Dust storm emission inversion using data assimilation

Jin, Jianbing

DOI
10.4233/uuid:c90cefff-2a6e-42f0-9893-a1c2cc11f1ac

Publication date
2019

Document Version
Final published version

Citation (APA)
Jin, J. (2019). *Dust storm emission inversion using data assimilation*. [Dissertation (TU Delft), Delft University of Technology]. https://doi.org/10.4233/uuid:c90cefff-2a6e-42f0-9893-a1c2cc11f1ac

DUST STORM EMISSION INVERSION USING DATA ASSIMILATION

DUST STORM EMISSION INVERSION USING DATA ASSIMILATION

Proefschrift

ter verkrijging van de graad van doctor
aan de Technische Universiteit Delft,
op gezag van de Rector Magnificus Prof. dr. ir. T.H.J.J. van der Hagen,
voorzitter van het College voor Promoties,
in het openbaar te verdedigen op dinsdag 3 december 2019 om 12.30 uur

door

Jianbing JIN

Master of Engineering in Electrical Engineering,
Harbin Institute of Technology, Harbin, China,
geboren te ShaoXing, China.

Dit proefschrift is goedgekeurd door de promotoren.

Samenstelling promotiecommissie:

Rector Magnificus,	voorzitter
Prof. dr. ir. H.X. Lin,	Technische Universiteit Delft, Promoter
Prof. dr. ir. A.W. Heemink,	Technische Universiteit Delft, Promoter
Onafhankelijke leden:	
Prof. dr. Z. Wang	Institute of Atmospheric Physics, China
Prof. dr. O.L. Quintero Montoya	U. EAFIT, Colombia
Prof. dr. ir. M. Verlaan	Technische Universiteit Delft
Prof. dr. ir. H.W.J. Russchenberg	Technische Universiteit Delft
Overig lid:	
Dr. ir. A.J. Segers,	TNO, the Netherlands

Keywords: Dust storm forecast, emission inversion, chemical tranport model, measurement, data assimilation

Author email: jianbing_jin@yahoo.com

ISBN 978-94-6384-092-7

An electronic version of this dissertation is available at
http://repository.tudelft.nl/.

Life never gives anything for nothing,
and that a price is always exacted for what fate bestows

— Stefan Zweig

CONTENTS

Summary xi

Samenvatting xiii

1 Introduction 1
- 1.1 Dust storm . . . 2
- 1.2 Dust model . . . 4
- 1.3 Data assimilation . . . 5
  - 1.3.1 Sequential data assimilation . . . 5
  - 1.3.2 Variational data assimilation . . . 5
- 1.4 Aerosol observations . . . 6
  - 1.4.1 Field station monitoring network . . . 6
  - 1.4.2 Remote sensing data . . . 7
- 1.5 Dust storm data assimilation . . . 8
- 1.6 Outline of this thesis . . . 9
  - 1.6.1 Aim . . . 9
  - 1.6.2 Research questions . . . 9
  - 1.6.3 Research approaches . . . 10
  - 1.6.4 Organization of the thesis . . . 11

2 LOTOS-EUROS chemical transport model and dust storm emission 21
- 2.1 LOTOS-EUROS chemical transport model . . . 22
  - 2.1.1 Model configurations . . . 22
  - 2.1.2 Dust aerosol description . . . 23
  - 2.1.3 Dust emission parametrization . . . 23
  - 2.1.4 Dust emission in LOTOS-EUROS . . . 24
- 2.2 Emission errors analysis . . . 26
  - 2.2.1 Uncertainty in the friction velocity . . . 28
  - 2.2.2 Uncertainty in the friction velocity threshold . . . 28
  - 2.2.3 Comparison of uncertainties . . . 29
- 2.3 Conclusions . . . 29

3 Reduced-tangent-linearization 4DVar 35
- 3.1 Introduction . . . 36
- 3.2 Dust event in April 2015 . . . 37
- 3.3 Data assimilation scheme . . . 38
  - 3.3.1 Spatially varying multiplicative factor (SVMF) for friction velocity threshold (FVT) . . . 38
  - 3.3.2 SVMF filters . . . 39
  - 3.3.3 Reduced-tangent-linearization 4DVar . . . 40

3.4 Dust storm observations from China MEP network . . . 42
3.5 Twin experiment results and discussion . . . 43
3.5.1 Experiment setup . . . 43
3.5.2 SVMF truth and observation operator . . . 44
3.5.3 Parameter estimation . . . 45
3.5.4 Dust flux estimation . . . 47
3.5.5 Model state estimation . . . 47
3.5.6 Computational complexity analysis . . . 49
3.6 Experiments with real field observations . . . 52
3.6.1 Statistical observation bias correction . . . 53
3.6.2 Observation representing error . . . 53
3.6.3 Results . . . 53
3.7 Conclusions . . . 58

4 Machine learning based observation bias correction 63
4.1 Introduction . . . 64
4.2 Emission inversion system . . . 66
4.2.1 Biased observation representing error . . . 67
4.2.2 Assimilation Window . . . 68
4.3 Observation bias correction methods . . . 68
4.3.1 Chemical transport model (Lotos-Euros/*non-dust*) . . . 68
4.3.2 Machine learning for *non-dust* PM_{10} simulations . . . 69
4.3.3 Evaluation of *non-dust* PM_{10} bias corrections . . . 71
4.4 Data assimilation experiments . . . 74
4.4.1 Observation error configuration . . . 77
4.4.2 Dust emission estimation . . . 78
4.4.3 Dust simulation and forecast skill . . . 79
4.4.4 Evaluation of forecast skill . . . 80
4.5 Conclusions . . . 83

5 Dust emission inversion using Himawari-8 AODs 89
5.1 Introduction . . . 90
5.2 Dust storm event in May 2017 . . . 91
5.3 Emission inversion system . . . 91
5.3.1 Data assimilation methodology . . . 91
5.3.2 Assimilation window . . . 94
5.4 Data for assimilation and validation . . . 94
5.4.1 Himawari-8 Aerosol Optical Depth (AOD) . . . 94
5.4.2 Himawari-8 AOD Versus AERONET . . . 96
5.4.3 Map of the field station observations . . . 97
5.5 Observation selection for data assimilation . . . 99
5.5.1 Inconsistence between the dust model and Himawari-8 AOD . . . 100
5.5.2 Background check . . . 101
5.5.3 Dust mask selection . . . 101

5.6 Assimilation result and discussion . . . 102
5.6.1 Emission analysis . . . 102
5.6.2 AOD analysis . . . 104
5.6.3 Comparison with surface PM_{10} . . . 105
5.6.4 Forecast skill . . . 111
5.7 Conclusions . . . 111

6 Backtracing dust emission errors using the adjoint method 115
6.1 Introduction . . . 116
6.2 Dust emission inversion . . . 118
6.3 Regional difference between observations and simulations . . . 120
6.4 Determine emission sources using an adjoint model . . . 121
6.4.1 Adjoint theory . . . 121
6.4.2 Test the implementation of the adjoint model . . . 125
6.4.3 Identification of emission sources . . . 127
6.5 Emission inversion with improved emission uncertainty . . . 129
6.6 Conclusions . . . 131
6.7 Supplementary . . . 132

7 Conclusions 137
7.1 Discussion of the research questions . . . 137
7.2 Outlook . . . 140

Acknowledgements 143

Curriculum Vitæ 145

List of Publications 147

SUMMARY

Severe dust storms present great threats to the environment, property and human health over the areas in the downwind of arid regions. Several dynamical dust models have been developed to predict the dust concentrations in the atmosphere. Currently, the accuracy of these models is limited mainly due to the imperfect modeling of dust emissions. Along with the progress in the dust and aerosol modeling, the advances in sensor technologies have made large-scale aerosol measurements feasible. The rich measurements provide opportunities to estimate uncertain emission fields, and subsequently, to improve the forecast skill. Such process of emission optimization conditioned on measurements is usually referred as *emission inversion*. Here, the term of *emission inversion* specially represents the way of deriving estimates from observations through the use of an atmospheric chemical transport model and a data assimilation method.

Emission inversion is usually challenging due to the huge computational costs of the assimilation algorithm, biases in the assimilated observations, observation-simulation inconsistence, and the difficulties in quantifying the intrinsic emission uncertainty. In this work, these challenges are explored for real severe dust storms that occurred in East Asia. The most important progress made in this study is the design of a dust emission inversion system which has a high computational efficiency, bias correction of PM_{10} measurements, data selection of satellite properties (AODs) as preprocessing before the assimilation, as well as an adjoint method for emission error detection.

As a first step we develop an integrated dust emission inversion system - a chemical transport model LOTOS-EUROS coupled with a reduced-tangent-linearization 4DVar data assimilation. Different from the traditional 4DVar which requires a huge effort to build and maintain the adjoint of a realistic model, our assimilation algorithm is adjoint-free. The computational complexity increases with the number of uncertain parameters. To further reduce the computation costs, a cascade of two model reduction techniques, sensitivity-based parameter filters and Proper Orthogonal Decomposition have been implemented, which lead to a reduction of the parameter dimension from initially $O(10^4)$ to $O(10^2)$.

Then, inversion of dust emission parameters is performed by assimilating PM_{10} measurements from an air quality monitoring network established by China Ministry of Environmental Protection. However, data assimilation relies on a basic assumption of an unbiased observation error, but the PM_{10} measurements are actually the sum of the dust aerosols and the particles released in local activities. For this application, the non-dust aerosols in PM_{10} are considered as nontrivial biases. The necessities of performing bias correction of PM_{10} measurements in dust emission inversion are illustrated. We adopted a novel data-based machine learning, as well as a traditional chemical transport model, to simulate the non-dust composition in PM_{10}, respectively. Experiments show that the posterior dust forecast driven by the estimated emissions was further improved by removing the bias from the assimilated measurements using any of the two bias correc-

tion methods. The best posterior emission fields are obtained when using the machine learning model for bias correction, with the existing measurements used more precisely and the resulting forecasts closer to reality.

In addition to the PM_{10} measurements from the air quality monitoring stations only located in the densely populated region and far away the dust sources, next, AODs from the new Himawari-8 satellite instrument are also assimilated. With the wide observing coverage and fine temporal resolution, this advanced geostationary instrument is capable of monitoring the East Asian dust storms which usually have great spatiotemporal variability. Promising results are obtained in AOD assimilation experiments for an extreme dust storm event. However, some AOD observations show significant inconsistence with the simulations and the PM_{10} and AERONET observations, which might be caused by retrieval errors over a partially clouded scene. The assimilation procedure therefore includes a screening method to exclude those observations in order to avoid unrealistic results. A dust mask screening method is designed, which selects only those observations where the deterministic model produces a substantial amount of dust. Experiments show that this screening algorithm provides more accurate results compared to the traditional method based on background covariance.

Finally, we design a method for backtracing the potential emission source using an adjoint method. One base of emission inversion using data assimilation is the correct assumptions about the emission background error covariance. However, a partially unrepresentative background uncertainty is unavoidable. Since in complex dust emission parameterization the uncertainties are induced by a lot of different inputs, they can hardly be taken into account all together. Regarding the investigated severe dust event, our assimilation system successfully resolved observation-minus-simulation errors in the most dust-affected regions. However, a large underestimation of dust in northeast China remained despite the assimilated measurements indicated severe dust plumes there. An adjoint model of our dust simulation system is therefore used to detect the most likely source region for these unresolved dust loads. The backward modeling points at the Horqin desert, which used to be considered as less important in East Asia dust storm forecast, but in this case is the most likely and nontrivial emission source. The reference emission and uncertainty are then reconstructed over the Horqin desert by assuming higher surface erodibility. After the emission reconstruction, the emission inversion is performed again and the posterior dust simulations are now in better agreement with the reality.

SAMENVATTING

Ernstige stofstormen vormen een grote bedreiging voor het milieu, eigendommen en de gezondheid over de regio's in de wind van droge gebieden. Verschillende dynamische stofmodellen zijn ontwikkeld om de stofconcentraties in de atmosfeer te voorspellen. Momenteel is de nauwkeurigheid van deze modellen voornamelijk beperkt door de imperfecte modellering van stofemissies. Samen met de vooruitgang in de stof- en aerosolmodellering, de vooruitgang in sensor technologieën hebben grootschalige aërosolmetingen mogelijk gemaakt. De beschikbaarheid van enorme hoeveelheid meetdata bieden mogelijkheden om onzekere emissievelden te schatten en vervolgens de voorspellingsvaardigheid verbeteren. Een dergelijk proces van emissieoptimalisatie door middel van meetdata wordt meestal emissie-inversie genoemd. Hier de term emissie-inversie doelt met name op de manier om schattingen af te leiden uit waarnemingen door het gebruik van een atmosferisch chemisch transportmodel en een data-assimilatiemethode.

Emissie-inversie is meestal een uitdaging vanwege de enorme rekenkosten van de assimilatie-algoritme, vertekeningen in de geassimileerde waarnemingen, observatiesimulatie inconsistentie en de moeilijkheden bij het kwantificeren van de intrinsieke emissieonzekerheid. In dit werk worden deze uitdagingen onderzocht voor echte zware stofstormen die zich in het Oost-Azië hebben voorgedaan. De belangrijkste vooruitgang die in dit onderzoek is geboekt, is het ontwerpen van een stofemissie-inversie systeem met een hoge rekenefficiëntie, bias-correctie van PM_{10}-metingen, dataselectie van satellietwaarnemingen (AOD's) als voorbewerking vóór de assimilatie, evenals een adjoint methode voor detectie van fouten in emissiedata.

Als eerste stap ontwikkelen we een geïntegreerd stofemissie-inversiesysteem - een chemische stof transportmodel LOTOS-EUROS gekoppeld aan een 4DVar met gereduceerde tangens-linearisatie data-assimilatie. Anders dan de traditionele 4DVar die een enorme inspanning vereist om het adjoint van een realistisch model te implementeren, ons assimilatie-algoritme is adjoint-vrij. De rekencomplexiteit neemt toe met het aantal onzekere parameters. Om de rekenkosten verder te verlagen, een cascade van twee modelreductietechnieken, gevoeligheid-gebaseerde parameter filters en Proper Orthogonal Decomposition hebben geïmplementeerd, wat in eerste instantie leidde tot een vermindering van de parameterdimensie van $O(10^4)$ tot O (10^2).

Vervolgens wordt de inversie van stofemissie uitgevoerd door PM_{10}-metingen te assimileren van een monitoringnetwerk voor luchtkwaliteit dat is opgericht door het Chinese ministerie van Milieu Bescherming. Data assimilatie is echter gebaseerd op een basisaanname van een objectieve observatiefout, maar de gemeten PM_{10} concentraties zijn eigenlijk de som van het stof afkomstig uit de woestijn en de deeltjes die vrijkomen bij lokale activiteiten. Voor deze toepassing wordt het niet-woestijnstof in PM_{10} als niet-triviale bias beschouwd. We hebben de noodzaak van een bias-correctie van PM_{10}-metingen bij stofemissie-inversie aangetoond, vervolgens gebruiken we een nieuw op data gebaseerd machine learning algoritme, evenals een traditioneel chemisch trans-

portmodel, om de niet-woestijnstof in PM_{10} als bias-term te berekenen. Experimenten tonen aan dat de posterior stofvoorspelling met de gecorrigeerde emissies werd verder verbeterd na aftrek van de bias in de metingen met behulp van een van de twee bias-correctie methoden. De beste posterior emissievelden worden verkregen bij gebruik van de machine learning voor biascorrectie, waarbij de resulterende voorspellingen dichter bij de realiteit komen.

De meetstations van de PM_{10} meetnetwerk voor luchtkwaliteit liggen in het dichtbevolkte gebied en ver weg de stofbronnen, daarom onderzoeken we de mogelijkheid om AOD's van het nieuwe Himawari-8 satellietinstrument te gebruiken. Met zijn brede dekking en fijne temporale resolutie, dit geavanceerde geostationaire instrument is in staat om de Oost-Aziatische stofstormen te observeren die meestal grote spatiotemporele variabiliteit hebben. Veelbelovende resultaten worden verkregen in AOD assimilatie experimenten voor een extreme stofstormgebeurtenis. Sommige AOD-waarnemingen vertonen echter significante inconsistentie met de simulaties en de PM_{10}- en AERONET-waarnemingen, die mogelijk worden veroorzaakt door ophaalfouten in een gedeeltelijk bewolkte scène. De assimilatieprocedure bevat daarom een screeningmethode om observaties uit te sluiten die tot onrealistische resultaten kunnen leiden. Een stofmasker screening methode is hiervoor ontworpen, die alleen de waarnemingen selecteert waarbij het deterministische model een aanzienlijke hoeveelheid stof produceert. Experimenten laten zien dat dit screening-algoritme nauwkeurigere resultaten oplevert in vergelijking met de traditionele methode op basis van achtergrondcovariantie.

Ten slotte ontwerpen we een methode om de potentiële emissiebron te traceren met behulp van een adjoint methode. Eén basis van emissie-inversie met behulp van data assimilatie is de juiste veronderstellingen over de emissie achtergrondfout covariantie. Echter een gedeeltelijk niet representatief achtergrondonzekerheid is onvermijdelijk. In complexe stofemissie-parametrering de onzekerheden worden veroorzaakt door veel verschillende inputs. Wat betreft de onderzochte ernstige stofgebeurtenis, onze assimilatiesysteem heeft met succes observatie-minus-simulatiefouten in de meest door stof aangetaste gebieden opgelost. Een grote onderschatting van stof in Noordoost-China bleef ondanks de geassimileerde metingen daar ernstige stofpluimen aangeven. Een adjoint model van ons stofsimulatiesysteem wordt daarom gebruikt om de meest waarschijnlijk brongebied voor deze onopgeloste stofbelastingen te detecteren. De achterwaartse modellering wijst naar de Horqin-woestijn, die vroeger als minder belangrijk werd beschouwd in de stofstorm in Oost-Azië voorspelling, maar is in dit geval de meest waarschijnlijke en niet-triviale emissiebron. De referentie emissie en onzekerheid worden vervolgens gereconstrueerd over de Horqin-woestijn door hogere erodeerbaarheid van het oppervlak aan te nemen. Na de emissie-reconstructie is de emissie-inversie opnieuw uitgevoerd en de posterior stofsimulaties zijn nu beter in overeenstemming met de realiteit.

1

INTRODUCTION

Dust storms are of high interest since they pose great threats to the human health, cause severe disruption of transportation and aviation systems, and have profound effects on the Earth energy cycles.

Dynamic model systems have been established in the last three decades to serve as a key element of dust forecasting and early warning systems. However, the accuracy of those existing dust storm models are limited mainly due to the difficulty in accurately modeling the dust emission.

Data assimilation has been identified as a research priority to improve the dust storm forecast skills by feeding available measurements into dust models.

1

1.1. DUST STORM

DUST storms, e.g., the one captured in Fig. 1.1, are a type of lower atmosphere events, and defined as meteorological hazards by the World Meteorological Organization (WMO). They occurred as a result of wind erosion liberating particles from exposed dry surfaces (UNEP. et al., 2016, WMO, 2019).

Figure 1.1: A massive sand storm swept through a village next to Gobi desert. Source: Mail online

Dust storms occur relatively common in arid or semi-arid regions. However, finer dust particles may be lifted several kilometers high into the atmosphere, subsequently carried over long distances by the prevailing winds, even across continents (Shao et al., 2011, Zhang et al., 2018). Together with substantial amounts of dust particles, dust storms may also carry irritating spores, bacteria, viruses and persistent organic pollutants (WMO, 2017). They pose great threats to human health e.g., dust pneumonia, strep throat, cardiovascular disorders and eye sicknesses, e.g., illness reported in Fig. 1.2, especially in downwind regions (Benedetti et al., 2014, Ozer et al., 2007, Shao and Dong, 2006, WMO, 2018).

Next to the human health, the resulting low visibility can cause severe disruptions of the transportation and aviation systems. For instance, struck by a choking dust storm, the visibility has plummeted in Beijing and over 1,100 flights were delayed in early May 2017 (Jin et al., 2019). Industries like semiconductor ones will also be threatened since they require a clean atmosphere to fabricate electronic chips (Benedetti et al., 2014).

The dust cycle itself is also a key player in the Earth system with profound effects on cycles of energy, carbon and water. Each year, an estimation of 2000 Mt dust is emitted into the atmosphere, 75% of which is deposited to land while the rest is deposited to the ocean (Shao et al., 2011). These particles fertilize both the terrestrial and ocean ecosystem, boosting primary productivity. Dust particles also interact with atmospheric radiation and may significantly modify the Earth radiative balance (Balkanski et al., 2007, Calil

Figure 1.2: Sand storm triggers allergies, breathlessness in Dubai in April 2015. Source: Gulf News Health

et al., 2011, Shao and Dong, 2006, Wu et al., 2016). The importance of dust for weather forecast, e.g., through enhancing precipitation by acting as droplet neclei, has also been recognized (Benedetti et al., 2014, UNEP. et al., 2016).

On the planetry scale, the global dust pattern shown in Fig. 1.3 closely matches the distribution of earth arid surface shown in Fig. 1.4, since both of them are governed by the general atmospheric circulation (Kaskaoutis et al., 2018, Prospero et al., 2002, Shao et al., 2013). Those research revealed that North Africa, the Middle East, Southwest Asia, South America, and East Asia have experienced the majority of regular dust events in the past decades.

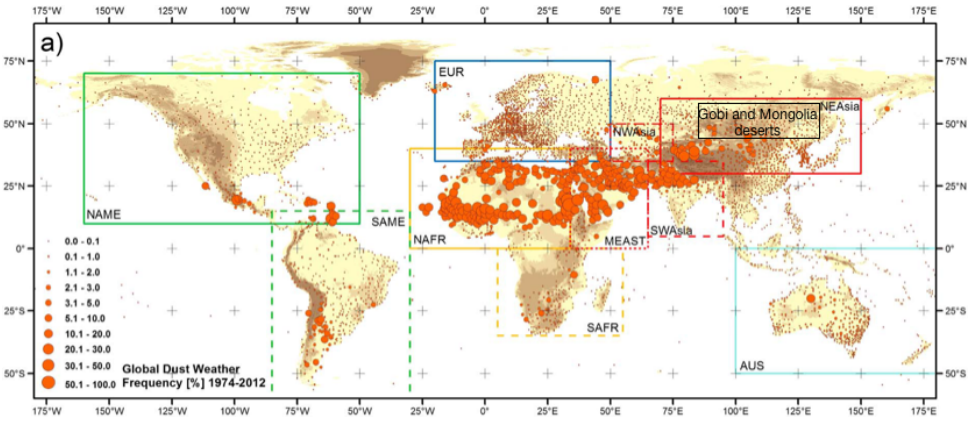

Figure 1.3: Global pattern of dust weather frequency estimated from the weather records for the period of 1974 to 2012. This figure is adapted from Fig.2 in Shao et al. (2013)

In this thesis, the main focus is on the severe dust storms that occurred in East Asia, but the methodology developed can also be applied to other areas. For centuries, East Asia is frequently affected by severe dust storms every year, especially in late spring

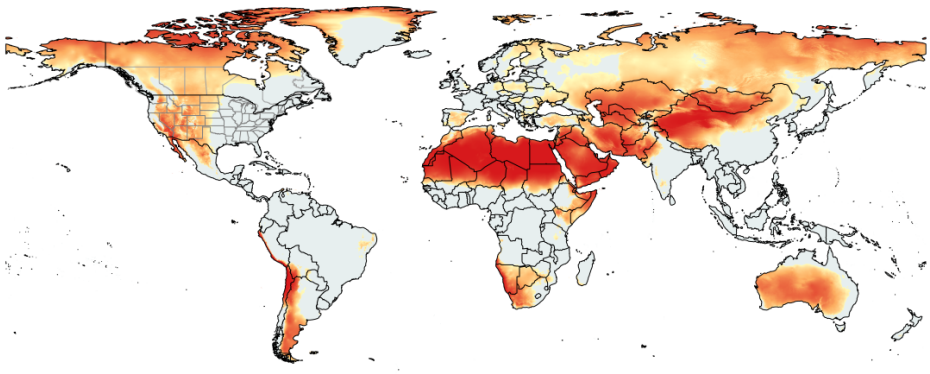

Figure 1.4: Global arid zone distribution, in which the arid region is colored with red. Source: *World Clim, v2.0*

and early summer. The last decades have even seen an increase of dusts, likely due to the population expansion and land desertification (Gong et al., 2004). These dust storms usually originated from the Mongolia and Gobi Deserts in the north (see Fig. 1.3), and then moved to the densely populated southeastern areas of China by the prevailing winds. Occasionally, dust clouds reached the Korean peninsula and Japan, and parts of dust plumes were even transported across the Pacific Ocean eventually. Though these dust events usually lasted for a few days, they carried a great amount of dust aerosols to the downwind regions, causing the aforementioned damages to several hundred millions of people. Two of the most severe dust events in the last decade (occurred in April 2015 and May 2017) are used as the test cases in this thesis.

1.2. DUST MODEL

The interest to understand the formation and spread of dust from health professionals, aviation authorities and policy makers have grown since the last two decades. A huge amount of effort has been paid to mathematically describe the dust life cycles of emission, transport and deposition (Alfaro et al., 1997, Gong et al., 2003, Liu et al., 2003, Marticorena and Bergametti, 1995, Marticorena et al., 1997, Shao et al., 1996, Wang et al., 2000). Since the early 1990s, chemical transport models (CTM) involving dust simulations (Uno et al., 2006, Zhao et al., 2006) have been developed in research groups and weather prediction centers in order to reduce threats that dust storms pose. At the present, global/regional dust storms, e.g., ECMWF Integrated Forecast System (IFS) (Morcrette et al., 2008a,b, 2009), BSCDREAM8b (Mona et al., 2014, Pérez et al., 2006), CUACE/Dust(Gong and Zhang, 2008, Zhou et al., 2008), GEOS-Chem (Fairlie et al., 2007) and LOTOS-EUROS (Manders et al., 2017, Timmermans et al., 2017) are widely used for the operational aerosol forecasting.

Those models not only help us to better understand the characteristics of the dust storms, but are also essential elements of dust forecasting and early warning systems. However, usually huge discrepancies exist in simulated dust concentrations and observations. It is reported that the differences between dust simulations and real measure-

ments can be as large as two orders of magnitudes (Huneeus et al., 2011, Niu et al., 2008). The most important reason for such wide scattering of model errors is the difficulty in accurately modeling the dust emission, of which the details are demonstrated in Chapter 2.2.

1.3. DATA ASSIMILATION

Mathematically, models are often uncertain due to insufficient knowledge on the full aspects of a system or due to limited computation power to conduct simulations in fine scale. Even if the model is very accurate, the outcome will still not be able to reproduce the reality unless we have the knowledge of the initial/boundary conditions, forcing inputs and other model parameters (Evensen, 2009, Chapter 1).

A realization from one model integration, therefore, is only one likely estimate of the reality, and the full spread or probability density function (pdf) of model states is unknown. The pdf of model states is actually a fundamental part of a model. It can not only be used in model outcome evaluation, but also as a base to derive the most likely estimate of the model states.

In addition to the model, observations of the model variables are also collected. Those measurements can be feed into the dynamic models to improve the estimate of model states or other uncertain parameters through data assimilation.

The essence of data assimilation has been defined in various ways. Evensen (2009) referred to data assimilation as "*the computation of the pdf of model solution conditioned on the given observations*". In Kalnay (2002), data assimilation is defined as "*a statistical combination of observations and short-range forecasts*". Talagrand (1997) stated that data assimilation can be described as "*the process through which all the available information is used in order to estimate as accurately as possible the investigated model*".

From an algorithmic point of view, the existing data assimilation methods can be described as either *sequential* or *variational* (Talagrand, 1997).

1.3.1. SEQUENTIAL DATA ASSIMILATION

In *sequential assimilation*, when a model forwards to a time instant where observations are available, the background model variables are taken as *a priori* estimate which will be updated/corrected by using the measurements. The outcome from the estimation is referred as *a posterior*. The model will then propagate forward in time with the *posterior* from the updated model states. This procedure will be repeated until all observations are assimilated. The typical *sequential* data assimilation that are widely implemented in geoscience modeling (Fu et al., 2015, Houtekamer and Mitchell, 2001, Houtekamer and Zhang, 2016) is the Ensemble Kalman Filter (EnKF), which was introduced by Evensen (1994, 2003).

1.3.2. VARIATIONAL DATA ASSIMILATION

Variational data assimilation (DA) aims to obtain the posterior that optimally fits all the observations over an assimilation window with several observational instants. It is a powerful method to reconstruct or update the structure of initial/boundary condition, input emission and other imperfect model parameters.

The typical variational method is the four dimensional variation (4DVar) data assimilation. This optimal is calculated by minimizing a cost function:

$$\mathcal{J}(\boldsymbol{x}_0) = \frac{1}{2}(\boldsymbol{x}_0 - \boldsymbol{x}_0^b)^T \mathbf{B}^{-1} (\boldsymbol{x}_0 - \boldsymbol{x}_0^b) + \frac{1}{2}\sum_{i=1}^{k}(\boldsymbol{y}_i - \mathcal{H}_i(\boldsymbol{x}_i))^T \mathbf{R}_i^{-1} (\boldsymbol{y}_i - \mathcal{H}_i(\boldsymbol{x}_i)) \quad (1.1)$$

where the subscript i represents instants involved in the assimilation window. $\boldsymbol{x}_0$ is the initial condition to be estimated, which could be the emission field or boundary condition depending on the application. $\boldsymbol{y}_i$ is the vector of available observations for the time instant i; $\boldsymbol{x}_i$ denotes the vector of model variables, which is transfered to observation space through operator $\mathcal{H}_i$. Background error covariance $\mathbf{B}$ and observation error covariance $\mathbf{R}_i$ quantify the uncertainties of the background and observations, respectively.

In the circumstance that the estimates are the emission fields or scaling factors for the emission inventory, such optimization is referred as *emission inversion* or *emission inverse modeling* in this thesis. Note that emission inversion is also doable through using other statistical methods. Here it specifically represents the process of deriving estimates from observations through the use of an atmospheric chemical transport model and a data assimilation method.

Once the assimilation analysis is completed, the model will be restarted over the assimilation window using the *posterior* to generate the reanalysis over the assimilation cycle as well as the forecast.

Other popular variational data assimilation methods are three dimensional variational (3DVar), four dimensional ensemble variational (4DEnVar) (Liu et al., 2008, 2009), Hybrid 4DVar (Lorenc et al., 2015), trajectory-based 4DVar (Lu et al., 2015). In this thesis, a *reduced-tangent-linearization* 4DVar is designed and used in the dust storm emission inversion. The algorithm is introduced in Chapter 3.

1.4. AEROSOL OBSERVATIONS

Along with the progress in the dust/aerosol modeling, the advances in sensor technologies and the continuously decreasing costs of electronic devices have made large-scale aerosol measurements feasible. Both aerosol monitoring devices onboard satellites or based on ground stations have been used in the last two decades. The rich data from the measurements provide opportunities to identify the dust emission source regions, the aerosol size distribution, the process of long-distance transport, as well as to evaluate the model performance at various timescales. In addition, these measurements are of high importance since they can be assimilated to correct the dust model errors through data assimilation.

Since this thesis focuses on dust storms over East Asia, only measurements covering this research domain are explored.

1.4.1. FIELD STATION MONITORING NETWORK

Since 2013, the China Ministry of Environmental Protection (MEP) has commenced to release the hourly-average measurements of atmospheric constituents including $PM_{2.5}$, PM_{10}, CO, O_3 and SO_2 (Li et al. (2017)). A huge number of ground stations measuring these air quality indices have been established in densely populated areas. At the

present, the monitoring network has grown to 1,500 field stations covering all over China as shown in Fig. 1.5.

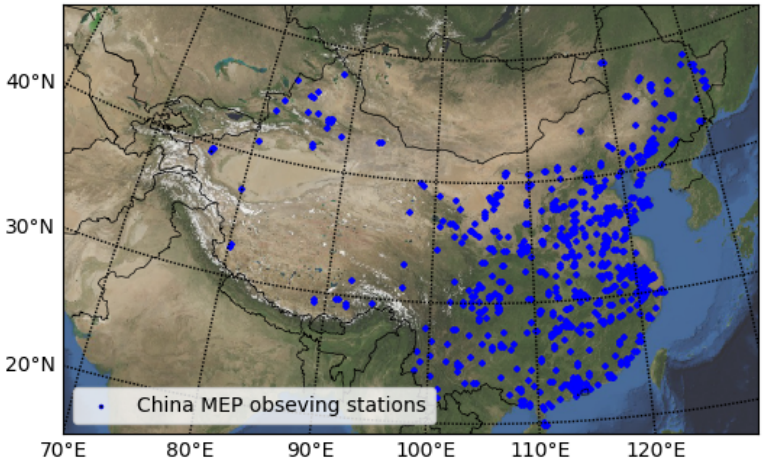

Figure 1.5: The China MEP air quality monitoring network.

Due to the high temporal resolutions and the rather dense monitoring network, the ground-based air quality observing network has become a powerful source to capture the rapid spatiotemporal variability of dust storms. The records, mainly the PM_{10} feature, were widely used to calibrate and assess the dust model (Benedetti et al., 2018, Huneeus et al., 2011, Lin et al., 2008a, Wang et al., 2008, Yumimoto et al., 2016a).

However, the observed full aerosol observations do not only consist of dust, but are actually the sum of the dust and other aerosols. The latter is emitted not only from anthropogenic activities such as industries, vehicles, and households, but also from natural sources such as wild fires and sea spray. Especially for the PM_{10} concentration at ground level, the reported values during dust storms are more like to be mixed with the contribution from *non-dust* aerosols. In this thesis we will simply regard the *non-dust* fraction of the total PM_{10} as an observation bias. The PM_{10} are either assimilated directly or preprocessed with different bias corrections before assimilation (Chapter 3 and Chapter 4).

1.4.2. REMOTE SENSING DATA

Another important monitoring technology for tracking dust storms is remote sensing from space. The remote sensing instruments with the wide observing coverage is the best option to completely identify the large-scale dust storms compared to the existing ground based monitoring systems (Knippertz and Stuut, 2014). For instance, the ground-based stations that observe aerosols (including dust) are often located only in populated regions for easier construction and maintenance, which are normally far away from the source regions. Those instruments can only measure the dust levels when the

plumes have already arrived in the downwind areas, hence they are of limited help to the early dust forecasting and warning system, especially for the cities near the dust sources.

In fact, aerosol optical depths (AODs) from satellites have been widely used in the dust forecast and early warning system. Up to now, aerosol products from the Moderate Resolution Imaging Spectroradiometer (MODIS) instrument onboard the polar orbiting satellites Terra and Aqua have also been widely used in global or East Asia aerosol/dust monitoring (Di Tomaso et al., 2017, Escribano et al., 2016, Khade et al., 2013, Schutgens et al., 2012, Yumimoto et al., 2016a, Yumimoto and Takemura, 2015). While those AOD observations only provide information about the total column, satellite observations from the CALIPSO instrument provides views on the vertical structure of a dust plume Winker et al. (2007).

Designed with the wide observing coverage and high temporal resolution, geostationary measuring instruments provide valuable information to track these short term and fast-changing airborne pollution events. An example is the SEVERI instrument onboard the MSG (Meteosat Second Generation) mission, from which the aerosol products have been used in dust storm detection over North Africa (Ian and Richard, 2012) and estimation of volcanic ash emissions affecting Europe (Fu et al., 2017). The first of the new-generation geostationary Earth orbit meteorological satellites, Himawari-8 was launched in October 2014 by the Japan Meteorological Agency (JMA) (Bessho et al., 2016), and is pointed to East Asia. One of the instruments on the satellite is the Advanced Himawari Imager (AHI), which has significantly higher radiometric, spectral, and spatial resolution than those previously available in the geostationary orbit. The AHI has a multi-band imager with 16 spectral channels, covering a wavelength range from 0.46 to 13.3 μm. With a short observation interval of 10 minutes for the full disk and 2.5 min for specific target regions, Himawari-8 has the ability to track fast-changing phenomena, and thus provide useful data for assimilation into a dust storm model over East Asia. The Himawari-8 aerosol measurements have already been used in the airborne aerosol assimilation (Yumimoto et al., 2016b), and also in the dust data assimilation which shows the overwhelming strength compared to the MODIS satellite measurements (Sekiyama et al., 2016).

In Chapter 5, we will explore the dust emission inversion using AOD observations from the Himawari-8 instrument. The geostationary satellite potentially covers both the dust source regions as well as the dust affected regions, with high spatial and temporal resolution. This opens the possibility that a dust storm is observed in an early stage already, and could therefore help to reduce the uncertainty in the emission estimate.

1.5. DUST STORM DATA ASSIMILATION

As aforementioned, data assimilation has been widely used to feed available measurements into the dynamic models for correcting imperfections in atmospheric applications (Dubovik et al., 2008, Hakami et al., 2005, Schutgens et al., 2012, Sekiyama et al., 2010). In the dust modeling field, both the sequential and variational data assimilation methods have been adopted either to estimate the 3D dust concentration fields or uncertain model parameters, for instance, the dust emissions and intial 3D dust levels.

Surface visibility and Aerosol Optical Depth (AOD) were incorporated into the China Unified Atmospheric Chemistry Environment/Dust (CUACE/Dust) model to correct the

errors in initial conditions using 3DVar (Gong and Zhang, 2008, Niu et al., 2008, Wang et al., 2008, Zhou et al., 2008). In that work, a relationship between PM_{10} observations and visibility was established, which transferred the large number of visibility monitoring data into dust concentrations. Lin et al. (2008a,b) assimilated daily averaged PM_{10} using an Ensemble Kalman Filter (EnKF), which also resulted in corrected initial model states.

In addition to the state estimation, emission inversion from observations through variational data assimilation is also an important research topic in dust modeling. Yumimoto et al. (2008) assimilated AOD observations from ground-based LIDAR sites to estimate the dust emission rate using four dimensional variational (4DVar) data assimilation. Aerosol products from the MODIS instrument have also been used widely in dust/aerosol emission inverse modeling by ensemble-based (Di Tomaso et al., 2017, Khade et al., 2013, Schutgens et al., 2012, Yumimoto et al., 2016a) and variational data assimilation (Escribano et al., 2016, Yumimoto and Takemura, 2015). Observations from the CALIPSO instrument that provide information on the vertical structure of a dust plume are also used to estimate the emission field using 4D-LETKF (Sekiyama et al., 2010).

Though remarkable progress has been made in these studies, the dust storm data assimilation still has large spaces for improvements. To further optimize the fast-varying dust storms, challenges include development of more efficient assimilation algorithms, use of new types of observations with a wide spatiotemporal coverage and a fine resolution, observation quality control strategies, accurate quantification of the error sources in dust simulations.

1.6. OUTLINE OF THIS THESIS

1.6.1. AIM

From the previous section, it follows that forecast skills of existing dust storm models are limited mainly due to the imperfections in the emission parametrization, and that data assimilation has been identified as a research priority to correct errors in dynamic models conditioned on the available measurements. Therefore, the main aim of this thesis is to develop a dust storm emission inversion system using data assimilation techniques. The system allows assimilation of observations from various aspects (PM_{10} concentrations and remote sensing data) to update the dust emission fields which could drive a dust forecast with a higher accuracy. In this thesis, the dust emission inversion is explored based on cases of two extremely severe dust storm events that occurred in East Asia, in April 2015 and May 2017, respectively.

1.6.2. RESEARCH QUESTIONS

The specific research questions addressed in this thesis are:

1. How to quantify the uncertainty in state-of-the-art dust emission parametrization? In data assimilation context that means: how to configure the background error covariance?

2. How to develop a data assimilation algorithm for the dust emission inversion with

a high computational efficiency?

3. When assimilating PM_{10} observations with dust simulations, to what extent is the non-dust bias in these observations misleading the analysis, and how to use the full aerosol measurements as a proxy for dust in the emission inversion?

4. What is the added value of assimilating aerosol properties from a geostationary satellite, and how to exclude inconsistent AOD observations which might arise from retrieval errors over a partially clouded scene?

1.6.3. RESEARCH APPROACHES

Emission inversion using data assimilation relies on the correct assumption about the background error covariance. To answer research question 1 we first analyze the error sources in the dust emission parametrization scheme, and identify that the error in the friction velocity threshold (FVT) parametrization has the dominant contribution to the emission variability, compared to other inputs like the friction velocity. A spatially varying multiplicative factor (SVMF) is introduced for the friction velocity threshold (FVT) to correct the mismatch in the dust emission scheme in Chapter 2. The SMVFs are estimated in the emission inversion system, and the dust storm forecast driven by the estimated emission field (using the estimated SVMFs) is evaluated through a comparison with independent data in Chapter 3.

Regarding research question 2, one of the most challenging parts in the dust emission inversion system is the development of a tangent linear model of the chemical transport model. Chapter 3 focuses on the design of an adjoint-free 4DVar, in which the tangent linear model is calculated using a perturbing method. Since the computational complexity of this DA algorithm increases with the number of uncertain parameters, model reducing techniques, e.g., sensitivity-based parameter filters and Proper Orthogonal Decomposition, are designed to achieve a high computational efficiency.

Data assimilation algorithms rely on a basic assumption of an unbiased observation error. In the presence of biases, the assimilation analysis might diverge from reality, since the data assimilation itself cannot distinguish whether the differences between model simulations and observations are due to the biased observations or model deficiencies. However, the presence of inconsistent measurements with nontrivial biases is unavoidable in practice. In this dust emission inversion, all measurements available are actually full aerosol observations, which is a sum of *dust* and *non-dust* aerosols, instead of the 'pure' dust measurements. In Chapter 4, research question 3 is studied by exploring a machine learning based observation bias correction method, which enables the use of those full aerosol measurements (mainly PM_{10}) as a proxy for the dust concentrations under severe dust conditions.

In Chapter 5, the availability of Himawari-8 AOD observations allows to explore the strengths of assimilating the geostationary satellite data, which are designed with a wide scanning coverage and a high temporal resolution. In addition, regarding the inconsistent AOD measurements mentioned in research question 4, we also design a screening method in the assimilation procedure to exclude these observations in order to avoid unrealistic results.

In Chapter 6 challenges mentioned in research question 1 are further studied. Previous research on the dust emission inversion all used an empirical background error covariance. Therefore a partially unrepresentative background uncertainty is unavoidable since the intrinsic uncertainties are actually induced from a lot of different inputs, which might not able to fully resolve observation-minus-simulation differences. Chapter 6 describes the use of an adjoint method to backtrack the most likely source region for these unresolved dust loads. The resulted emission sensitivity can guide the construction of a more accurate background covariance which can better explain the remaining residues.

1.6.4. ORGANIZATION OF THE THESIS

The thesis is organized as follows: Chapter 2 describes the LOTOS-EUROS/dust model that is used to simulate the dust storms over East Asia. An analysis of the crucial uncertainties in the emission parametrization is included which will be used to describe the background error covariance in our emission inversion system. In Chapter 3, an integrated dust storm emission inversion system, LOTOS-EUROS/dust coupled with an adjoint-free *reduced-tangent-linearization* 4DVar is developed. Chapter 4 reports how data-driven machine learning can be used to perform observation bias correction in order to use the PM_{10} measurements as proxy of dust concentration. Chapter 5 examines the key strengths of assimilating the data from the geostationary satellite Himawari-8 which has a relatively wide observing coverage and a high temporal resolution. In Chapter 6, we present how to trace back dust emission errors using the adjoint method, and show that a representative background uncertainty could help to resolve the observation-simulation discrepancies in emission inversion more accurately. Finally, Chapter 7 summarizes the conclusions of this thesis and the recommendations for further study.

REFERENCES

Alfaro, S. C., Gaudichet, A., Gomes, L., and Maillé, M. (1997). Modeling the size distribution of a soil aerosol produced by sandblasting. *J. Geophys. Res.*, 102(D10):11239–11249.

Balkanski, Y., Schulz, M., Claquin, T., and Guibert, S. (2007). Reevaluation of mineral aerosol radiative forcings suggests a better agreement with satellite and AERONET data. *Atmospheric Chemistry and Physics*, 7(1):81–95.

Benedetti, A., Baldasano, J. M., Basart, S., Benincasa, F., Boucher, O., Brooks, M. E., Chen, J.-P., Colarco, P. R., Gong, S., Huneeus, N., et al. (2014). *Operational dust prediction*. Springer.

Benedetti, A., Di Giuseppe, F., Jones, L., Peuch, V. H., Remy, S., and Zhang, X. (2018). The impact of data assimilation on the prediction of Asian desert dust using an operational 4D-Var system. *Atmospheric Chemistry and Physics Discussions*, pages 1–17.

Bessho, K., Date, K., Hayashi, M., Ikeda, A., Imai, T., Inoue, H., Kumagai, Y., Miyakawa, T., Murata, H., Ohno, T., Okuyama, A., Oyama, R., Sasaki, Y., Shimazu, Y., Shimoji, K., Sumida, Y., Suzuki, M., Taniguchi, H., Tsuchiyama, H., Uesawa, D., Yokota, H., and Yoshida, R. (2016). An Introduction to Himawari-8/9— Japan’s New-Generation Geostationary Meteorological Satellites. *Journal of the Meteorological Society of Japan. Ser. II*, 94(2):151–183.

Calil, P. H. R., Doney, S. C., Yumimoto, K., Eguchi, K., and Takemura, T. (2011). Episodic upwelling and dust deposition as bloom triggers in low-nutrient, low-chlorophyll regions. *J. Geophys. Res.*, 116(C6):C06030+.

Di Tomaso, E., Nick, Jorba, O., and Garcia-Pando, C. P. (2017). Assimilation of MODIS Dark Target and Deep Blue observations in the dust aerosol component of NMMB-MONARCH version 1.0. *Geoscientific Model Development*, 10:1107–1129.

Dubovik, O., Lapyonok, T., Kaufman, Y. J., Chin, M., Ginoux, P., Kahn, R. A., and Sinyuk, A. (2008). Retrieving global aerosol sources from satellites using inverse modeling. *Atmospheric Chemistry and Physics*, 8(2):209–250.

Escribano, J., Boucher, O., Chevallier, F., and Huneeus, N. (2016). Subregional inversion of North African dust sources. *Journal of Geophysical Research: Atmospheres*, 121(14):8549–8566.

Evensen, G. (1994). Sequential data assimilation with a nonlinear quasi-geostrophic model using Monte Carlo methods to forecast error statistics. *J. Geophys. Res.*, 99(C5):10143–10162.

Evensen, G. (2003). The Ensemble Kalman Filter: theoretical formulation and practical implementation. *Ocean Dynamics*, 53(4):343–367.

Evensen, G. (2009). *Data assimilation: the ensemble Kalman filter*. Springer Science & Business Media.

Fairlie, T. D., Jacob, D. J., and Park, R. J. (2007). The impact of transpacific transport of mineral dust in the united states. *Atmospheric Environment*, 41(6):1251 – 1266.

Fu, G., Lin, H., Heemink, A., Segers, A., Lu, S., and Palsson, T. (2015). Assimilating aircraft-based measurements to improve forecast accuracy of volcanic ash transport. *Atmospheric Environment*, 115:170 – 184.

Fu, G., Prata, F., Lin, H. X., Heemink, A., Segers, A., and Lu, S. (2017). Data assimilation for volcanic ash plumes using a satellite observational operator: a case study on the 2010 Eyjafjallajökull volcanic eruption. *Atmospheric Chemistry and Physics*, 17(2):1187–1205.

Gong, S. L. and Zhang, X. Y. (2008). CUACE/Dust – an integrated system of observation and modeling systems for operational dust forecasting in Asia. *Atmospheric Chemistry and Physics*, 8(9):2333–2340.

Gong, S. L., Zhang, X. Y., Zhao, T. L., and Barrie, L. A. (2004). Sensitivity of Asian dust storm to natural and anthropogenic factors. *Geophysical Research Letters*, 31(7).

Gong, S. L., Zhang, X. Y., Zhao, T. L., McKendry, I. G., Jaffe, D. A., and Lu, N. M. (2003). Characterization of soil dust aerosol in China and its transport and distribution during 2001 ACE-Asia: 2. Model simulation and validation. *J. Geophys. Res.*, 108(D9):4262+.

Hakami, A., Henze, D. K., Seinfeld, J. H., Chai, T., Tang, Y., Carmichael, G. R., and Sandu, A. (2005). Adjoint inverse modeling of black carbon during the Asian Pacific Regional Aerosol Characterization Experiment. *J. Geophys. Res.*, 110(D14):D14301+.

Houtekamer, P. L. and Mitchell, H. L. (2001). A Sequential Ensemble Kalman Filter for Atmospheric Data Assimilation. *Monthly Weather Review*, 129(1):123–137.

Houtekamer, P. L. and Zhang, F. (2016). Review of the ensemble kalman filter for atmospheric data assimilation. *Monthly Weather Review*, 144(12):4489–4532.

Huneeus, N., Schulz, M., Balkanski, Y., Griesfeller, J., Prospero, J., Kinne, S., Bauer, S., Boucher, O., Chin, M., Dentener, F., Diehl, T., Easter, R., Fillmore, D., Ghan, S., Ginoux, P., Grini, A., Horowitz, L., Koch, D., Krol, M. C., Landing, W., Liu, X., Mahowald, N., Miller, R., Morcrette, J. J., Myhre, G., Penner, J., Perlwitz, J., Stier, P., Takemura, T., and Zender, C. S. (2011). Global dust model intercomparison in AeroCom phase I. *Atmospheric Chemistry and Physics*, 11(15):7781–7816.

Ian, A. and Richard, W. (2012). An automated dust detection using SEVIRI: A multiyear climatology of summertime dustiness in the central and western Sahara. *Journal of Geophysical Research: Atmospheres*, 117(D8).

Jin, J., Lin, H. X., Segers, A., Xie, Y., and Heemink, A. (2019). Machine learning for observation bias correction with application to dust storm data assimilation. *Atmospheric Chemistry and Physics*, 19(15):10009–10026.

Kalnay, E. (2002). *Atmospheric Modeling, Data Assimilation and Predictability*. Cambridge University Press.

Kaskaoutis, D., Houssos, E., Solmon, F., Legrand, M., Rashki, A., Dumka, U., Francois, P., Gautam, R., and Singh, R. (2018). Impact of atmospheric circulation types on southwest asian dust and indian summer monsoon rainfall. *Atmospheric Research*, 201:189 – 205.

Khade, V. M., Hansen, J. A., Reid, J. S., and Westphal, D. L. (2013). Ensemble filter based estimation of spatially distributed parameters in a mesoscale dust model: experiments with simulated and real data. *Atmospheric Chemistry and Physics*, 13(6):3481–3500.

Knippertz, P. and Stuut, J.-B. W. (2014). Mineral dust. *Springer Dordrecht Heidelberg New York London, doi*, 10:978–94.

Li, G., Bei, N., Cao, J., Wu, J., Long, X., Feng, T., Dai, W., Liu, S., Zhang, Q., and Tie, X. (2017). Widespread and persistent ozone pollution in eastern China during thenonwinter season of 2015: observations and source attributions. *Atmospheric Chemistry and Physics*, 17:2759–2774.

Lin, C., Wang, Z., and Zhu, J. (2008a). An Ensemble Kalman Filter for severe dust storm data assimilation over China. *Atmospheric Chemistry & Physics*, 8:2975–2983.

Lin, C., Zhu, J., and Wang, Z. (2008b). Model bias correction for dust storm forecast using ensemble Kalman filter. *J. Geophys. Res.*, 113(D14):D14306+.

Liu, C., Xiao, Q., and Wang, B. (2008). An Ensemble-Based Four-Dimensional Variational Data Assimilation Scheme. Part I: Technical Formulation and Preliminary Test. *Mon. Wea. Rev.*, 136(9):3363–3373.

Liu, C., Xiao, Q., and Wang, B. (2009). An Ensemble-Based Four-Dimensional Variational Data Assimilation Scheme. Part II: Observing System Simulation Experiments with Advanced Research WRF (ARW). *Mon. Wea. Rev.*, 137(5):1687–1704.

Liu, M., Westphal, D. L., Wang, S., Shimizu, A., Sugimoto, N., Zhou, J., and Chen, Y. (2003). A high-resolution numerical study of the Asian dust storms of April 2001. *J. Geophys. Res.*, 108(D23):8653+.

Lorenc, A. C., Bowler, N. E., Clayton, A. M., Pring, S. R., and Fairbairn, D. (2015). Comparison of hybrid-4denvar and hybrid-4dvar data assimilation methods for global nwp. *Monthly Weather Review*, 143(1):212–229.

Lu, S., Lin, H. X., Heemink, A. W., Fu, G., and Segers, A. J. (2015). Estimation of Volcanic Ash Emissions Using Trajectory-Based 4D-Var Data Assimilation. *Mon. Wea. Rev.*, 144(2):575–589.

Manders, A. M. M., Builtjes, P. J. H., Curier, L., Denier van der Gon, H. A. C., Hendriks, C., Jonkers, S., Kranenburg, R., Kuenen, J., Segers, A. J., Timmermans, R. M. A., Visschedijk, A., Wichink Kruit, R. J., Van Pul, W. A. J., Sauter, F. J., van der Swaluw, E., Swart, D. P. J., Douros, J., Eskes, H., van Meijgaard, E., van Ulft, B., van Velthoven, P., Banzhaf, S., Mues, A., Stern, R., Fu, G., Lu, S., Heemink, A., van Velzen, N., and Schaap, M. (2017). Curriculum vitae of the LOTOS-EUROS (v2.0) chemistry transport model. *Geoscientific Model Development*, 10(11):4145–4173.

Marticorena, B. and Bergametti, G. (1995). Modeling the atmospheric dust cycle: 1. Design of a soil-derived dust emission scheme. *Journal of Geophysical Research: Atmospheres*, pages 16415–16430.

Marticorena, B., Bergametti, G., Aumont, B., Callot, Y., N'Doumé, C., and Legrand, M. (1997). Modeling the atmospheric dust cycle: 2. simulation of saharan dust sources. *Journal of Geophysical Research: Atmospheres*, 102(D4):4387–4404.

Mona, L., Papagiannopoulos, N., Basart, S., Baldasano, J., Binietoglou, I., Cornacchia, C., and Pappalardo, G. (2014). Earlinet dust observations vs. bsc-dream8b modeled profiles: 12-year-long systematic comparison at potenza, italy. *Atmospheric Chemistry and Physics*, 14(16):8781–8793.

Morcrette, J.-J., Beljaars, A., Benedetti, A., Jones, L., and Boucher, O. (2008a). Sea-salt and dust aerosols in the ecmwf ifs model. *Geophysical Research Letters*, 35(24).

Morcrette, J.-J., Boucher, O., Jones, L., Salmond, D., Bechtold, P., Beljaars, A., Benedetti, A., Bonet, A., Kaiser, J., Razinger, M., Schulz, M., Serrar, S., Simmons, A., Sofiev, M., Suttie, M., Tompkins, A., Untch, A., and the GEMS-AER team (2008b). Aerosol analysis and forecast in the ecmwf integrated forecast system: Forward modelling.

Morcrette, J.-J., Boucher, O., Jones, L., Salmond, D., Bechtold, P., Beljaars, A., Benedetti, A., Bonet, A., Kaiser, J. W., Razinger, M., Schulz, M., Serrar, S., Simmons, A. J., Sofiev, M., Suttie, M., Tompkins, A. M., and Untch, A. (2009). Aerosol analysis and forecast in the european centre for medium-range weather forecasts integrated forecast system: Forward modeling. *Journal of Geophysical Research: Atmospheres*, 114(D6).

Niu, T., Gong, S. L., Zhu, G. F., Liu, H. L., Hu, X. Q., Zhou, C. H., and Wang, Y. Q. (2008). Data assimilation of dust aerosol observations for the CUACE/dust forecasting system. *Atmospheric Chemistry and Physics*, 8(13):3473–3482.

Ozer, P., Laghdaf, M., Lemine, S., and Gassani, J. (2007). Estimation of air quality degradation due to Saharan dust at Nouakchott, Mauritania, from horizontal visibility data. *Water, Air, and Soil Pollution*, 178(1-4):79–87.

Prospero, J. M., Ginoux, P., Torres, O., Nicholson, S. E., and Gill, T. E. (2002). Environmental characterization of global sources of atmospheric soil dust identified with the nimbus 7 total ozone mapping spectrometer (toms) absorbing aerosol product. *Reviews of Geophysics*, 40(1):2–1–2–31.

Pérez, C., Nickovic, S., Baldasano, J. M., Sicard, M., Rocadenbosch, F., and Cachorro, V. E. (2006). A long saharan dust event over the western mediterranean: Lidar, sun photometer observations, and regional dust modeling. *Journal of Geophysical Research: Atmospheres*, 111(D15).

Schutgens, N., Nakata, M., and Nakajima, T. (2012). Estimating Aerosol Emissions by Assimilating Remote Sensing Observations into a Global Transport Model. *Remote Sensing*, 4(11):3528–3543.

Sekiyama, T. T., Tanaka, T. Y., Shimizu, A., and Miyoshi, T. (2010). Data assimilation of CALIPSO aerosol observations. *Atmospheric Chemistry and Physics*, 10:39–49.

Sekiyama, T. T., Yumimoto, K., Tanaka, T. Y., Nagao, T., Kikuchi, M., and Murakami, H. (2016). Data Assimilation of Himawari-8 Aerosol Observations: Asian Dust Forecast in June 2015. *SOLA*, 12(0):86–90.

Shao, Y., Klose, M., and Wyrwoll, K.-H. (2013). Recent global dust trend and connections to climate forcing. *Journal of Geophysical Research: Atmospheres*, 118(19):11,107–11,118.

Shao, Y., Wyrwoll, K.-H., Chappell, A., Huang, J., Lin, Z., McTainsh, G. H., Mikami, M., Tanaka, T. Y., Wang, X., and Yoon, S. (2011). Dust cycle: An emerging core theme in earth system science. *Aeolian Research*, 2(4):181 – 204.

Shao, Y. P. and Dong, C. H. (2006). A review on East Asian dust storm climate, modelling and monitoring. *Global and Planetary Change*, 52(1-4):1–22.

Shao, Y. P., Raupach, M. R., and Leys, J. F. (1996). A model for predicting aeolian sand drift and dust entrainment on scales from paddock to region. *Australian Journal of Soil Research*, 34(3):309+.

Talagrand, O. (1997). Assimilation of observations, an introduction (gtspecial issueltdata assimilation in meteology and oceanography: Theory and practice). *Journal of the Meteorological Society of Japan. Ser. II*, 75(1B):191–209.

Timmermans, R., Kranenburg, R., Manders, A., Hendriks, C., Segers, A., Dammers, E., Zhang, Q., Wang, L., Liu, Z., Zeng, L., Denier van der Gon, H., and Schaap, M. (2017). Source apportionment of PM2.5 across China using LOTOS-EUROS. *Atmospheric Environment*.

UNEP., WMO., and UNCCD (2016). *Global Assessment of Sand and Dust Storms. United Nations Environment Programme*. Nairobi.

Uno, I., Wang, Z., Chiba, M., Chun, Y. S., Gong, S. L., Hara, Y., Jung, E., Lee, S. S., Liu, M., Mikami, M., Music, S., Nickovic, S., Satake, S., Shao, Y., Song, Z., Sugimoto, N., Tanaka, T., and Westphal, D. L. (2006). Dust model intercomparison (DMIP) study over Asia: Overview. *J. Geophys. Res.*, 111(D12):D12213+.

Wang, Y. Q., Zhang, X. Y., Gong, S. L., Zhou, C. H., Hu, X. Q., Liu, H. L., Niu, T., and Yang, Y. Q. (2008). Surface observation of sand and dust storm in East Asia and its application in CUACE/Dust. *Atmospheric Chemistry and Physics*, 8(3):545–553.

Wang, Z., Ueda, H., and Huang, M. (2000). A deflation module for use in modeling long-range transport of yellow sand over East Asia. *J. Geophys. Res.*, 105(D22):26947–26959.

Winker, D. M., Hunt, W. H., and McGill, M. J. (2007). Initial performance assessment of caliop. *Geophysical Research Letters*, 34(19).

WMO (2017). WMO AIRBORNE DUST BULLETIN: Sand and Dust Storm Warning Advisory and Assessment System. Technical report.

WMO (2018). WMO AIRBORNE DUST BULLETIN: Sand and Dust Storm Warning Advisory and Assessment System. Technical report.

WMO (2019). WMO AIRBORNE DUST BULLETIN: Sand and Dust Storm Warning Advisory and Assessment System. Technical report.

Wu, C., Lin, Z., He, J., Zhang, M., Liu, X., Zhang, R., and Brown, H. (2016). A process-oriented evaluation of dust emission parameterizations in CESM: Simulation of a typical severe dust storm in East Asia. *Journal of Advances in Modeling Earth Systems*, 8(3):1432–1452.

Yumimoto, K., Murakami, H., Tanaka, T. Y., Sekiyama, T. T., Ogi, A., and Maki, T. (2016a). Forecasting of Asian dust storm that occurred on May 10–13, 2011, using an ensemble-based data assimilation system. *Particuology*, 28:121–130.

Yumimoto, K., Nagao, T. M., Kikuchi, M., Sekiyama, T. T., Murakami, H., Tanaka, T. Y., Ogi, A., Irie, H., Khatri, P., Okumura, H., Arai, K., Morino, I., Uchino, O., and Maki, T. (2016b). Aerosol data assimilation using data from Himawari-8, a next-generation geostationary meteorological satellite. *Geophys. Res. Lett.*, 43(11):2016GL069298+.

Yumimoto, K. and Takemura, T. (2015). Long-term inverse modeling of Asian dust: Interannual variations of its emission, transport, deposition, and radiative forcing. *J. Geophys. Res. Atmos.*, 120(4):2014JD022390+.

Yumimoto, K., Uno, I., Sugimoto, N., Shimizu, A., Liu, Z., and Winker, D. M. (2008). Adjoint inversion modeling of Asian dust emission using lidar observations. *Atmospheric Chemistry and Physics*, 8(11):2869–2884.

Zhang, X. X., Sharratt, B., Liu, L. Y., Wang, Z. F., Pan, X. L., Lei, J. Q., Wu, S. X., Huang, S. Y., Guo, Y. H., Li, J., Tang, X., Yang, T., Tian, Y., Chen, X. S., Hao, J. Q., Zheng, H. T., Yang, Y. Y., and Lyu, Y. L. (2018). East Asian dust storm in May 2017: observations, modelling, and its influence on the Asia-Pacific region. *Atmospheric Chemistry and Physics*, 18(11):8353–8371.

Zhao, T. L., Gong, S. L., Zhang, X. Y., Abdel-Mawgoud, A., and Shao, Y. P. (2006). An assessment of dust emission schemes in modeling east Asian dust storms. *Journal of Geophysical Research*, 111(D5):D05S90+.

Zhou, C. H., Gong, S. L., Zhang, X. Y., Wang, Y. Q., Niu, T., Liu, H. L., Zhao, T. L., Yang, Y. Q., and Hou, Q. (2008). Development and evaluation of an operational SDS forecasting system for East Asia: CUACE/Dust. *Atmospheric Chemistry and Physics*, 8(4):787–798.

2

LOTOS-EUROS CHEMICAL TRANSPORT MODEL AND DUST STORM EMISSION

A dynamic model is in need to simulate the life cycles of dust storms.

In large-scale dust modeling systems, the representation of dust emission remains relatively crude which limits the forecast of these models.

Emission inversion using data assimilation can reconstruct the imperfect emission field by incorporating available measurements. Errors in the dust emission parameterization need to be identified to define the likely estimates.

Parts of this chapter have been published in Jin et al. (2018):
Spatially varying parameter estimation for dust emissions using reduced-tangent-linearization 4DVar.
Atmospheric Environment, 187, 358-373;
and in Jin et al. (2019):
Dust Emission Inversion Using Himawari-8 AODs Over East Asia: An Extreme Dust Event in May 2017.
Journal of Advances in Modeling Earth Systems, 11(2):446-467.

2.1. LOTOS-EUROS CHEMICAL TRANSPORT MODEL

In this thesis, the LOTOS-EUROS regional chemical transport model (CTM) is used to simulate the dust storms over East Asia. LOTOS–EUROS model has been developed by a consortium of institutes in the Netherlands. The model system originates from a merge of two dynamic models, Long-Term Ozone Simulation (LOTOS) and European Operational Smog model (EUROS). These two model systems were developed individually since the 1980s at Netherlands Organization for Applied Scientific Research (TNO) and National Institute for Public Health and the Environment (RIVM) (Schaap et al., 2008). Over the past 10 years, LOTOS-EUROS has received new or revised parameterizations and additional functionalities (Manders et al., 2017).

LOTOS-EUROS has been used for a wide range of applications supporting scientific research, regulatory programs and air quality forecasts both inside and outside Europe (Manders et al., 2017). At present, LOTOS-EUROS operational forecasts over China are also released via the MarcoPolo-Panda projects (Brasseur et al., 2019, Petersen et al., 2019, Timmermans et al., 2017) through the link[1]. Besides, it is also implemented in the WMO Sand and Dust Storm Warning Advisory and Assessment System to provide short-time forecast of the dust loading over the North Africa-Middle East-Europe (NA-ME-E) areas, the online forecast product are delivered through the link[2].

In this study, the model only simulates mineral dust from the deserts, since the focus is on estimation of dust emissions for cases with two extreme dust storm events in East Asia. Although in urbanized areas in this region the amount of non-dust aerosols could be substantial, reaching values up to 500 $\mu g/m^3$ (Shao et al., 2018). For the events that are studied these amounts are relative small compared to the observed dust concentration. Simulations of non-dust aerosols are only used in Chapter 4 to remove the non-dust bias from the PM_{10} observations.

2.1.1. MODEL CONFIGURATIONS

To establish a dust simulation system over East Asia, the LOTOS-EUROS model is configured on a domain from 15°N to 50°N and 70°E to 140°E as shown in Fig. 2.1, with a resolution about 0.50°× 0.50°in our first piece of work (Chapter 3), and a finer resolution 0.25°× 0.25°in our following research (Chapter 4 to Chapter 6). Vertically, the model consists of 8 mixing layers with a top at 10 km. The model is driven by European Center for Medium-Ranged Weather Forecast (ECMWF) operational forecasts for forecast steps of 3-12 hours, starting from the 00:00 and 12:00 analyses. The data is extracted from the archive at regular longitude/latitude grid of about 7 km resolution. Physical processes included are advection, diffusion, dry and wet deposition, and sedimentation. More details regarding the LOTOS-EUROS can be found in (Manders et al., 2017), and an open-source version of the model can be acquired through the website[3].

[1] http://www.marcopolo-panda.eu/forecast/ (last access: July 2019)
[2] http://sds-was.aemet.es/forecast-products/dust-forecasts/compared-dust-forecasts (last access: July 2019)
[3] https://lotos-euros.tno.nl/

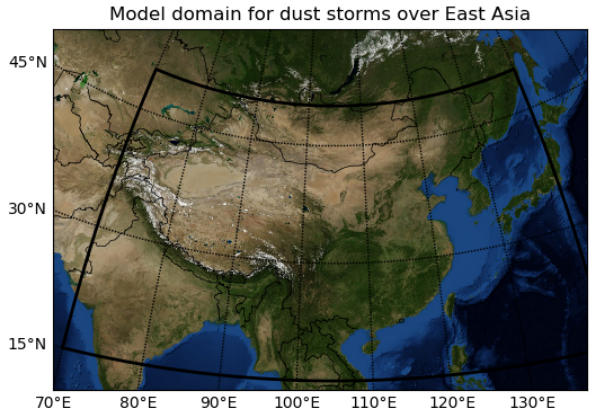

Figure 2.1: LOTOS-EUROS model domain for dust storms over East Asia

2.1.2. DUST AEROSOL DESCRIPTION

The dust emission parametrization describes the flux of dust aerosols from the surface to the first model layer. The flux of very fine particles is insignificant because wind shear force for those small particles is in general small compared to inter-particle adhesion. On the other side of the size spectrum, coarse grains are able to be lifted from the surface, but the continuous drag is not sufficient to lift the weight, and they easily drop down back to the surface. Thus in this thesis, only the soil particles within a diameter range $0.01\mu\text{m} < D_p < 10\ \mu\text{m}$ are considered, and the dust load is described by 5 aerosol bins as shown in Table.2.1. Another reason to exclude larger size bins in this work is that PM_{10} observations either for assimilation or for validation also measure the aerosols with a maximum diameter 10 μm. Similar aerosol size range setting can be found in dust model NMMB-MONARCH (Di Tomaso et al., 2017) and BSC-DREAM8b (Mona et al., 2014).

Table 2.1: Dust aerosol size distribution in LOTOS-EUROS.

Bins	dust_ff	dust_f	dust_ccc	dust_cc	dust_c
Diameter range (μm)	0.01 to 1	1 to 2.5	2.5 to 4	4 to 7	7 to 10

2.1.3. DUST EMISSION PARAMETRIZATION

The windblown dust emission that results in the release of aerosols from soil particles is a complex process. It involves the contribution from soil particle (size distribution, sand/clay/silt texture composition), surface state (vegetation cover, surface roughness, soil moisture, and terrain) and meteorology (friction velocity). It is a key component in dust modeling system and in general an important source of natural aerosols.

Much efforts have been devoted to complete micro-physical specifications of the erodible environment to predict the saltation mass flux and resulting sandblasted dust emissions using either wind tunnel tests or field experiments (Alfaro et al., 1997, Fécan et al., 1999, Marticorena and Bergametti, 1995, Shao et al., 1996). In those parameteri-

zation schemes, the dust emission flux f is mainly governed by atmospheric circulation which is quantified by friction velocity (u_*), and land surface/soil properties that reflect the soil erodibility (Darmenova et al., 2009). The dust emission starts only when the friction velocity overcomes the threshold to initiate the surface particle saltation (see Fig. 2.2). The soil erodibility is quantified by the size-dependent friction velocity threshold (FVT, u_{*t}) which is defined as the minimum friction velocity required to initialize the motion of the soil particles.

Those existing parameterizations were already validated with a high credibility either in wind tunnel tests or in simulations for case studies. However, the representation of those dust emission schemes in regional and global atmospheric models are still limited. The difficulty in accurately modeling the dust emission are explained in Chapter. 2.2.

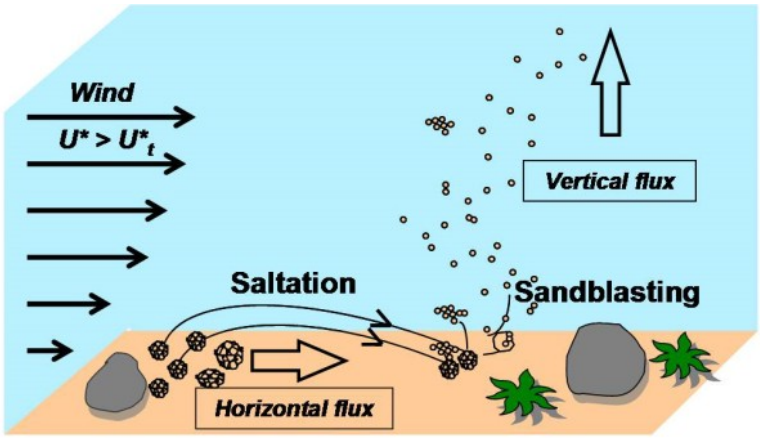

Figure 2.2: Schema representing the key processes for the production of desert aerosols. Source: LISA

2.1.4. DUST EMISSION IN LOTOS-EUROS

The physical basis of the dust emission model adopted in LOTOS-EUROS is the parameterization scheme by Marticorena and Bergametti (1995). The dust flux rate f is calculated as a function of horizontal saltation $\mathcal{F}_h$, the sandblasting efficiency α (Shao et al., 1996), a terrain preference $\mathcal{S}$, and an erodible surface fraction $\mathcal{C}$ as:

$$f = \mathcal{F}_h \cdot \alpha \cdot \mathcal{S} \cdot \mathcal{C} \tag{2.1}$$

The horizontal saltation $\mathcal{F}_h$ represents the horizontal flux rate, which is proportional to the third power of the wind friction velocity u_*, as long as this exceeds a certain friction velocity threshold u_{*t}. Explicitly, $\mathcal{F}_h$ in a given grid cell is computed from:

$$\mathcal{F}_h = \begin{cases} 0 & u_* \le u_{*t} \\ \frac{\rho_a}{g}\, u_*^3 \,(1+\frac{u_{*t}}{u_*})\,(1-\frac{u_{*t}^2}{u_*^2}) & u_* > u_{*t} \end{cases} \tag{2.2}$$

where g denotes the gravitational constant, and ρ_a represents the atmospheric density. The friction velocity u_* is computed from the ECMWF wind speed at 10 m height assuming neutral atmospheric stability, following a logarithmic profile. The friction velocity

threshold (FVT) u_{*t} represents the minimum friction velocity to initiate the movement of soil particles. It is derived first for an idealized dry and smooth surface, and then refined using two correction factors that describe the actual situation in a grid cell:

$$u_{*t} = u_{*ts} \cdot \frac{f_w}{f_r} \tag{2.3}$$

where f_w and f_r are the correction terms of soil moisture and surface roughness elements to the FVT over an idealized dry and smooth surface (u_{*ts}). The soil moisture affects the soil erodibility by enhancing the inter-particle cohesive force. High soil moisture means that particles will glue together and become more difficult to mobilize. The parameterization of soil moisture correction term f_w in Fécan et al. (1999) is formulated as:

$$f_w = \begin{cases} 1, & w \le w'(c) \\ \sqrt{1 + 1.21(100w - 100w'(c))^{0.68}}, & w > w'(c) \end{cases} \tag{2.4}$$

where w is the gravimetric soil water moisture fraction which is also from a ECMWF dynamic product. and w' represents the soil moisture threshold that is only determined by the clay fraction c of the soil, the database of which is derived from the fifth generation Penn State/NCAR Mesoscale Model, (MM5). The surface roughness correction term is calculated as:

$$f_r = 1 - \frac{\ln(\frac{z_0}{z_{0s}})}{\ln[0.35 \cdot (\frac{0.1}{z_{0s}})^{0.8}]} \tag{2.5}$$

where z_0 (cm) and z_{0s}(cm) are the roughness length for momentum and the smooth roughness length, respectively. The roughness length z_0 is mainly determined by the surface landuse while the latter is set as a constant value of 30 μm.

Of the other factors in Eq. 2.1, the sandblasting efficiency α is determined by the average diameter of the soil particles in saltation and the average diameter of suspended particles.

$$\alpha = \frac{2}{3} \cdot \frac{\rho_p}{\rho_a} \cdot \frac{\tau\, \gamma\, g}{[u_{*t}(D_a)]^2} \tag{2.6}$$

where ρ_p represents the aerosol particle density, which is usually set as the constant value ($2.65 \cdot 10^3 \cdot$ kg$\cdot$ m^3), and ρ_a denotes the air density, γ is a constant usually set as 2.5, $u_{*t}(D_a)$ is the friction velocity for the suspended dust particle with an average diameter of D_a (6.7 μm). The τ is set as a constant dependent on the averge diameter of soil particles and aerosol particles as:

$$\tau = [0.125 \cdot 10^{-4} \cdot \ln(D_p) + 0.328 \cdot 10^{-4}] \cdot \exp(-140.7 \cdot D_a + 0.37) \tag{2.7}$$

Here D_p represents the average diameter of the dust particles in saltation (75 μm).

The terrain preference $\mathcal{S}$ is referred as the probability of having accumulated sediments in a given model cell (Ginoux et al., 2001), calculated as:

$$\mathcal{S}_i = \frac{z_{\max} - z_i}{z_{\max} - z_{\min}} \tag{2.8}$$

where the z_i denotes the elevation of the given grid cell i, while $z_{\max}$ and $z_{\min}$ represent the maximum and minimum elevations in the surrounding 10°$\times$ 10°area, respectively.

The current configuration assumes that only areas identified as barren surfaces in the landuse maps allow wind blown dust emissions, while all vegetated or water covered surfaces are considered as non-erodible. The fraction of barren surface $\mathcal{C}$ in a grid cell is taken from the Global Land Cover database[4].

2.2. EMISSION ERRORS ANALYSIS

Our LOTOS-EUROS simulation model that includes aforementioned online dust emission parametrization, but also other large-scale CTM/dust systems mentioned in Chapter 1.2, are capable of reproducing many of the observed dust features. They have retrieved valuable information to elucidate the characteristics and trends of the dust storms. Another important application of these models is to forecast dust concentrations over a few hours to a few days in order to quantify the potential impact on society. Although these dust systems have differences in treating the dust emission schemes, surface boundary data (e.g., soil texture, soil moisture, vegetation cover), and meteorological products, it was found that the dust transport patterns from the source region to downwind areas were usually quite similar. However, the simulated dust concentrations sometimes showed a difference of more than two orders of magnitude from each other, as well as from the observations (Huneeus et al., 2011, Niu et al., 2008). The most important reason for such wide scattering of model error is the difficulty in accurately modeling the dust emission (Gong and Zhang, 2008, Uno et al., 2006).

In large-scale CTM systems, the representation of dust emission remains relatively crude. The intrinsic emission errors are induced from a lot of different input sources, the impossibility for the models to resolve the fine-scale variability in wind fields that drives the dust emission, but also insufficient knowledge about the aerosol lifting process itself (Escribano et al., 2016, Foroutan and Pleim, 2017, Foroutan et al., 2017).

In terms of the horizontal flux rate in Eq. 2.2, the friction velocity threshold (FVT, u_{*t}) is very important and sensitive for the outcome, since it directly influences whether dust saltation will occur and also quantifies the amplitude of the flux rate. However, implementation of these FVT parameterization in large-scale models will inevitably cause scale-mismatch issues. For instance, the quantifications of the soil moisture correction term f_w is conducted in wind tunnel experiments, where the soil moisture was determined in the very superficial top layer of the soil (2 cm). However, the regional or global meteorology model are not able to provide the precise soil moisture estimates for a superficial soil layer as thin as those measured in the wind tunnel experiments used to build the FVT parameterization (Bergametti et al., 2016). Due to these reasons, the FVT parameterization included in the existing dust emission models generally gives a mismatch with the observed values (Xi and Sokolik, 2015, Zender, 2003, Zhao et al., 2006). Besides, the imperfect spatial distribution of soil properties (like clay fraction) and surface landuse dataset will also result in the uncertainty of f_w and f_r (Menut et al., 2013), then influences the FVT parameterization. Di Tomaso et al. (2017) considered that the uncertainty of the FVT is the main error source in the dust emission parametrization, and it is was compensated by applying a multiplicative parameter in their study.

Emission errors are also likely to be induced during the formation of the friction ve-

[4] http://forobs.jrc.ec.europa.eu/products/glc2000/

locity (u_*) from meteorology data, the terrain preference ($\mathcal{S}$) from the topography resource, and the erodible surface fraction ($\mathcal{C}$) from the land cover database.

Besides, these deterministic parameterizations are not representative for the stochastic nature of dust emissions. For example, the dust saltation is assumed to occur when u_t exceeds the minimum friction velocity that is needed to initiate a movement of soil particles. However, observations show that within the dust particle size range the threshold friction velocity also scatters widely due to stochastic inter-particle cohesion (Shao and Klose, 2016); in reality there will always be a (small) amount of free moving dust which can be resuspended even by weak wind forces.

The goal of this study is to estimate dust emissions during severe dust events by assimilation of available data. To achieve this, it is necessary to describe the uncertainty in the dust simulations. We assume that the main uncertainty is in the parametrization of the dust emissions. Although other model elements such as transport and deposition also include uncertainties, for the events under study they are assumed to be of less importance than the location and the amount of dust emission. This assumption could be seen as a first step towards a system that takes into account other uncertainties too, but that probably requires additional information such as vertical distributions of the dust load which are currently not available.

For the emission inversion using the data assimilation, both the background emission field and its uncertainty are required. The latter defines the distribution of the deviation from the former. In this thesis, emission error sources from the friction velocity threshold (FVT) and friction velocity (FV) are considered first, and the resulting uncertainty is used in the emission inverse modeling in Chapter 3 (FVT only), Chapter 4 (FVT only) and Chapter 5 (both FVT and FV). The calculated background emission together with the *a priori* are validated to be able to explain the observation-minus-simulation errors in most cases. Errors due to the uncertainties in terrain preference and erodible surface fraction are further introduced in Chapter 6 in order to fully resolve the observation-minus-simulation difference over a local region.

The sensitivity of the dust simulations towards changes in friction velocity threshold and friction velocity is analyzed in Chapter 2.2.2 and Chapter 2.2.1 for the dust event in May 2017. Considering the main drivers of the emission, the emission deviation can be approximated as a linear combination of these two parameters, friction velocity and friction velocity threshold:

$$\delta f \approx \mathcal{F}_{u_*}\, \delta u_* + \mathcal{F}_{u_{*t}}\, \delta u_{*t} \tag{2.9}$$

The linear operators $\mathcal{F}_{u_*}$ and $\mathcal{F}_{u_{*t}}$ approximate the change in emissions given changes in u_* and u_{*t} with respect to a simulation with the default configuration. We assume that the uncertainty in the friction velocity δu_* (which is a property of the meteorology) is independent from the uncertainty in the friction velocity threshold δu_{*t} (which is a property of surface and soil state). Furthermore, we define the vectors $\delta \boldsymbol{u}_*$ and $\delta \boldsymbol{u}_{*t}$, which consist of δu_* and δu_{*t} in the model grid cells respectively, and assume that their uncertainty follows a Gaussian distribution defined by a zero mean and covariance matrices $\mathbf{B}_{u_*}$ and $\mathbf{B}_{u_{*t}}$ respectively. The uncertainty in the vector $\delta \boldsymbol{f}$ with emission perturbations on the grid is then:

$$\mathbf{B} = \mathbf{F}_{u_*}\, \mathbf{B}_{u_*}\, \mathbf{F}_{u_*}^T + \mathbf{F}_{u_{*t}}\, \mathbf{B}_{u_{*t}}\, \mathbf{F}_{u_{*t}}^T \tag{2.10}$$

with $\mathbf{F}_{u_*}$ and $\mathbf{F}_{u_{*t}}$ the matrix operators based on the linearizations.

The emission covariance is not exactly computed as in Eq.2.10 for that require the computation and storage of the two huge-sized uncertainty matrix, $\mathbf{B}_{u_*}$ and $\mathbf{B}_{u_{*t}}$, and the matrix operators $\mathbf{F}_{u_*}$ and $\mathbf{F}_{u_{*t}}$. The two contributions to the covariance of the emission deviation are discussed in the following sections.

2.2.1. UNCERTAINTY IN THE FRICTION VELOCITY

A suitable method to estimate the uncertainty in emissions due to uncertainty in the friction velocity field is to use the variability in the meteorological input. For the ECMWF meteorological forecasts that are used as model input, the variability could be estimated from the ensemble forecast that is available too, where each member is a perturbation of the deterministic forecast. For the studied period the ensemble forecast consists of 26 different members, and each of these has been used with the model to compute dust emissions. These forecast ensemble are valid for prediction horizons of 3-12 hours from the 06:00 and 18:00 analyses, extracted from the archive at a resolution of about 30 km. The ensemble covariance of these emissions is then used to represent for the uncertainty in the emissions due to uncertainty in friction velocity:

$$\mathbf{F}_{u_*}\,\mathbf{B}_{u_*}\,\mathbf{F}_{u_*}^T \approx \frac{1}{N_1-1}\sum_{k=1}^{N_1}\left(\boldsymbol{f}_{u_*,k}-\overline{\boldsymbol{f}}_{u_*}\right)\left(\boldsymbol{f}_{u_*,k}-\overline{\boldsymbol{f}}_{u_*}\right)^T \tag{2.11}$$

where $\boldsymbol{f}_{u_*,k}$ denotes the emission vector computed using meteorological ensemble member k, $\overline{\boldsymbol{f}}_{u_*}$ is the ensemble average, and $N_1 = 26$ is the ensemble size. This ensemble covariance is not computed and stored as a full matrix due to its huge size; instead, the ensemble members are stored and elements of the covariance are evaluated when needed.

2.2.2. UNCERTAINTY IN THE FRICTION VELOCITY THRESHOLD

The parameterization of u_{*t} follows the concept of adding two correction terms to the threshold friction velocity over an idealized dry and smooth surface. One term is for soil moisture, governed by the inputs of soil moisture and soil clay mass fraction, another one is for the non-erodible surface roughness elements, governed by the input of the surface roughness. The imperfect spatially distributed surface states and soil texture dataset are the main reasons for inaccurately modeling the friction velocity threshold in the dust emission parametrization. The errors in the friction velocity thresholds are assumed to be compensated for by introducing a spatially varying multiplicative factor $\boldsymbol{\beta}$. This tuning parameter vector is assumed to follow a Gaussian distribution $\mathcal{N}(\boldsymbol{\beta}_b, \mathbf{B}_\beta)$, of which the details are described in Chapter 3.3.1.

Given the covariance matrix $\mathbf{B}_\beta$, an ensemble of samples of $\boldsymbol{\beta}$ are drawn with a random generator. These ensemble samples are then applied in the dust model, and each of them produces an emission forecast. The covariance of these emission fields are used to approximate the emission uncertainty due to the friction velocity threshold:

$$\mathbf{F}_{u_{*t}}\,\mathbf{B}_{u_{*t}}\,\mathbf{F}_{u_{*t}}^T \approx \frac{1}{N_2-1}\sum_{k=1}^{N_2}\left(\boldsymbol{f}_{u_{*t},k}-\overline{\boldsymbol{f}}_{u_{*t}}\right)\left(\boldsymbol{f}_{u_{*t},k}-\overline{\boldsymbol{f}}_{u_{*t}}\right)^T \tag{2.12}$$

where $\boldsymbol{f}_{u_{*t},k}$ represents the emission vector computed using friction velocity threshold ensemble member k, $\overline{\boldsymbol{f}}_{u_{*t}}$ is the ensemble average, and N_2 is the friction velocity threshold sample size, which is chosen to be 100 in this study.

2.2.3. COMPARISON OF UNCERTAINTIES

To estimate the relative importance of the two contributions to the emission uncertainty, an emission integration index $\mathcal{F}_i$ (g/m^2) is defined that represents the accumulated dust emission in a cell i from 15:00 May 2 to 15:00 May 4 2017, the period that completely covers the severe dust storm event studied in Chapter 5 and Chapter 6. The map of deterministic $\mathcal{F}_i$ can be found in Fig. 2.3(a), while the map in Fig. 2.3(b) presents the evaluated standard deviations from the parameterized uncertainties based on the meteorological ensemble and samples of β factors drawn with a random generator over the potential source region. The maps show that the variability in emissions due to uncertainty in friction velocity Fig. 2.3(c) is relatively small compared to the variability due to uncertainty in friction velocity threshold Fig. 2.3(d). The total standard deviation is therefore mainly caused by the uncertain soil parameters in this study case. However, the uncertainty in the wind field might have considerable contribution to the emission uncertainty during other dust storms.

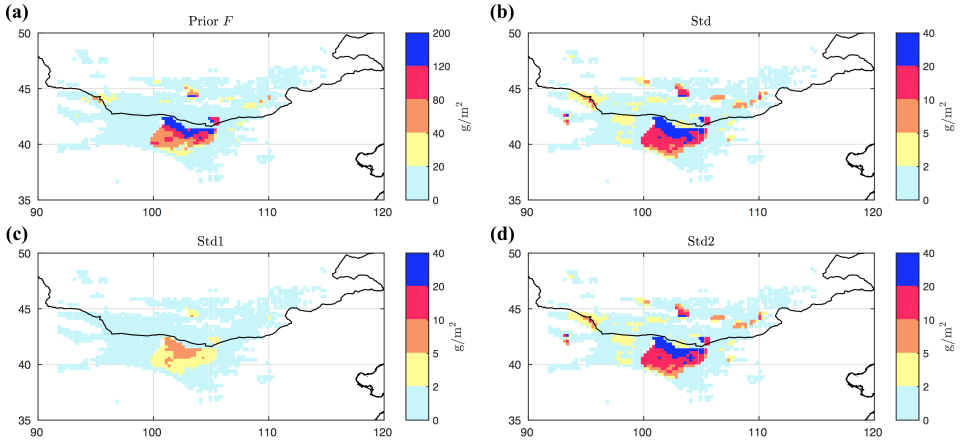

Figure 2.3: (a):Prior emission index $\mathcal{F}$; (b): standard deviation (Std) of the emission index $\mathcal{F}$ from 15:00 May 02 to 15:00 May 04 2017; (c: Std of F due to the perturbation in wind field; (d): in FVT map

2.3. CONCLUSIONS

The regional CTM LOTOS-EUROS is configured to simulate dust storms over East Asia. The errors in the emission parametrization are analyzed. They are identified to be caused by the uncertainties in a lot of different inputs e.g., wind fields referred as friction velocity, soil and surface properties represented by friction velocity threshold. The relative importance of these two key contributions to the emission uncertainty are evaluated. The results show that the variability in emissions due to uncertainty in friction veloc-

ity is relatively small compared to the variability due to uncertainty in friction velocity threshold. The total standard deviation is therefore mainly caused by the uncertain soil and surface parameters in our test case.

REFERENCES

Alfaro, S. C., Gaudichet, A., Gomes, L., and Maillé, M. (1997). Modeling the size distribution of a soil aerosol produced by sandblasting. *J. Geophys. Res.*, 102(D10):11239–11249.

Bergametti, G., Rajot, J. L., Pierre, C., Bouet, C., and Marticorena, B. (2016). How long does precipitation inhibit wind erosion in the Sahel? *Geophys. Res. Lett.*, 43(12):2016GL069324+.

Brasseur, G. P., Xie, Y., Petersen, A. K., Bouarar, I., Flemming, J., Gauss, M., Jiang, F., Kouznetsov, R., Kranenburg, R., Mijling, B., Peuch, V.-H., Pommier, M., Segers, A., Sofiev, M., Timmermans, R., van der A, R., Walters, S., Xu, J., and Zhou, G. (2019). Ensemble forecasts of air quality in eastern china – part 1: Model description and implementation of the marcopolo–panda prediction system, version 1. *Geoscientific Model Development*, 12(1):33–67.

Darmenova, K., Sokolik, I. N., Shao, Y., Marticorena, B., and Bergametti, G. (2009). Development of a physically based dust emission module within the Weather Research and Forecasting (WRF) model: Assessment of dust emission parameterizations and input parameters for source regions in Central and East Asia. *J. Geophys. Res.*, 114(D14):D14201+.

Di Tomaso, E., Nick, Jorba, O., and Garcia-Pando, C. P. (2017). Assimilation of MODIS Dark Target and Deep Blue observations in the dust aerosol component of NMMB-MONARCH version 1.0. *Geoscientific Model Development*, 10:1107–1129.

Escribano, J., Boucher, O., Chevallier, F., and Huneeus, N. (2016). Subregional inversion of North African dust sources. *Journal of Geophysical Research: Atmospheres*, 121(14):8549–8566.

Fécan, F., Marticorena, B., and Bergametti, G. (1999). Parametrization of the increase of the aeolian erosion threshold wind friction velocity due to soil moisture for arid and semi-arid areas. *Annales Geophysicae*, 17(1):149+.

Foroutan, H. and Pleim, J. E. (2017). Improving the simulation of convective dust storms in regional-to-global models. *Journal of Advances in Modeling Earth Systems*, 9(5):2046–2060.

Foroutan, H., Young, J., Napelenok, S., Ran, L., Appel, K. W., Gilliam, R. C., and Pleim, J. E. (2017). Development and evaluation of a physics-based windblown dust emission scheme implemented in the CMAQ modeling system. *Journal of Advances in Modeling Earth Systems*, 9(1):585–608.

Ginoux, P., Chin, M., Tegen, I., Prospero, J. M., Holben, B., Dubovik, O., and Lin, S.-J. (2001). Sources and distributions of dust aerosols simulated with the GOCART model. *J. Geophys. Res.*, 106(D17):20255–20273.

Gong, S. L. and Zhang, X. Y. (2008). CUACE/Dust – an integrated system of observation and modeling systems for operational dust forecasting in Asia. *Atmospheric Chemistry and Physics*, 8(9):2333–2340.

Huneeus, N., Schulz, M., Balkanski, Y., Griesfeller, J., Prospero, J., Kinne, S., Bauer, S., Boucher, O., Chin, M., Dentener, F., Diehl, T., Easter, R., Fillmore, D., Ghan, S., Ginoux, P., Grini, A., Horowitz, L., Koch, D., Krol, M. C., Landing, W., Liu, X., Mahowald, N., Miller, R., Morcrette, J. J., Myhre, G., Penner, J., Perlwitz, J., Stier, P., Takemura, T., and Zender, C. S. (2011). Global dust model intercomparison in AeroCom phase I. *Atmospheric Chemistry and Physics*, 11(15):7781–7816.

Jin, J., Lin, H. X., Heemink, A., and Segers, A. (2018). Spatially varying parameter estimation for dust emissions using reduced-tangent-linearization 4DVar. *Atmospheric Environment*, 187:358–373.

Jin, J., Segers, A., Heemink, A., Yoshida, M., Han, W., and Lin, H.-X. (2019). Dust Emission Inversion Using Himawari-8 AODs Over East Asia: An Extreme Dust Event in May 2017. *Journal of Advances in Modeling Earth Systems*, 11(2):446–467.

Manders, A. M. M., Builtjes, P. J. H., Curier, L., Denier van der Gon, H. A. C., Hendriks, C., Jonkers, S., Kranenburg, R., Kuenen, J., Segers, A. J., Timmermans, R. M. A., Visschedijk, A., Wichink Kruit, R. J., Van Pul, W. A. J., Sauter, F. J., van der Swaluw, E., Swart, D. P. J., Douros, J., Eskes, H., van Meijgaard, E., van Ulft, B., van Velthoven, P., Banzhaf, S., Mues, A., Stern, R., Fu, G., Lu, S., Heemink, A., van Velzen, N., and Schaap, M. (2017). Curriculum vitae of the LOTOS-EUROS (v2.0) chemistry transport model. *Geoscientific Model Development*, 10(11):4145–4173.

Marticorena, B. and Bergametti, G. (1995). Modeling the atmospheric dust cycle: 1. Design of a soil-derived dust emission scheme. *Journal of Geophysical Research: Atmospheres*, pages 16415–16430.

Menut, L., Pérez, C., Haustein, K., Bessagnet, B., Prigent, C., and Alfaro, S. (2013). Impact of surface roughness and soil texture on mineral dust emission fluxes modeling. *J. Geophys. Res. Atmos.*, 118(12):6505–6520.

Mona, L., Papagiannopoulos, N., Basart, S., Baldasano, J., Binietoglou, I., Cornacchia, C., and Pappalardo, G. (2014). EARLINET dust observations vs. BSC-DREAM8b modeled profiles: 12-year-long systematic comparison at Potenza, Italy. *Atmospheric Chemistry and Physics*, 14(16):8781–8793.

Niu, T., Gong, S. L., Zhu, G. F., Liu, H. L., Hu, X. Q., Zhou, C. H., and Wang, Y. Q. (2008). Data assimilation of dust aerosol observations for the CUACE/dust forecasting system. *Atmospheric Chemistry and Physics*, 8(13):3473–3482.

Petersen, A. K., Brasseur, G. P., Bouarar, I., Flemming, J., Gauss, M., Jiang, F., Kouznetsov, R., Kranenburg, R., Mijling, B., Peuch, V.-H., Pommier, M., Segers, A., Sofiev, M., Timmermans, R., van der A, R., Walters, S., Xie, Y., Xu, J., and Zhou, G. (2019). Ensemble forecasts of air quality in eastern china – part 2: Evaluation of the marcopolo–panda prediction system, version 1. *Geoscientific Model Development*, 12(3):1241–1266.

Schaap, M., Timmermans, R., Roemer, M. G. M., Boersen, G. A. C., Builtjes, P. J. H., Sauter, F., Velders, G. J. M., and Beck, J. P. (2008). The lotos-euros model: description, validation and latest developments. *International Journal of Environment and Pollution*, 32(2).

Shao, P., Tian, H., Sun, Y., Liu, H., Wu, B., Liu, S., Liu, X., Wu, Y., Liang, W., Wang, Y., Gao, J., Xue, Y., Bai, X., Liu, W., Lin, S., and Hu, G. (2018). Characterizing remarkable changes of severe haze events and chemical compositions in multi-size airborne particles (PM1, PM2.5 and PM10) from January 2013 to 2016–2017 winter in Beijing, China. *Atmospheric Environment*, 189:133–144.

Shao, Y. and Klose, M. (2016). A note on the stochastic nature of particle cohesive force and implications to threshold friction velocity for aerodynamic dust entrainment. *Aeolian Research*, 22:123–125.

Shao, Y. P., Raupach, M. R., and Leys, J. F. (1996). A model for predicting aeolian sand drift and dust entrainment on scales from paddock to region. *Australian Journal of Soil Research*, 34(3):309+.

Timmermans, R., Kranenburg, R., Manders, A., Hendriks, C., Segers, A., Dammers, E., Zhang, Q., Wang, L., Liu, Z., Zeng, L., Denier van der Gon, H., and Schaap, M. (2017). Source apportionment of PM2.5 across China using LOTOS-EUROS. *Atmospheric Environment*.

Uno, I., Wang, Z., Chiba, M., Chun, Y. S., Gong, S. L., Hara, Y., Jung, E., Lee, S. S., Liu, M., Mikami, M., Music, S., Nickovic, S., Satake, S., Shao, Y., Song, Z., Sugimoto, N., Tanaka, T., and Westphal, D. L. (2006). Dust model intercomparison (DMIP) study over Asia: Overview. *J. Geophys. Res.*, 111(D12):D12213+.

Xi, X. and Sokolik, I. N. (2015). Seasonal dynamics of threshold friction velocity and dust emission in Central Asia. *Journal of Geophysical Research: Atmospheres*, 120(4):1536–1564.

Zender, C. S. (2003). Mineral Dust Entrainment and Deposition (DEAD) model: Description and 1990s dust climatology. *Journal of Geophysical Research*, 108(D14):4416+.

Zhao, T. L., Gong, S. L., Zhang, X. Y., Abdel-Mawgoud, A., and Shao, Y. P. (2006). An assessment of dust emission schemes in modeling east Asian dust storms. *Journal of Geophysical Research*, 111(D5):D05S90+.

3

REDUCED-TANGENT-LINEARIZATION 4DVAR

In this Chapter, an integrated dust emission inversion system - LOTOS-EUROS/dust coupled with a reduced-tangent-linearization 4DVar data assimilation has been developed. Errors in dust storm models are assumed to be caused by the inflexibility and inaccuracy of the existing friction velocity threshold parameterization in dust emission. A spatially varying multiplicative factor for the threshold is introduced. This parameter is estimated by assimilating measurements from a field station network established by China Ministry of Environmental Protection. The data assimilation algorithm is adjoint-free, and its computational complexity increases with the number of uncertain parameters. Two model reducing techniques, sensitivity-based parameter filters and proper orthogonal decomposition, are sequentially implemented one after each other, which lead to a reduction of parameter dimension from initially $O(10^4)$ to $O(10^2)$.

Twin experiments are conducted to evaluate the impact of assimilation settings on the dust forecast accuracy. In addition, experiments with real observations are conducted. However, these observations also reflect the aerosol concentration from local emissions. To effectively use these observations as representative for dust concentrations, a simple observation bias correction and a variable representation error scheme are designed. Improvements on the dust storm forecast with our system are demonstrated.

This chapter has been published in (Jin et al., 2018):
Sptially varying parameter estimation for dust emissions using reduced-tangent-linearization 4DVar. *Atmospheric Environment*, 187, 358-373.

3.1. INTRODUCTION

FOUR-dimensional variational (4DVar) data assimilation is a powerful method to reconstruct the parameter structure. The aim of 4DVar is to obtain the analysis that optimally fit the observations, and the solution can be obtained by solving a large-scale optimization problem. 4DVar currently implemented in large-scale dynamic models are usually based on an incremental method. In other words, the minimization of the full nonlinear cost function is approximated with the minimization of a series of linearized ones. These linearizations are called tangent linearization (TL) and adjoint model (AM). However, it always requires a huge effort to build and maintain the TL and AM for realistic models.

To alleviate the cost of implementing the TL and AM of the original model, adjoint-free and reduced-tangent-linearization 4DVar methods have been developed, such as inverse modeling using a model reduction approach (Vermeulen and Heemink, 2006, Vermeulen et al., 2005), a proper orthogonal decomposition based (POD-based) 4DVar (Cao et al., 2007, Daescu and Navon, 2008, Lawless et al., 2008). The model reductions in those methods are based on proper orthogonal decomposition (POD) which projects the original model upon the dominant patterns. They provide a lower-order version of the original TL while retaining the key properties.

In this Chapter, we develop an integrated dust emission inversion system, including a regional dust transport model LOTOS-EUROS/dust (Manders et al. (2017)) and reduced-tangent-linearization (RTL) 4DVar data assimilation algorithm. A dust storm event that occurred in April 2015 over East Asia is chosen as a test case. Based on the work of Di Tomaso et al. (2017) and the dust emission error analysis in Chapter 2.2, we assume that the main emission uncertainty is due to the errors in the friction velocity threshold. A spatially varying multiplicative factor (SVMF) is introduced to the friction velocity threshold (FVT) to correct the mismatch in the dust emission scheme.

The SVMF is estimated by the adjoint-free 4DVar using the hourly observations from the field station network established by the China Ministry of Environmental Protection (MEP). The computational cost of the RTL 4DVar depends on the degree of freedom of SVMF. To improve the computational efficiency of the data assimilation algorithm, two model reduction techniques are adopted. Firstly, three SVMF filters (landcover-based, windfield-based and emission-based) are designed, with which the SVMF size is reduced from initially $O(10^4)$ to $O(10^3)$. Then, further reduction is obtained using POD which projects the SVMF onto $O(10^2)$ key patterns. Twin experiments are conducted to evaluate the impact of reduced covariance rank size and SVMF filters on the estimation accuracy. Our system is verified to be capable of correcting the imperfections of FVT map, and results indicate that in this way a more accurate dust emission can be obtained. Furthermore, experiments with real field observations are also performed. However, the ground measurements of dust also reflect background coarse-mode aerosols released in anthropogenic activities, which is referred as bias in this thesis. Thus a statistical observation bias correction (OBC) and a variable representation error is designed which make the observations more representative for the dust. Improvements on the dust simulation are verified.

We improve the dust emission parameterization by applying a spatially varying multiplicative factor (SVMF) to the friction velocity threshold (FVT). The SVMF will be es-

timated using the RTL 4DVar, which is adjoint free. The computation cost of the data assimilation algorithm is proportional to the dimension of FVT. To improve the computational efficiency, two model reduction techniques are designed. This is the first time the field measurements from the China MEP are assimilated, its huge spatial coverage and high temporal resolution are shown to be a promising and powerful source of data for severe dust storm forecast. The dust storm forecast is significantly improved in the experiment using these real observations.

Chapter 3 is organized as follows. The test case, the dust storm event in April 2015, is described in Chapter 3.2. LOTOS-EUROS/dust is also evaluated through a comparison with the field observations and another dust forecast model BSC-DREAM8b. The methodology of the RTL 4DVar is reviewed in Chapter 3.3, and the three SVMF filters are explained. The dust observations as well as the existing bias from the China MEP is introduced in Chapter 3.4. Twin experiments are designed in Chapter 3.5, we investigate the impacts of assimilation settings on the SVMF estimation. The improvements on dust emission, and dust concentration are also evaluated. In Chapter 3.6, the real observations with the OBC and the variable representation error are used in the assimilation experiments. The estimation of SVMF, dust flux and dust concentration is evaluated.

3.2. DUST EVENT IN APRIL 2015

This dust storm emission started on 14, April China Stand Time (CST) in the Mongolia and Gobi desert, the plume was then transported to the downwind regions. At 00:00, 15 April(UTC), the BSC-DREAM8b dust loading shows the main dust plume was in Inner Mongolia province as shown in Fig.3.1(a). Then it was carried towards the southeast direction, and 12 hours later it arrived the Central China as shown in Fig.3.1(b).

Limited by the observation network coverage in the source region, the high-value PM_{10}, caused by the severe dust storm, was observed only by the few stations in Inner Mongolia province at 08:00 (CST), April 15, and most observing sites reported a low-value PM_{10} caused by the non-dust aerosols, as shown in Fig.3.1(c). The field PM_{10} measurements not exactly reflect the dust concentration, but also reflect the non-dust local aerosols. Thus at this non-dust period, the PM_{10} concentration is not zero but at a low level. At 20:00, severe PM_{10} concentration was reported by more than 200 stations as shown in Fig.3.1(d), which is believed to caused by the dust storm.

This dust event is reproduced by LOTOS-EUROS/dust with the similar configurations illustrated in Chapter 2.1.1. In the emission process, the mass content fraction of dust bin 1 takes up less than 0.5% of all dust flux, while bin 5 dominantly has a fraction more than 54%. The mass fraction of bin 2~4 is about 2%, 5.5% and 37%, respectively. Therefore, the aerosols with a diameter larger than 2.5 μm are dominant among all the 5 dust particles. Fig.3.1(e) and (f) show the corresponding dust loading plumes by LOTOS-EUROS, the main part of LOTOS-EUROS dust plume at 8:00 also stayed in Inner Mongolia, but a big tail was already transported to the Central China, which does not match the observations well. Similar to the field measurements and BSC-DREAM8b, the dust loading plume was transported to Central China later. Compared to the simulation by BSC-DREAM8b, the maximum dust loading reproduced by LOTOS-EUROS is about 4 times smaller. Generally, there is difference between the dust simulations by LOTOS-

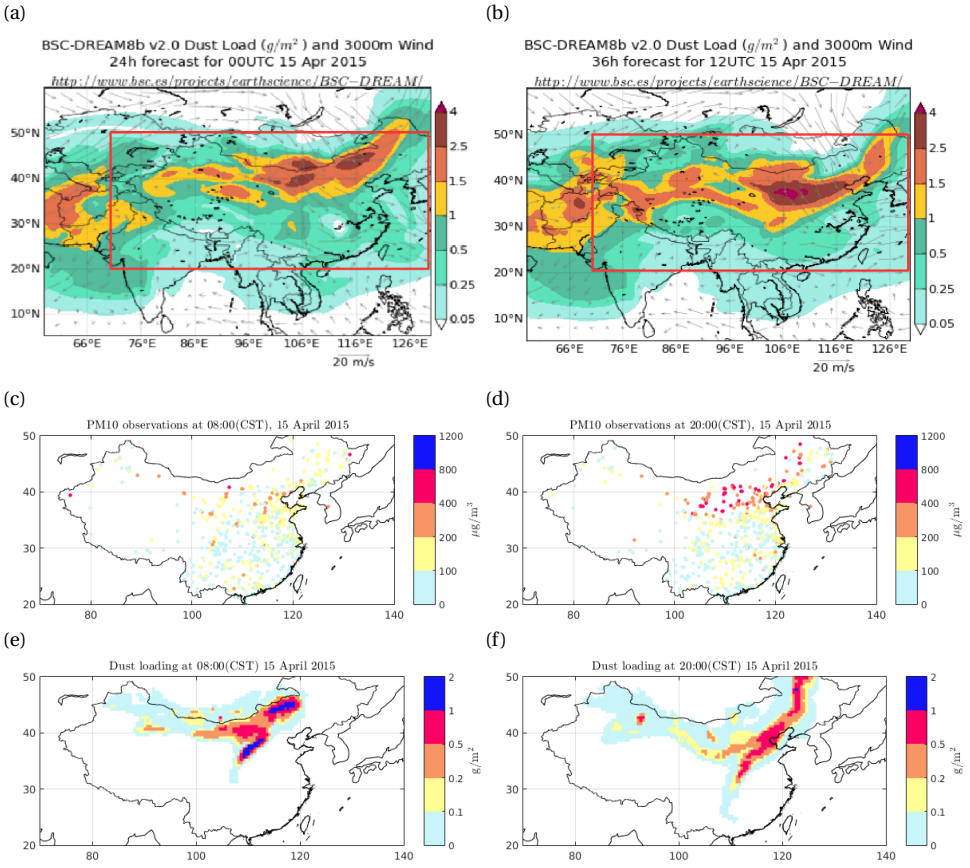

Figure 3.1: China MEP field observations and dust loading simulations: (a)(b)BSC-DREAM8B; (c)(d)PM_{10} ground observations; (e)(f)LOTOS-EUROS at two time snapshots (a)(c)(e) 08:00 (CST) and (b)(d)(f) 20:00 (CST), April 15, 2015.

EUROS, BSC-DREAM8b and the ground observations, but the simulated plume shapes are close to each other, and also similar to the observed PM_{10} from the field observation network. Thus, LOTOS-EUROS with the above configurations is capable of simulating the SDS over East Asia.

3.3. DATA ASSIMILATION SCHEME

3.3.1. SPATIALLY VARYING MULTIPLICATIVE FACTOR (SVMF) FOR FRICTION VELOCITY THRESHOLD (FVT)

In order to correct the mismatch in the friction velocity threshold (FVT) parameterization, a spatially varying multiplicative parameter (SVMF) β is introduced:

$$u_{*t}^{\text{true}}(i,t) = \boldsymbol{\beta}(i) \cdot u_{*t}(i,t) \tag{3.1}$$

where $u_{*t}(i,t)$ is the model parameterized FVT in a given cell i at time t, while $u_{*t}^{\text{true}}(i,t)$ is the true FVT. $\boldsymbol{\beta} \in \mathbf{R}^P$ stores the spatially varying β, and P is in the order of $O(10^4)$.

In the 4DVar system, the tangent linear (TL) model size is proportional to the estimated parameter dimension. The TL is constructed using the perturbation method in this paper, and considered as the most expensive part of the algorithm. To keep the computation time acceptable, the dust emission flux of 5 dust bins in different soil types in the given cell are applied with the same SVMF. The temporal variation of the β map within each assimilation window could be easily implemented in the current system, but treated constant due to the extra computation costs. However, the posterior from one cycle is set to be the prior of next assimilation window, thus, the β map would be temporally variable in case of long run with multiple cycles. The β values here are imposed with a mean of 1.0 and a standard deviation $\sigma = 0.1$. β_{min} and β_{max} are set as 0.7 and 1.3, respectively. Similarly, β is configured with a mean of 1 and a spread of 0.4 by Di Tomaso et al. (2017).

A distance-based spatial correlation $\mathbf{C}(i,j)$ of β is designed by:

$$\mathbf{C}(i,j) = e^{-d_{i,j}^2/2*L^2} \tag{3.2}$$

where $d_{i,j}$ represents the distance of two grid cells i and j, and L is the distance threshold used to build the spatial correlation of β. A small L represents a weak correlation and a high spatially varying freedom level. The value of L is tunable, for the dust event in April 2015 an empirical choice of $L = 800$ km is used. The expected vector $\boldsymbol{\beta}$ has a prior $\boldsymbol{\beta}_b = [1, 1, ..., 1]$ with error $\boldsymbol{\epsilon}_b$ as:

$$\boldsymbol{\beta} = \boldsymbol{\beta}_b + \boldsymbol{\epsilon}_b \tag{3.3}$$

where the background error ϵ_b are assumed to be unbiased and Gaussian distributed, described by a known covariance $\mathbf{B}$ where

$$\mathbf{B}(i,j) = \sigma^2 \cdot \mathbf{C}(i,j) \tag{3.4}$$

3.3.2. SVMF FILTERS

The RTL 4DVar is to seek the optimal solution in the dominant subspace. The computation efficiency of the adjoint-free algorithm depends on the dimension of the subspace. In this paper, two model reduction techniques are implemented together to reduce the original space to a small number of key patterns: the SVMF filters and POD-based covariance reduction. The SVMF filters aim to reduce the parameter space by filtering out the nonsensitive values. Here we have developed three sequentially-implemented SVMF filters (landcover-based, windfield-based and emission-based β filters), these filters only fit the short-term dust storm simulation.

LANDCOVER-BASED SVMF FILTER

In the dust model, the landcover is categorized into several types, like tree cover, shrub cover, water bodies and bare areas. However only the deserts or barren areas are considered as the potential sources. The landcover-based β filter aims to reduce the SVMF space by filtering out the β in the non-source region, while it only enables the β for FVT in the given cell which is a desert or barren area.

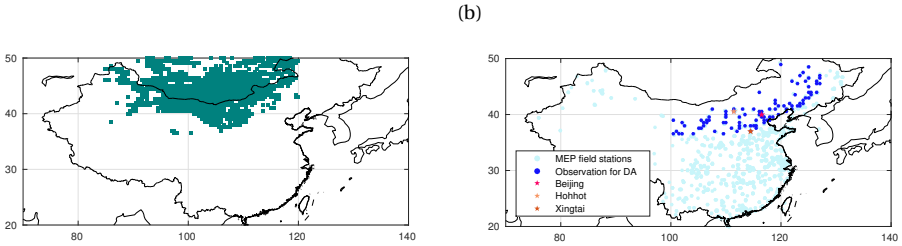

Figure 3.2: (a): Map of the grid cells where β values are defined, as found after the application of the three SVMF filters; (b): the network of field measurement stations

Croplands and rangelands are also the potential sources for dusts. However, a dynamic vegetation growing model is necessary to incorporate these emission processes, thus, these possible emissions are not included yet. For the event under investigation it is also known that the source regions are not croplands or rangelands.

WINDFIELD-BASED SVMF FILTER

Even when the grid cell i is a potential dust emission region (desert or barren areas), the model simulations will only be affected by the $\boldsymbol{\beta}$ when the wind friction velocity $u_*(i,t)$ exceeds the minimum FVT $u_{*t}(i,t)$. Accordingly, the windfield-based β filter is developed in which the β will be enabled only if

$$u_*(i,t) > u_{*t}(i,t) \cdot \beta_{min} \tag{3.5}$$

EMISSION-BASED SVMF FILTER

If the dust emission flux rate $f(i,\beta)$ in a grid cell i is always weak even for $\beta = \beta_{min}$ within the assimilation cycle, then the dust flux can be neglected, the emission is thus not sensitive to the β for such grid cell. Therefore, the emission-based SVMF filter is designed where β will be enabled only if

$$f(i,\beta_{min}) > f_{th} \tag{3.6}$$

f_{th} is the weak dust emission threshold and set as 10 μg/(m^2·s) in this study.

For the dust storm event studied in this paper, the dimension of β is reduced from $O(10^4)$ originally to $O(10^3)$ through the three filters. The reduced SVMF coverage is shown in Fig.3.2(a), in contrast, the original SVMF map covers the whole model domain.

3.3.3. REDUCED-TANGENT-LINEARIZATION 4DVAR

The aim of the 4DVar is to seek the maximum likelihood estimation of the SVMF $\boldsymbol{\beta}$, conditioned on the available observations over an assimilation window. In a full nonlinear 4DVar system, this problem can be solved by minimizing a cost function:

$$\mathcal{J}(\boldsymbol{\beta}) = \frac{1}{2}(\boldsymbol{\beta}-\boldsymbol{\beta}_b)^T\mathbf{B}^{-1}(\boldsymbol{\beta}-\boldsymbol{\beta}_b) + \frac{1}{2}\sum_{i=1}^{k}\{\boldsymbol{y}_i - \mathcal{H}_i(\boldsymbol{x}_i)\}^T\mathbf{O}_i^{-1}\{\boldsymbol{y}_i - \mathcal{H}_i(\boldsymbol{x}_i)\} \tag{3.7}$$

where the subscript i represents time $t_i \in [t_1, t_k]$. The term $\boldsymbol{x}_i \in \mathbf{R}^n$ denotes the state vector, which contains the dust concentrations defined in a 3D array of grid cells. $\boldsymbol{y}_i \in \mathbf{R}^m$ is the observation vector representing the field observations. $\mathbf{O}_i \in \mathbf{R}^{m\times m}$ is the observation error covariance. Observation operator $\mathcal{H}_i \in \mathbf{R}^{n\times m}$ transforms the state space into observation space.

In realistic models, the 4DVar approach is usually implemented in an incremental formulation. In the incremental 4DVar approach, the model is first linearized around the optimal guess. Then constrained on those linearizations the cost function can be minimized, this minimization process is called inner loop. However, the solution will only be suboptimal for the full space, thus the procedure needs to be repeated where the suboptimal is set as the new optimal guess, and this process is defined as the outer loop. The cost function in the incremental 4DVar formulation is described as:

$$\begin{aligned}\mathcal{J}(\delta\boldsymbol{\beta}) =& \frac{1}{2}\{\delta\boldsymbol{\beta} + (\boldsymbol{\beta} - \boldsymbol{\beta}_b)\}^T \mathbf{B}^{-1}\{\delta\boldsymbol{\beta} + (\boldsymbol{\beta} - \boldsymbol{\beta}_b)\} \\ &+ \frac{1}{2}\sum_{i=1}^{k}\{\mathbf{H}_i\mathbf{M}_i\delta\boldsymbol{\beta} + \boldsymbol{d}_i\}^T \mathbf{O}_i^{-1}\{\mathbf{H}_i\mathbf{M}_i\delta\boldsymbol{\beta} + \boldsymbol{d}_i\}\end{aligned} \tag{3.8}$$

$$\boldsymbol{d}_i \;=\; \mathcal{H}_i\mathcal{M}_i(\boldsymbol{\beta}) - \boldsymbol{y}_i \tag{3.9}$$

where $\mathcal{M}_i \in \mathbf{R}^{n\times P}$ is the LOTOS-EUROS/dust model. The variables $\delta\boldsymbol{\beta} \in \mathbf{R}^P$ denotes a perturbation around the optimal guess $\boldsymbol{\beta}$, while the operator $\mathbf{H}_i \in \mathbf{R}^{m\times n}$ and $\mathbf{M}_i \in \mathbf{R}^{n\times P}$ are the linearizations of $\mathcal{H}_i$ and $\mathcal{M}_i$ around the optimal guess $\boldsymbol{\beta}_b$.

An advantage of the incremental approach over the full nonlinear 4DVar is that once the model is linearized, the gradient of the model remains constant within each outer loop. Hence, it does not need to be recalculated at every inner loop, unlike the classical approach. However, to build and maintain linearized models $\mathbf{M}$ always costs a huge effort.

In practice, a further simplification can be made based on the incremental 4DVar without implementing the full dimension model linearization $\mathbf{M}$. We adopt a RTL 4DVar with much less computation cost. As the βs are assumed to be spatially correlated in Eq.3.2, the further reduction can be conducted by projecting the model onto a set of dominant patterns. These patterns are derived by a Proper Orthogonal Decomposition (POD) of the error covariance $\mathbf{B}$ as follows:

$$\begin{aligned}\mathbf{B} = \mathbf{U}\mathbf{U}^T &\approx \tilde{\mathbf{U}}\tilde{\mathbf{U}}^T \\ \delta\boldsymbol{\beta} &\approx \tilde{\mathbf{U}}\delta\boldsymbol{w} \\ \boldsymbol{\beta} - \boldsymbol{\beta}_b &\approx \tilde{\mathbf{U}}\boldsymbol{w}\end{aligned} \tag{3.10}$$

where $\mathbf{U} \in \mathbf{R}^{P\times P}$ is the background covariance transform, while $\tilde{\mathbf{U}} \in \mathbf{R}^{P\times p}$ is the truncation of $\mathbf{U}$ based on POD. The vectors $\boldsymbol{w}$ and $\delta\boldsymbol{w} \in \mathbf{R}^p$ are the transform control variable vectors, where p denotes the rank of the reduced background covariance, which is in the order of $O(10^2)$. Thus, the simplified incremental 4DVar is defined with the inner minimization performed in a lower subspace. The minimization processes are performed with the following steps:

(1) Set the first guess $\boldsymbol{w} = [0, 0, ..., 0]$, $\boldsymbol{\beta} = \boldsymbol{\beta}_b$

(2) Do the outer loop iterations of minimization for $l = 1, 2, ...$

(i) Derive the rank reduced tangent linear model $\mathbf{H}_i\tilde{\mathbf{M}}_i\tilde{\mathbf{U}}$ by integrating the nonlinear model $\mathcal{H}_i\mathcal{M}_i$ from the initial $\boldsymbol{\beta}$, as well as the innovations $\boldsymbol{d}_i$ by Eq.5.3

(ii) Minimize the cost function $\mathcal{J}^l$ (inner loop minimization)

$$\mathcal{J}^l(\delta\boldsymbol{w}) = \frac{1}{2}(\delta\boldsymbol{w} + \boldsymbol{w})^T(\delta\boldsymbol{w} + \boldsymbol{w}) + \frac{1}{2}\sum_{i=1}^{k}\{\mathbf{H}_i\tilde{\mathbf{M}}_i\tilde{\mathbf{U}}\delta\boldsymbol{w} + \boldsymbol{d}_i\}^T O^{-1}\{\mathbf{H}_i\tilde{\mathbf{M}}_i\tilde{\mathbf{U}}\delta\boldsymbol{w} + \boldsymbol{d}_i\} \tag{3.11}$$

(iii) Update $\boldsymbol{w} = \boldsymbol{w} + \delta\boldsymbol{w}$, and $\boldsymbol{\beta} = \boldsymbol{\beta}_b + \tilde{\mathbf{U}}\boldsymbol{w}$

(3) Set the final analysis $\boldsymbol{\beta}^a = \boldsymbol{\beta}$.

The RTL 4DVar is based on POD of $\mathbf{B}$, which efficiently carries out model reduction by identifying the few most energetic modes. It not only reduces the computation time to derive the model linearization $\tilde{\mathbf{M}}$, but also speeds up the inner loop minimization. However, as it only explores the optimal parameters in a reduced subspace, inevitably some properties of the original system will be lost. Generally, the higher the ratio p/P, the less computation saving could be achieved, but more model dynamics will be retained.

3.4. DUST STORM OBSERVATIONS FROM CHINA MEP NETWORK

From April 14 to April 17 in 2015, more than 400 sites in the North China observed severe PM_{10} concentration caused by a SDS from Gobi desert, providing a good opportunity to study the dust storm simulation. Among the several hundred stations in the dust-affected areas, 94 sites are selected, from which the hourly PM_{10} concentration will be assimilated in the following twin experiments. For a given site where several stations overlap, the average measurements of these observations will be used. These observation sites are shown in Fig.3.2(b).

However, as the daily air pollution has been a severe problem in China. Airborne pollutants from agriculture, fossil fuel burning for electricity, in particular coal for electricity and oil for transportation severely effect the air quality. Thus, even during the SDS, in which the dust particles are the dominant aerosols, the PM_{10} measurements from the field stations cannot exactly reflect the dust aerosol concentration, but also include background coarse-mode aerosols from local airborne emissions. The time series of PM_{10} and $PM_{2.5}$ in the field stations of Hohhot (40.5°N, 111.5°E) and Beijing (40°N, 116.5°E) are shown in Fig.3.3. These two cities are chosen to demonstrate the existence of the observation bias that is found in all other cities. Before the SDS is observed ($t < 08:00$ (CST), April 15), PM_{10} around 100 and 200 $\mu g/m^3$, $PM_{2.5}$ around 50 and 60 $\mu g/m^3$ are already observed in Hohhot and Beijing, respectively. Then at 13:00 and 18:00, there is a sharp increase of the PM_{10} observations in Hohhot and Beijing, which is believed to be caused by SDS. Besides, the $PM_{2.5}$ level is quite stable, not affected by the

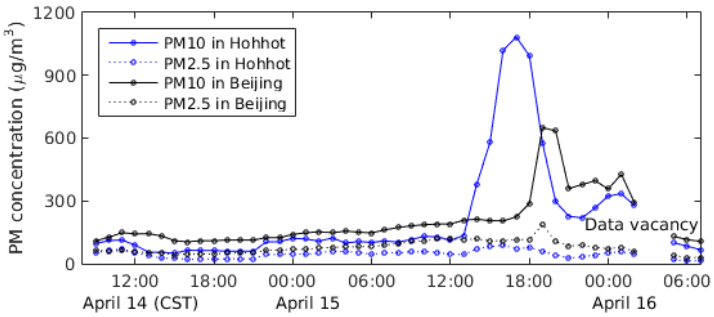

Figure 3.3: Time series of PM_{10}, $PM_{2.5}$ measurements in Hohhot and Beijing

dust storm. It validates that the dust aerosols with a diameter less than 2.5 μm take up a small fraction as we mentioned in Chapter 3.2.

Xu et al. (2017) demonstrated that the common aerosol sources (anthropogenic emission) result in a strong positive correlation between the PM_{10} and $PM_{2.5}$, and Zhou et al. (2016) mentioned when the $PM_{2.5}$ is scarce, the ratio (the slope of the linear regression of $PM_{2.5}$ versus PM_{10}) and the available PM_{10} could help to evaluate the $PM_{2.5}$ situation. For observation sites like Beijing and Hohhot, the correlation coefficient R between these two PMs are quite high (0.84 and 0.92) before the dust storm (08:00, April 14 to 08:00 April 15). Therefore, it is also possible to evaluate the non-dust PM_{10} by the $PM_{2.5}$ during the following dust storm event, as follows:

$$PM_{10}^{\text{non-dust}} = r \times PM_{2.5} + b \qquad r > 1 \tag{3.12}$$

where r and b are the linear regression parameters based on the non-dust period (08:00, April 14 to 08:00 April 15) PM data in a given site.

In the following twin experiments, the anthropogenic airborne aerosols are excluded, and the PM_{10} observations are assumed to only reflect the dust concentration. In the real data experiments, an observation bias correction (OBC) algorithm is applied, in which the correlation $R(PM_{10}, PM_{2.5})$ during the non-dust period is first calculated. Only the cities whose PM_{10} and $PM_{2.5}$ are closely related, i.e, $R > R_{\text{thre}}$, the observations will be assimilated, and the observation bias y_{bias} and dust concentration y are considered as:

$$y_{\text{bias}} = PM_{10}^{\text{non-dust}} \tag{3.13}$$

$$y = PM_{10} - y_{\text{bias}} \tag{3.14}$$

3.5. TWIN EXPERIMENT RESULTS AND DISCUSSION

3.5.1. EXPERIMENT SETUP

Twin experiments are conducted to evaluate the impact of reduced covariance rank size p and the three SVMF filters on parameter estimation. The improvements on dust flux and dust concentration simulation using the estimated SVMF are assessed.

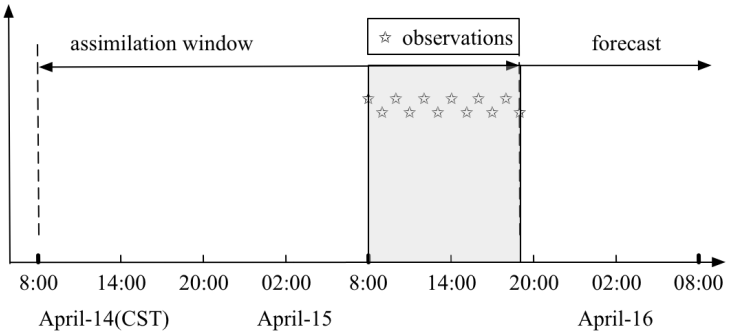

Figure 3.4: Illustration of the assimilation window of 36 hours, measurements in the gray period are assimilated

According to our prior simulations, the dust emission started at April 14 in the Mongolia and Gobi Desert, and lasted for several hours. Subsequently, the plume is blown to the downwind areas. However, it is not observed until 08:00, April 15, by the field stations due to the long distance transport. Therefore, the first assimilation window is designed from 08:00(CST), April 14 to 19:00(CST), April 15 (36 hours), but only the field observations within the last 12 hours are assimilated as shown in Fig.3.4. As the dust emission is negligible after the first cycle, a second one is not performed.

The period after 19:00, April 15 is defined as the forecast stage, in which the data is not assimilated and used as the independent observation for cross-validation. With the posterior $\boldsymbol{\beta}_a$ map from the assimilation cycle, the dust model is propagated forward from the 08:00, April 14 again, and stopped at 07:00, April 16. Then, the model output is compared with the truth both in the assimilation window and forecast stage.

3.5.2. SVMF TRUTH AND OBSERVATION OPERATOR

In the twin experiments, the $\boldsymbol{\beta}_{\text{truth}}$ is randomly sampled from $N(\boldsymbol{\beta}_b, \mathbf{B})$, as shown in Fig.3.5. The βs in the eastern areas are assumed to be overestimated, while the ones in the western region are underestimated.

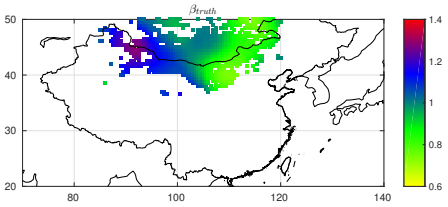

Figure 3.5: The $\boldsymbol{\beta}_{\text{truth}}$ map

An observation operator $\mathcal{H}$ is defined to map the model state $\boldsymbol{X}$ to observation space $\boldsymbol{y}$:

$$\boldsymbol{y}_i = \mathcal{H}_i(\boldsymbol{X}_i) + \boldsymbol{v}_i, \qquad \boldsymbol{v}_i \sim \mathcal{N}(0, \mathbf{R}_i) \tag{3.15}$$

Case	RTL 4DVar	p	SVMF filters
A(no DA)	×	-	-
B	√	8	√
C	√	16	√
D	√	16	×

NOTE: √ applied; × not applied.

Table 3.1: Configurations of 4 cases in twin experiments

where $\boldsymbol{v}$ denotes the observation representation error which is drawn from a Gaussian distribution with a mean 0 and a covariance matrix $\mathbf{R}$. The observations are assumed to be independent, thus $\mathbf{R}$ is a diagonal matrix. The observation error is assumed to be proportional to the measurement with a error percentage $e = 10\%$, a similar PM_{10} error setting was used in Lin et al. (2008).

3.5.3. PARAMETER ESTIMATION

The RTL 4DVar aims to minimize the cost function in the subspace $\boldsymbol{\beta} = \boldsymbol{\beta}_b + \tilde{\mathbf{U}}\boldsymbol{w}$, where $\tilde{\mathbf{U}} \in \mathbf{R}^{P\times p}$. In this study, the algorithm with 4 different configurations is implemented, as shown in Table 3.1. In case A (deterministic model, no data assimilation), the prior $\boldsymbol{\beta}_b$ is set as spatially constant $[1, 1, ..., 1]$ as shown in Fig.3.6(a). Reduced covariance rank $p = 8$ and $p = 16$ are used in case B and C, respectively, and the result is also compared with case D, in which $p = 16$ is used and the SVMF filters are excluded.

Fig.3.6(c) and (e) are the $\boldsymbol{\beta}_a$ obtained in case B and C, the RTL 4DVar together with SVMF filters return a $\boldsymbol{\beta}_a$ map which is a good match with the $\boldsymbol{\beta}_{\text{truth}}$. Fig.3.6(b),(d) and (f) present the parameter estimation error in case A,B,C. The data assimilation algorithm has an obvious effect on the parameter estimation, a larger p usually gives a more accurate result. Compared to the deterministic model simulation, case B and C using $p = 8$ and $p = 16$ result in a 41% and 53% improvement on parameter estimation. However, parameter estimation in the boundary region of source areas is always poor no matter $p = 8$ or $p = 16$. This is caused by the low sensitivity of the parameters in these regions to the field observations, and details will be further explained in Chapter 3.5.4.

Moreover, to investigate whether the three SVMF filters help to improve the computation efficiency of the RTL 4DVar, a comparison experiment is designed. In this test, the POD model reduction is implemented in the original space without using the filters, thus P is in the order of $O(10^4)$. With the same assimilation window and observation error setting, the optimal solution $\boldsymbol{\beta}_a$ is computed with $p = 16$. The posterior $\boldsymbol{\beta}_a$ and the parameter estimation error $\boldsymbol{\beta}_a - \boldsymbol{\beta}_{\text{truth}}$ map are shown in Fig.3.6(g) and (h). Even when the same reduced covariance rank $p = 16$ is used in case D, the estimated parameters are far worse than the $\boldsymbol{\beta}_a$ in case C, they are even worse than the $\boldsymbol{\beta}_a$ in case B with $p = 8$ and the SVMF filters. By using a much larger p in case D, a similar or even better performance than case B and C are expected. However, it also requires far more computation cost. Thus the SVMF filters help to achieve a higher accuracy with the limited reduced covariance rank size p.

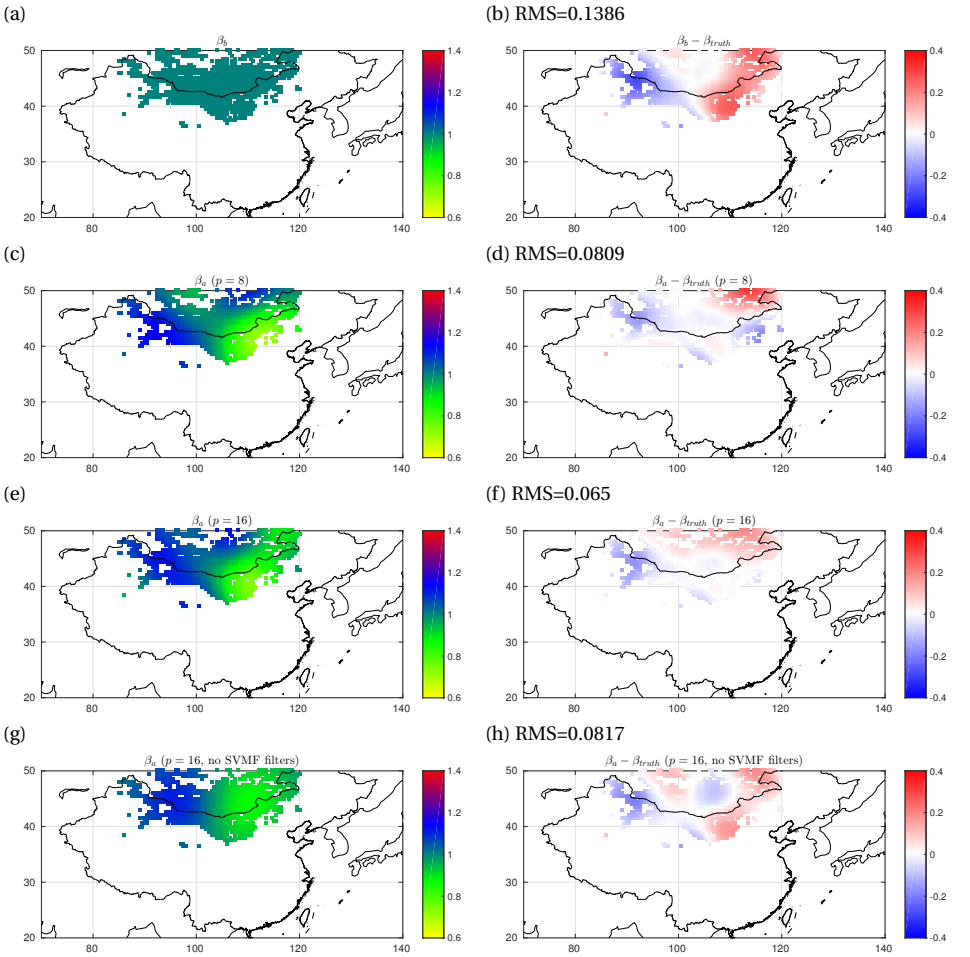

Figure 3.6: The prior, posterior parameter fields and the corresponding error maps: (a) and (b): $\boldsymbol{\beta_b}$ and $\boldsymbol{\beta}_b - \boldsymbol{\beta}_{\text{truth}}$; (c) and (d): $\boldsymbol{\beta_a}$ and $\boldsymbol{\beta}_a - \boldsymbol{\beta}_{\text{truth}}$ with $p = 8$; (e) and (f): $\boldsymbol{\beta_a}$ and $\boldsymbol{\beta}_a - \boldsymbol{\beta}_{\text{truth}}$ with $p = 16$; (g) and (h): $\boldsymbol{\beta_a}$ and $\boldsymbol{\beta}_a - \boldsymbol{\beta}_{\text{truth}}$ with $p = 16$ and not using SVMF filters

.

3.5.4. DUST FLUX ESTIMATION

In Chapter 3.5.3, the $\boldsymbol{\beta}_a$ has large errors in the boundary region of the potential source area in all the three assimilation-involved cases.

The aim of applying the SVMF to the FVT is to correct the errors in the dust emission parameterization, which will improve the corresponding dust emission simulation. However, the emission flux rate is a time-varying quantity and it is difficult to visualize the time series of flux map. Therefore, a dust emission integration F (g/m^2), from 08:00 (CST), April 14 and 7:00 (CST), April 16. is introduced to evaluate the dust emission.

Fig.3.7(a) shows the $F(\boldsymbol{\beta}_{\text{truth}})$ while Fig.3.7(b), (d), (f) and (h) represent the dust emission integration in cases A to D. In the $F(\boldsymbol{\beta}_{\text{truth}})$ map, it is observed that most dust aerosols are emitted from the eastern part of the source region, and the dust emission is very weak in the western areas. Similar to the $F(\boldsymbol{\beta}_{\text{truth}})$, the dust flux estimation on the western region can also be neglected for all the three $F(\boldsymbol{\beta}_a)$, and the difference to the $F(\boldsymbol{\beta}_{\text{truth}})$ in these areas is very small as shown in Fig.3.7(e), (g) and (i). Even though $\boldsymbol{\beta}_a$ has a large error in the western source region, we can still obtain a $F(\boldsymbol{\beta}_a)$ map that is quite close to the $F(\boldsymbol{\beta}_{\text{truth}})$ by using the data assimilation. Besides, the dust emission flux in the upper right corner is not well reproduced for all the three assimilation-involved cases. It is because the dust particles there are deposited completely before measured by the field observation network which is quite far away. Therefore, the poor $\boldsymbol{\beta}$ estimation in the boundary dust source regions is due to the low sensitivity to field observations.

In the background emission integration map $F(\boldsymbol{\beta}_b)$, the emission is concentrated in the middle source areas, resulting in a big discrepancy from the $F(\boldsymbol{\beta}_{\text{truth}})$. The error in the emission process is alleviated using the 4DVar, most dust emission is concentrated on the eastern areas for all the three $F(\boldsymbol{\beta}_a)$. It shows our system is not only capable in adjusting the emission rate in a given cell, but also in identifying the correct source regions.

Fig.3.7(c), (e), (g), and (i) represent the difference between the $F(\boldsymbol{\beta}_{\text{truth}})$ and dust emission integration F in cases A-D, with an RMSE of 5.4, 2.8, 1.2 and 4.5 g/m^2, respectively. Statistically, the RTL 4DVar in cases B,C and D result in a 48%, 78% and 17% improvement on dust emission estimation. Therefore, the SVMF filters helps to give a more accurate dust flux estimation using the same reduced covariance rank size p.

3.5.5. MODEL STATE ESTIMATION

With the estimated parameters $\boldsymbol{\beta}_a$, the model states $\boldsymbol{X}_a = \mathcal{M}(\boldsymbol{\beta}_a)$ both in the assimilation window $t \leqslant$ 19:00(CST), 15 April and in forecast stage $t >$ 19:00(CST), 15 April are also evaluated.

Fig.3.8(a) and (b) show the surface dust concentration (SDC) $\boldsymbol{X}_{\text{true}} = \mathcal{M}(\boldsymbol{\beta}_{\text{true}})$ at time snapshots of 19:00(CST) and 22:00(CST), respectively, while the corresponding SDC at these two moments in cases A to D are presented in Fig.3.8(c)-(j). It is found that the main part of dust plume $\boldsymbol{X}_{\text{true}}$ at 19:00 (CST) stayed in Central China and Inner Mongolia, where the severe SDC is as high as 1000 μg/m^3. Then it was moved southward, and the maximum SDC is in the range of 400 to 800 μg/m^3 at 22:00. Different from $\boldsymbol{X}_{\text{truth}}$, most values of $\boldsymbol{X}_b$ are rather low, and the main dust is concentrated in the front of the plume. Besides, a dust plume is also observed in the western region in the $\boldsymbol{X}_b$. Generally, the SDC simulation with the estimated $\boldsymbol{\beta}_a$ is greatly improved compared to the prior

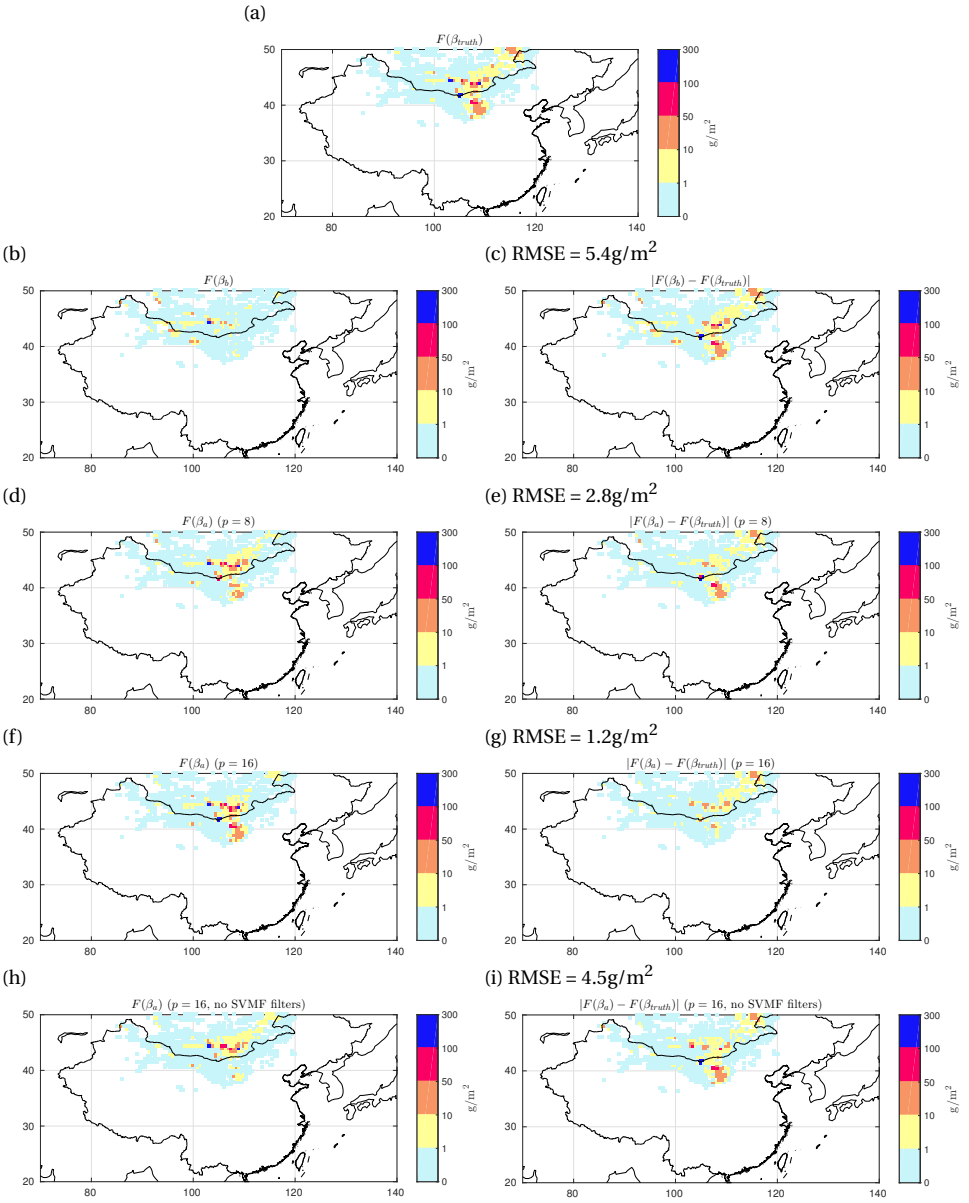

Figure 3.7: The truth, prior and posterior dust emission integration and the absolute error map: (a): $F(\boldsymbol{\beta}_{\text{truth}})$; (b) and (c): $F(\boldsymbol{\beta}_b)$, $|F(\boldsymbol{\beta}_b) - F(\boldsymbol{\beta}_{\text{truth}})|$; (e) and (f): $F(\boldsymbol{\beta}_a)$, $|F(\boldsymbol{\beta}_a) - F(\boldsymbol{\beta}_{\text{truth}})|$ with $p = 8$; (g) and (h): $F(\boldsymbol{\beta}_a)$, $|F(\boldsymbol{\beta}_a) - F(\boldsymbol{\beta}_{\text{truth}})|$ with $p = 16$; (i) and (j): $F(\boldsymbol{\beta}_a)$, $|F(\boldsymbol{\beta}_a) - F(\boldsymbol{\beta}_{\text{truth}})|$ with $p = 16$ and without using the SVMF filters

states $\boldsymbol{X}_b$. The severe dust affected areas are perfectly reproduced in $\boldsymbol{X}_a$ with $p = 16$, and the dust plume in western regions is also very weak. Meanwhile, the estimated SDC simulation using $p = 16$ performs better than simulation configured with $p = 8$ and $p = 16$ but without using the three SVMF filters.

Fig.3.9 (a) and (b) depict the SDC time series from 8:00(CST), 14 April to 07:00(CST), 16 April in the field station Hohhot and Beijing. In Hohhot, it is found that the background dust concentration reached a peak around 350 μg/m^3 at 11:00(CST), April 15, while the truth dust concentration peaked around 700 μg/m^3 at 18:00(CST). The estimated dust concentration variations in the three assimilation-involved cases are all very close to the truth, the peak is shifted later and becomes higher. For Beijing, the dust storm is not so severe, the background peak is about 200 μg/m^3 at 17:00(CST), and in the forecast stage, the SDC is almost zero. In contrast, the peak of the $\boldsymbol{X}_{\text{truth}}$ is about 100 μg/m^3 in the forecast stage. This trend is reproduced quite well by the $\boldsymbol{X}_a$ in the assimilation-involved cases.

To further assess the improvement, the root mean squared relative error (RMSrE) E is calculated,

$$E(\boldsymbol{X}) = \sqrt{\frac{1}{n}\sum_{j=1}^{n}\frac{(\boldsymbol{X}_{\text{truth}}(j) - \boldsymbol{X}(j))^2}{\boldsymbol{X}^2_{\text{truth}}(j)}} \tag{3.16}$$

where subscript j denotes a grid cell in the 3D model. E will be used to measure the difference between $\boldsymbol{X}_a$ and $\boldsymbol{X}_{\text{truth}}$.

Fig.3.10 shows the time series of RMSrE of the 3D model states in the assimilation window (08:00~19:00) and forecast stage (20:00~07:00). In all assimilation-involved (B,C and D) cases, persistent improvement on dust concentration simulation can be clearly observed. Moreover, the implementation of the SVMF filters contributes to a higher accuracy with the same reduced covariance rank p.

3.5.6. COMPUTATIONAL COMPLEXITY ANALYSIS

In this section, we will analyze the computation costs for the 4 cases. In the cost function minimization processes as described in Chapter 3.3.3, updating the rank-reduced tangent linearization $\mathbf{H}_i\tilde{\mathbf{M}}_i\tilde{\mathbf{U}}$ by forward model integration (FMI) is the most time consuming part. Each FMI takes about 40min (t_{FMI}), while the entire inner loop minimization costs less than 2min which will be neglected in the analysis below. Thus in each outer loop iteration, the computation time is approximately $p+1$ times the cost of one FMI, and the computational complexity (CC) for the whole minimization procedure can be approximated as:

$$\text{CC} = l \cdot (p+1) \cdot t_{\text{FMI}} + t_{\text{FMI}} \tag{3.17}$$

where l represents the number of outer loop iterations.

The value of cost function J vs. the number of outer loop iterations is shown in Fig.3.11, in all cases, the cost function is considered to be convergent within 5 outer loops. Table 3 lists the computational complexity in computing the prior, posteriors ($p = 8$, $p = 16$ and $p = 16$ but not using SVMF filters) in cases A-D, as well as the final

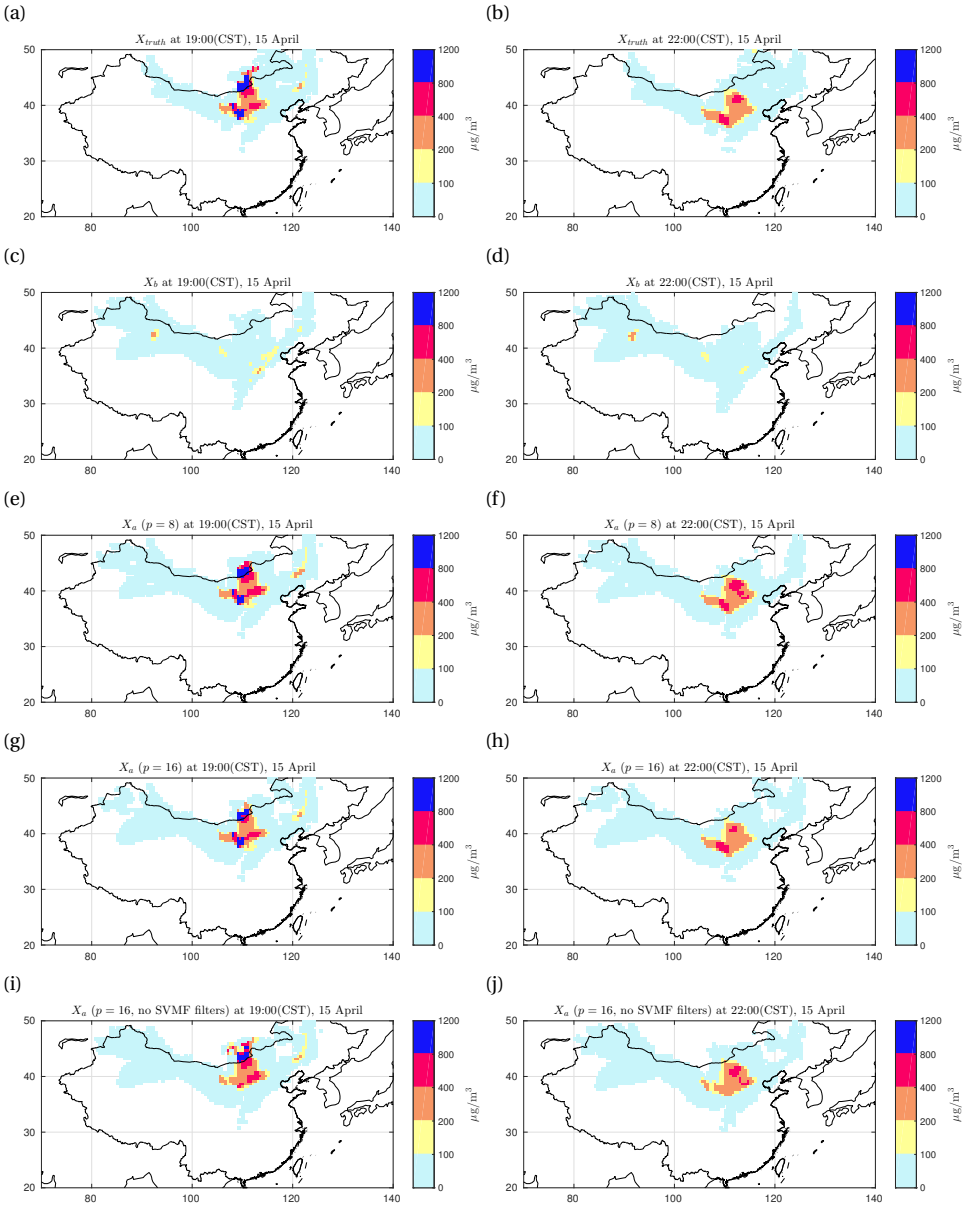

Figure 3.8: The surface dust concentration (SDC) simulation at 19:00(CST) and 22:00(CST), 15 April: (a)(b) Truth $\boldsymbol{X}_{\text{truth}}$; (c)(d) prior $\boldsymbol{X}_b$; (e)(f) posterior $\boldsymbol{X}_a$ with $p = 8$; (g)(h) posterior $\boldsymbol{X}_a$ with $p = 16$; (i)(j) posterior $\boldsymbol{X}_a$ with $p = 16$ and not using SVMF filters

(a)

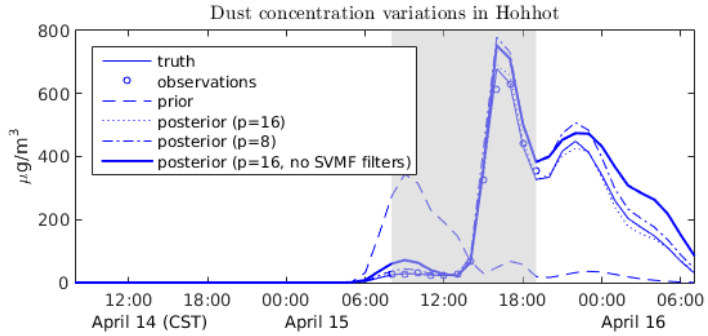

(b)

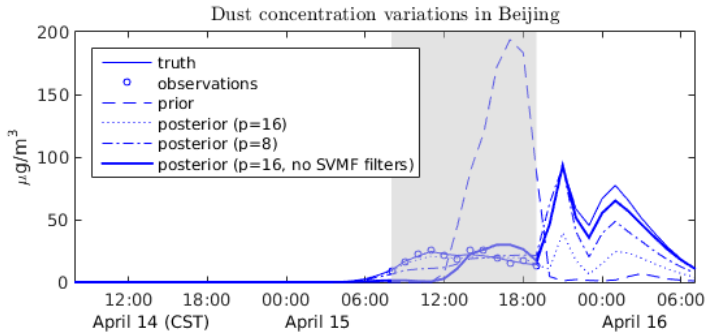

Figure 3.9: The SDC time series in the city of Beijing and Hohhot

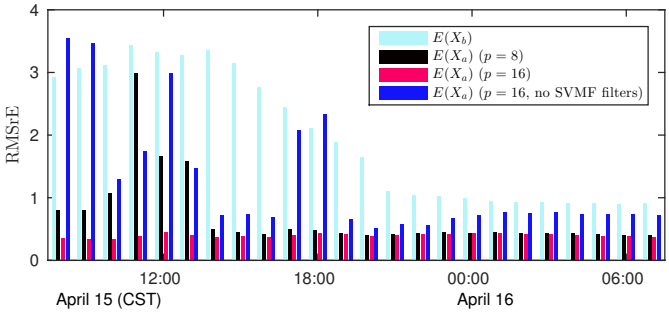

Figure 3.10: RMSrE under different reduced covariance rank p and with or without SVMF filters

Case	A	B	C	D
Configuration	prior	posterior $p = 8$	posterior $p = 16$	posterior $p = 16$ (no SVMF filters)
Outer loop(s) l	0	5	5	5
CC (t_{FMI})	1	46	86	86
$\mathcal{J} = \mathcal{J}_o + \mathcal{J}_b$	82876	2849	587	6074
RMSE of $\boldsymbol{\beta}$	0.139	0.081	0.065	0.082
RMSE of F (g/m^2)	5.4	2.8	1.2	4.5
average $E(X)$	1.96	0.70	0.40	1.25

Table 3.2: Computational complexity, final cost function, analysis error in β, F and $E(X)$

$J_o + J_b$, RMSE of $\boldsymbol{\beta}$ and F and the average $E(X)$. Obviously, the SVMF filter helps the RTL 4DVar to achieve a more accurate result with the limited computation cost.

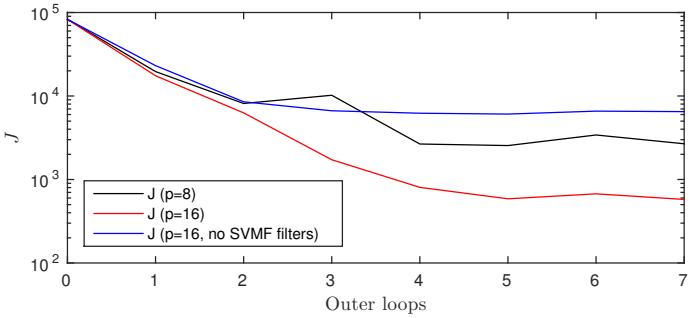

Figure 3.11: The value of the cost function vs. the number of outer loop iterations

Although the success of twin experiments is not a guarantee for the assimilation of real field observations, they do show the FVT map is able to be estimated under ideal conditions. To further explore the potential of the proposed method, we will conduct experiments with real field measurements in the following section.

3.6. EXPERIMENTS WITH REAL FIELD OBSERVATIONS

In the following, the real field measurements from China MEP are incorporated to estimate the FVT using the RTL 4DVar. These experiments are the initial tests to use the field observations in dust emission data assimilation, and they are based on the assumptions:

(1) The dust model is perfect, except the FVT;

(2) The dust can be fully represented by the 5 bins;

(3) The temporal variation of FVT within each assimilation cycle (36 hours) is negligible.

Similar to the configurations in the twin experiments, the only assimilation window is designed from 8:00(CST) to 19:00(CST), April 15. The β spatial correlation distance

threshold L and reduced covariance rank p are configured as 800 km and 16, respectively. We also tried $L = 400$ and $p = 40$, but the improvement is ignorable, thus $L = 800$ and $p = 16$ are considered to be sufficient for this case study.

3.6.1. STATISTICAL OBSERVATION BIAS CORRECTION

As mentioned in Chapter 3.4, the real PM_{10} include all aerosols with a diameter up to 10 μm, not only the dust particles. Thus the dust aerosol fraction need to be extracted from the PM_{10} measurements, this procedure is defined as observation bias correction (OBC), in which the non-dust PM_{10} is evaluated using the $PM_{2.5}$ as shown in Eq.3.13.

To make the OBC more representative, only when the PM_{10} and $PM_{2.5}$ are validated to be strongly correlated ($R > R_{\text{thre}}$) during the non-dust period (8:00, April 14 to 08:00, April 15), non-dust PM_{10} will be approximated, otherwise measurements at these sites will be discarded. In the experiments with real measurements, the correlation coefficient threshold R_{thre} are set as 0.6 and 0.8, which result 81 and 72 observation sites whose PM_{10} measurements will be processed and used in the data assimilation.

Besides, observations from Hohhot and Beijing together with Xingtai (37°N, 114.5°E) a city in the very downstream are not assimilated, but used as the independent observations for the cross-validation.

3.6.2. OBSERVATION REPRESENTING ERROR

Though the OBC is already implemented, and the preprocessed observations will be more close to the real dust concentration, it is still hard to distinguish the dust aerosols from the anthropogenic particles if the bias-corrected observation value is small. Thus, the 10% observation error setting is not suitable in the real data experiments.

A variable representation error is designed, in which a smaller representation error is assigned to measurements reporting a higher PM_{10} value. In other words, we give more confidence to high-value observations than small-value measurements to represent the dust concentration level. This observation error $v_i(j)$ in this case is drawn from a Gaussian distribution with mean 0 and a deviation σ. The σ is configured as:

$$\sigma = \begin{cases} 200 & y \leq 200 \ (\mu g/m^3) \\ -0.125 \cdot y + 225 & 200 < y < 1000 \ (\mu g/m^3) \\ 100 & y \geqslant 1000 \ (\mu g/m^3) \end{cases} \tag{3.18}$$

where y represents the PM_{10} field measurement. These observation error settings are empirically based, and should be checked before implementation in other aerosol data assimilation applications.

3.6.3. RESULTS

Firstly, the experiment was conducted using the original PM_{10} concentration combined with the variable representation error setting, but without the OBC. The posterior $\boldsymbol{\beta}_a$, as shown in Fig.3.12(a), is obtained after the first and the only assimilation cycle. Next, the experiment is performed again but using the bias-corrected observations, and the resulting posterior $\boldsymbol{\beta}_a$ map is shown in Fig.3.12(b). Compared to the prior $\boldsymbol{\beta}_b$ which is set as spatially constant $[1, ..., 1]$, the assimilation test without using OBC returns a $\boldsymbol{\beta}_a$ map

in which the $\boldsymbol{\beta}$ in the middle parts are overestimated. While in $\boldsymbol{\beta}_a$ which is calculated in the experiment using OBC, only the $\boldsymbol{\beta}$ in the very center part are overestimated.

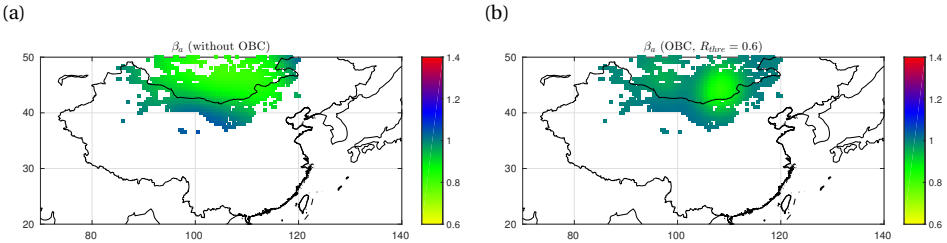

Figure 3.12: The $\boldsymbol{\beta}_a$ calculated in the assimilation experiments (a): without OBC; (b) with OBC

There is no doubt the $\boldsymbol{\beta}_a$ from the test without using OBC will result in a more severe dust storm. It is reasonable because the PM_{10} observations without OBC are believed to overestimate the surface dust concentration.

Fig.3.13 (a) and (b) show the dust emission integration F using the two $\boldsymbol{\beta}_a$ maps. In accord with the analysis above, more dust aerosols are emitted in $F(\boldsymbol{\beta}_a)$ (no OBC), while the main dust emissions concentrate on the very center part in $F(\boldsymbol{\beta}_a)$ (OBC).

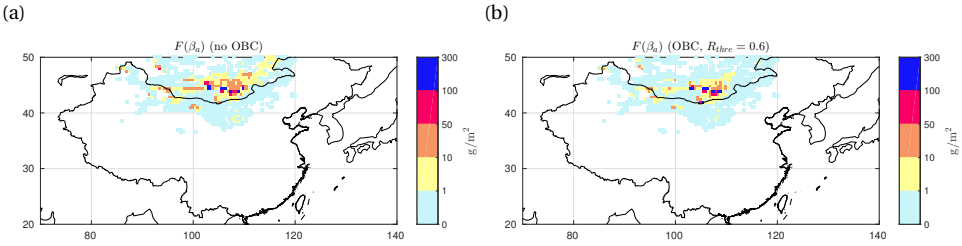

Figure 3.13: The $F(\boldsymbol{\beta}_a)$ calculated in the assimilation experiments (a): without OBC; (b): with OBC

The deterministic model simulation (no assimilation) was performed with the same settings as used in the twin experiments, and the corresponding SDC can be found in Fig.3.8(c) and (d). The background simulation is found to considerably underestimate the dust concentration.

Fig.3.14(a) and (b) show the field observations of PM_{10} at 19:00(CST) (in the assimilation window) and 22:00(CST) (in the forecast stage), April 15. At these two snapshots, the dust plume is already transported to the Central, Northeast and West China. Especially in Central China, the PM_{10} values in some cities are as high as 1000 μg/m^3. Fig.3.14(c) and (d) present the SDC estimation $\mathcal{M}(\boldsymbol{\beta}_a)$ which is calculated in no-OBC assimilation experiment. Generally, it can reproduce the dust plume well. In the Central China, the SDCs are in the range from 400 to 800 μg/m^3 similar to the real PM_{10} map. However, the dust concentration is still underestimated in the Northeast China compared to the observations.

Fig.3.14(e) and (f) show the bias-corrected SDC using OBC ($R_{\text{thre}} = 0.6$). Obviously, the 'real' dust level is not so severe compared to PM_{10} measurements in Fig.3.14(a) and (b). Besides, a weak PM_{10} $PM_{2.5}$ correlation is found at some cities in Northeast China, thus OBC is not implemented at these sites, and the observations are abandoned and not used. Fig.3.14(g) and (h) depict the estimated SDC $\mathcal{M}(\boldsymbol{\beta}_a)$ obtained by assimilating these bias-corrected measurements. Generally, the $\mathcal{M}(\boldsymbol{\beta}_a)$ matches the bias-corrected PM_{10} very well, and the dust is not so severe as the SDC in Fig.3.14(c) and (d).

To better evaluate the dust concentration estimation, the PM_{10} simulation time series, as well as the field PM_{10} observation variations at three selected cities are shown in Fig.3.15. The measurements from these cities (Hohhot, Beijing and Xingtai) are not assimilated, but treated as the independent data for the verification. They are chosen to illustrate the differences in results that were found for various sites.

The Hohhot city is located near the dust source region, thus the SDS arrives earlier than in the other two cities. As shown in Fig.3.15(a), the PM_{10} observations reaches the peak of 1100 μg/m^3 at 17:00, while the peak of the background SDC realization is around 300 μg/m^3 at 9:00, which is 8 hours earlier. In contrast, the PM_{10} simulation of all the three posteriors also reaches the top over 1000 μg/m^3 at 17:00. Over the whole assimilation window, the PM_{10} simulations are quite close to the PM_{10} measurements. In the forecast stage, both the PM_{10} measurements and simulations declined, although the observations decrease faster than the simulations. One possible reason is that there are few field stations located between the source region and Hohhot, thus little information related to the dust concentration in Hohhot in the forecast stage can be obtained in the assimilation window. Besides, an underestimation of the dust removal precesses (dry and wet deposition) could also lead to this error. On the other hand, as the y_{bias} is at a quite low level compared to the dust concentration in Hohhot, the improvement by using OBC is not significant.

Within the grid cell Beijing (116.25~116.75°N, 39.75~40.25°N), there are 15 field stations, but only the average of these measurements is used, and the observation distribution is not yet incorporated into the observation error configuration. In Fig.3.15(b), SDC simulation and the mean of 15 observations, together with the maximum and minimum measurements are presented. Generally, the estimated PM_{10} using OBC has a better performance than the background model realization and the one without using OBC, but it is still underestimated compared to the mean observations. In addition to the mean of observations, the distribution is considered to be used in our future work.

Our OBC is found to work very well in cities like Xingtai. Even though the PM_{10} level varied a lot during the non-dust period (08:00, April 14 to 08:00, April 15), the results of the non-dust PM_{10} simulation by $PM_{2.5}$ data match the trend very well. As Xingtai is located in the very downwind regions, the dust storm arrived there later than in Hohhot and Beijing as shown in Fig.3.15(c). Besides, because the dust transport is flow-dependent, more information related to the future dust concentration in Xingtai are supposed to be obtained in the first assimilation window. Therefore, we expect to obtain a good performance in the SDC simulation in forecast stage. In fact, the estimated PM_{10} simulation using OBC is very close to our expectation. Both the simulated PM_{10} and the real observations stayed around 250 μg/m^3 from 19:00 to 22:00, April 15, then sharply climbed to a top of 650 μg/m^3 at 0:00, April 16. In contrast, the prior PM_{10} simulation

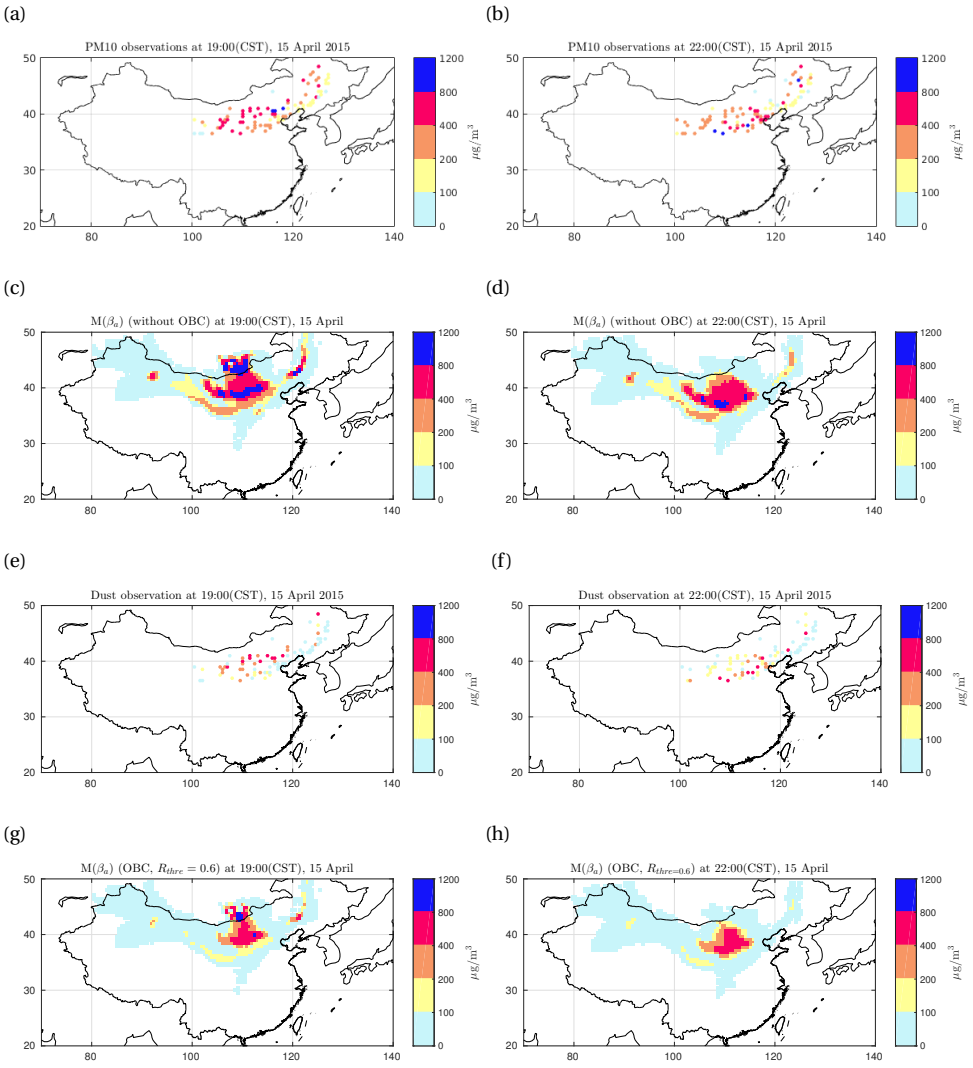

Figure 3.14: Surface dust concentration (SDC) simulations and field observations at 19:00(CST) and 22:00(CST), 15 April: (a) and (b): PM_{10}; (c) and (d): SDC by DA without OBC; (e) and (f): bias-corrected dust concentration measurement $PM_{10} - y_{bias}$; (g) and (h): SDC by DA with OBC

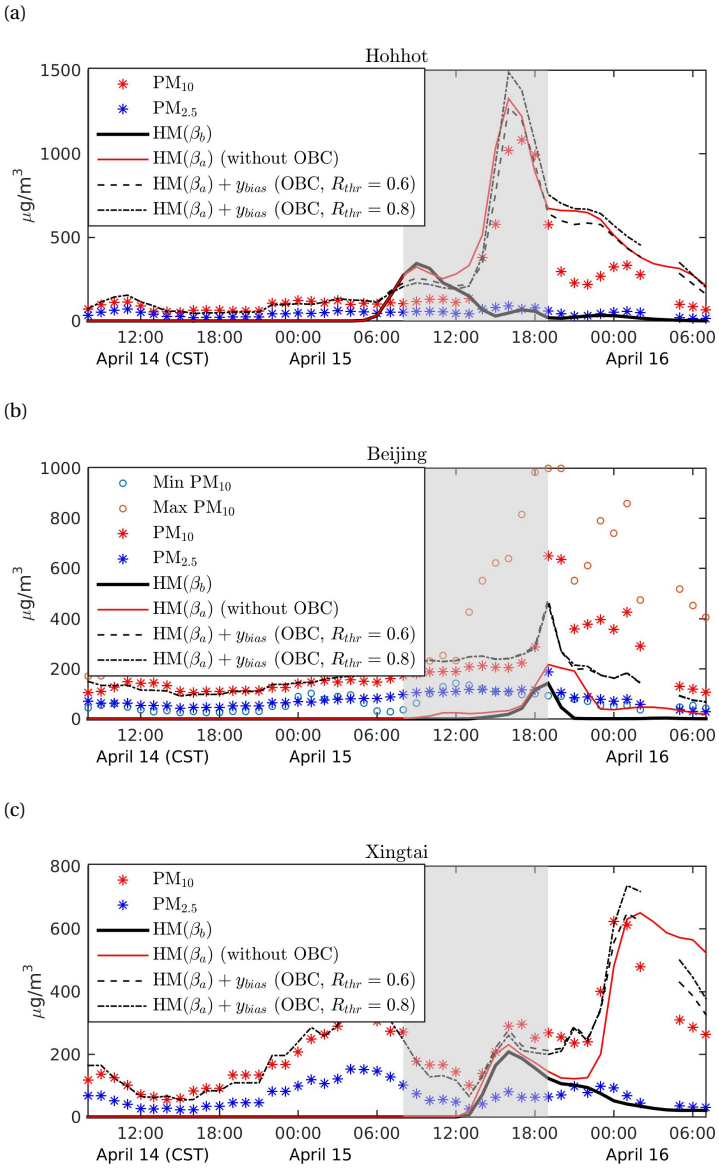

Figure 3.15: SDC simulation and PM_{10} variations in the city of (a): Hohhot, (b):Beijing, and (c): Xingtai

still seems to be earlier than the real observations. The posterior calculated in the assimilation test without OBC also matches the PM_{10} observation generally, but the difference is not negligible.

RMSE is also used to measure the difference between the PM_{10} simulation and the real measurements. Fig.3.16 shows the RMSE variation in the assimilation window (08:00~19:00) and forecast state (20:00~07:00). The average RMSE of HX_b in these two stages are about 267 and 284 $\mu g/m^3$. They are reduced to 223 and 253 $\mu g/m^3$ in the assimilation test, and further lowered to 125 and 183 $\mu g/m^3$ when the OBC is performed. The RMSE variations strongly shows the RTL 4DVar with the field observations can help to improve the dust storm forecast, and OBC is beneficial for achieving a more accurate result.

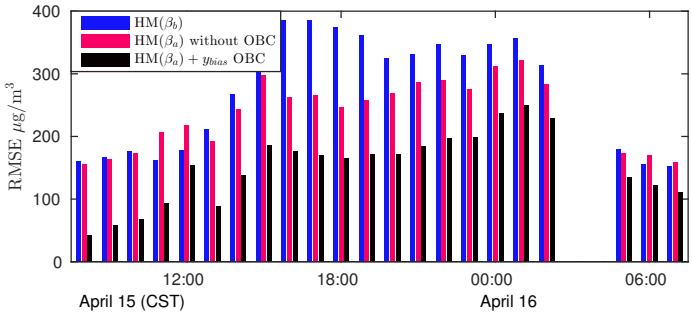

Figure 3.16: RMSE variation

3.7. CONCLUSIONS

A dust storm emission inversion system, which includes a regional dust transport model LOTOS-EUROS/dust and a reduced-tangent-linearization 4DVar, has been developed. One main feature in this study is that a spatially varying multiplicative factor (SVMF) β is applied to the friction velocity threshold (FVT), which aims to correct the mismatch in the FVT parameterization. An attractive advantage of the assimilation algorithm is that the adjoint model is not required, and replaced with the rank reduced tangent linear (TL) model. The TL is approximated by the perturbation method, the cost of which is proportional to the parameter dimension. Two model reduction techniques are designed to achieve a high computational efficiency. The first one includes the three spatially varying multiplicative factor (SVMF) filters which reduces the parameter dimension size from $O(10^4)$ to $O(10^3)$, the second one applies the proper orthogonal decomposition (POD) to further project the subspace into a set of key patterns $O(10^2)$.

Twin experiments have been performed to test the capacities of the assimilation algorithm. It is evaluated to be able to correct the spatial mismatch in the FVT parameterization using the field observations. Differences still exist between the parameter estimation $\boldsymbol{\beta}_a$ and $\boldsymbol{\beta}_{\text{truth}}$ in some boundary areas, which are caused by the low observability of these parameters by the ground observing system. The use of SVMF filters improve the convergence of the cost function with the limited computational cost.

Hourly field PM_{10} measurements from China MEP field network, provides a sam-

pling of the dust concentration with a high temporal resolution and a large spatial coverage. It is the first time these new data are used in dust storm data assimilation. A simple observation bias correction and a variable representation error are designed to alleviate the impact of the observation bias. In comparison with the independent data, our dust forecast system is able to capture the main characteristics of the dust plume. The OBC is an essential process for the forecast where the dust concentration is not very dominant in the PM_{10} measurement. Compared to the deterministic model simulation, the average RMSE has been reduced from 267 to 223 $\mu g/m^3$ in the assimilation window, 284 to 253 $\mu g/m^3$ in the forecast stage in the assimilation experiment. When the OBC is performed, the errors at the two stages are further reduced to 125 and 183 $\mu g/m^3$.

REFERENCES

Cao, Y., Zhu, J., Navon, I. M., and Luo, Z. (2007). A reduced-order approach to four-dimensional variational data assimilation using proper orthogonal decomposition. *Int. J. Numer. Meth. Fluids*, 53(10):1571–1583.

Daescu, D. N. and Navon, I. M. (2008). A Dual-Weighted Approach to Order Reduction in 4DVAR Data Assimilation. *Mon. Wea. Rev.*, 136(3):1026–1041.

Di Tomaso, E., Nick, Jorba, O., and Garcia-Pando, C. P. (2017). Assimilation of MODIS Dark Target and Deep Blue observations in the dust aerosol component of NMMB-MONARCH version 1.0. *Geoscientific Model Development*, 10:1107–1129.

Jin, J., Lin, H. X., Heemink, A., and Segers, A. (2018). Spatially varying parameter estimation for dust emissions using reduced-tangent-linearization 4DVar. *Atmospheric Environment*, 187:358–373.

Lawless, A. S., Nichols, N. K., Boess, C., and Bunse-Gerstner, A. (2008). Using Model Reduction Methods within Incremental Four-Dimensional Variational Data Assimilation. *Mon. Wea. Rev.*, 136(4):1511–1522.

Lin, C., Wang, Z., and Zhu, J. (2008). An Ensemble Kalman Filter for severe dust storm data assimilation over China. *Atmospheric Chemistry & Physics*, 8:2975–2983.

Manders, A. M. M., Builtjes, P. J. H., Curier, L., Denier van der Gon, H. A. C., Hendriks, C., Jonkers, S., Kranenburg, R., Kuenen, J., Segers, A. J., Timmermans, R. M. A., Visschedijk, A., Wichink Kruit, R. J., Van Pul, W. A. J., Sauter, F. J., van der Swaluw, E., Swart, D. P. J., Douros, J., Eskes, H., van Meijgaard, E., van Ulft, B., van Velthoven, P., Banzhaf, S., Mues, A., Stern, R., Fu, G., Lu, S., Heemink, A., van Velzen, N., and Schaap, M. (2017). Curriculum vitae of the LOTOS-EUROS (v2.0) chemistry transport model. *Geoscientific Model Development*, 10(11):4145–4173.

Vermeulen, P. T. M. and Heemink, A. W. (2006). Model-Reduced Variational Data Assimilation. *Monthly Weather Review*, pages 2888–2899.

Vermeulen, P. T. M., Heemink, A. W., and Valstar, J. R. (2005). Inverse modeling of groundwater flow using model reduction. *Water Resour. Res.*, 41(6):W06003+.

Xu, L., Batterman, S., Chen, F., Li, J., Zhong, X., Feng, Y., Rao, Q., and Chen, F. (2017). Spatiotemporal characteristics of pm2.5 and pm10 at urban and corresponding background sites in 23 cities in china. *Science of The Total Environment*, 599-600:2074 – 2084.

Zhou, X., Cao, Z., Ma, Y., Wang, L., Wu, R., and Wang, W. (2016). Concentrations, correlations and chemical species of pm2. 5/pm10 based on published data in china: potential implications for the revised particulate standard. *Chemosphere*, 144:518–526.

4

MACHINE LEARNING BASED OBSERVATION BIAS CORRECTION

Data assimilation algorithms rely on a basic assumption of an unbiased observation error. However, the presence of inconsistent measurements with nontrivial biases or inseparable baselines is unavoidable in practice. Assimilation analysis might diverge from reality, since the data assimilation itself cannot distinguish whether the differences between model simulations and observations are due to the biased observations or model deficiencies. Unfortunately, modeling of observation biases or baselines which show strong spatiotemporal variability is a challenging task. In this Chapter, we report how data-driven machine learning can be used to perform observation bias correction for the dust emission inversion using PM_{10} observations.

PM_{10} observations are considered as unbiased, however, a bias correction is necessary if they are used as a proxy for dust during dust storms since they actually represent a sum of dust particles and non-dust *aerosols. Two observation bias correction methods have been designed in order to use PM_{10} measurements as proxy for the dust storm loads under severe dust conditions. The first one is to use the conventional chemical transport (CTM) model to simulate life cycles of* non-dust *aerosols. The other one is to use the machine learning model to learn the relations between the regular PM_{10} and other air quality measurement. The latter is trained using two years of historical samples. The machine learning based* non-dust *model is shown to be in better agreements with observations compared to the CTM. The dust emission inversion tests have been performed, either through assimilating the raw measurements, or the bias-corrected dust observations using either the CTM or machine learning model.*

This chapter has been published in Jin et al. (2019):
Machine learning for observation bias correction with application to dust storm data assimilation.
Atmospheric Chemistry and Physics, 19(15), 10009-10026.

4.1. INTRODUCTION

IN general, the commonly used data assimilation schemes all rely on the basic assumption of an unbiased observation. In real applications, however, measurement biases are often unavoidable. In the presence of biases, it is impossible to determine whether a difference between an *a prior* simulation and an observation are due to the biased observations or model deficiencies. The biases might lead to assimilations that diverge from reality (Lorente-Plazas and Hacker, 2017). A well known example of observation biases is in radiance observation assimilation systems in presence of clouds (Berry and Harlim, 2017, Eyre, 2016). To avoid problems with these biases, up to 99% of cloudy observed measurements are discarded although they may also contain valuable information. If dust storms are coincident with clouds, it is also possible that in satellite retrieval algorithms clouds are mistaken for dust, leading to strong biases in the data to be assimilated (Chapter 5).

Another example where observation biases are important is when ground-based PM_{10} measurements are assimilated in dust simulation models. Due to the high temporal resolutions and the rather dense observation network, the ground-based air quality observing network has become a powerful source of measurements on dust aerosols. The records, mainly the PM_{10} feature, were widely used to calibrate, assess or estimate the dust model (Benedetti et al., 2018, Huneeus et al., 2011, Lin et al., 2008, Wang et al., 2008, Yumimoto et al., 2016). However, the observed PM_{10} concentrations do not only consist of dusts, but are actually the sum of the dust and other regular particles. The latter one are emitted not only from anthropogenic activities such as industries, vehicles, and households, but also from natural sources such as wild fires and sea spray. In this paper we will simply refer to these particles as the *non-dust* fraction of the total PM_{10}. The concentrations of *non-dust* aerosols in urbanized areas could be substantial, reaching values up to 500 $\mu g/m^3$ (Shao et al., 2018).

Although PM_{10} observations include a nontrivial bias, the wide spread availability makes them still useful in dust storm assimilation system. During dust storm events, extreme high peaks of more than 1000-2000 $\mu g/m^3$ PM_{10} are recorded which can be attributed mainly to dust. If these would be assimilated directly in dust simulation model, ignoring the fact that at least some part represents *non-dust*, the assimilation system would diverge to states that overestimate the dust load. In case of less severe dust events, the dust analysis divergence would then become extremely critical.

However, modeling of observation biases is very challenging when they have strong spatial and temporal variabilities. Little progress has been made in bias correction of full-aerosol measurements for their use in dust storm data assimilation. Lin et al. (2008) selected only PM_{10} observations for assimilation when at least one occurrence of dust clouds was reported by the local stations. In Chapter 3, it was found that on sites with both PM_{10} and $PM_{2.5}$ observations, only the PM_{10} concentration increased during a dust episode, while the $PM_{2.5}$ concentrations were not affected and remained at a constant level. Besides, Xu et al. (2017) and Chapter 3 suggested a strong correlation between $PM_{2.5}$ and *non-dust* PM_{10}. Therefore, a very simple *non-dust* PM_{10} baseline removal (called observation bias correction) was proposed, in which the available $PM_{2.5}$ was used

to approximate the *non-dust* PM_{10} (or baseline) during a dust event by:

$$PM_{10}^{non\text{-}dust} = b + r \times PM_{2.5} \tag{4.1}$$

where the b and $r > 1$ are linear regression parameters based on a 24-hour history of measurements before arrival of the dust storm. The aforementioned methods either exclude a selection of the measurements, which may still contain useful information, or work under ideal circumstance only when a simple correlation $\mathcal{R}$ between PM_{10} and $PM_{2.5}$ is valid. For instance, in the dust event studied in Chapter 3 the application of Eq. 4.1 in many sites failed since $\mathcal{R}$ is weak. To have a quality-assured bias correction, Eq. 4.1 is performed only when the *Pearson* correlation coefficient $\mathcal{R} > 0.8$. Consequently, measurements in around 45% sites are rejected in that case. To fully exploit the dust information present in total PM observations, a more advanced method is needed. In this paper we proposed two methods, either using a conventional chemical transport model, or a machine learning model.

A chemical transport model (CTM) implements all available knowledge on emission, transport, deposition, and other physical processes in order to simulate concentrations of trace gases and, important here, aerosols. Daily air quality forecasts are often provided using such CTMs. A simulation model for dust storm events is usually just a CTM with all tracers removed except dust; by using the full CTM, an estimate of the *non-dust* part of the aerosol load could be made. In this Chapter, the LOTOS-EUROS CTM is used to simulate the dust as well as the *non-dust* aerosol concentrations. If the non-dust model was perfect, the difference between simulation and observed PM_{10} would be unbiased, and assimilation could be applied to the combined dust and *non-dust* concentrations. In case of a dust storm event, it remains necessary to distinguish between the dust and *non-dust* part of the simulations since the two parts will have very different error characteristics. The dust part is quickly varying and has a large uncertainty, while the *non-dust* part is more smooth but very persistent in time and has a relatively small uncertainty. An assimilation system on the combined simulations should be able to handle these differences. However, the error attribution to their proper sources (dust and *non-dust* error) then becomes extremely critical as explained in Chapter 4.2.1. Since this paper focuses on dust during a severe event only, we will not explore the error characteristics of the *non-dust* part of the model. Therefore we will not apply an assimilation on the combined aerosol (dust and *non-dust*) model. Instead, the *non-dust* simulations will solely be used to remove the *non-dust* baseline from PM_{10} observations.

Similar to the air quality forecast, the accuracy of a CTM for *non-dust* aerosols is hampered by lack of accurate input data. For example, the timely update of anthropogenic emission inventories is always a key issue for air quality forecasts. With the ever-increasing complexity and resolution, the CTMs are now becoming highly nonlinear and time-consuming. However, they may still not be able to identify explicit representations of the non-dust aerosol dynamics, especially regarding fine-scale processes.

In addition to the conventional CTM, we propose a new method for removing the *non-dust* part of the PM_{10} observations which is based on machine learning (ML). Data-driven methods have already been proved to be a powerful tool to provide air quality forecasts for horizons of a few days, (e.g., Chen et al. (2018), Fan et al. (2017), Li et al. (2016, 2017)). Different from the chemical transport models which simulate the

aerosol physical processes, machine learning models describe mathematical relations of input-output and trained by learning a large number of samples from historical records. Our machine learning system used a neural network, namely *long short term memory* (LSTM). The input is formed by air quality indices for a number of relevant tracers (PM2.5, SO_2, NO_2, CO, and O_3), as well as meteorology data. The output of the system is an estimate of the *non-dust* PM_{10} concentration. The input features are to a large extent independent of the dust storms, even the $PM_{2.5}$ concentrations as shown in Chapter 3; observations of PM_{10} are excluded since excessive dust loads are visible mainly in this component. Recent development and the availability of open source machine learning tools provide a good opportunity to estimate the air quality indices using a data-driven machine learning models.

Whereas these are previous studies on dust storm data assimilation using various kinds of combined aerosol measurements, we are the first to investigate the necessities of bias correction for these full-aerosol observations in order to use them as 'real' dust measurements in a dust storm assimilation system. The adding values of observation bias correction in dust emission inversion is explored through the ground-based PM_{10} measurement assimilation. It can easily be applied to others general applications, e.g., remote sensing data assimilation. Our contributions are threefold. Firstly, we present and examine the conventional CTM for removing the *non-dust* part from PM_{10} observations. Secondly, we design and examine a novel machine learning based bias correction which is data-driven and free of the time-consuming numerical CTMs. Thirdly, we evaluate the two *non-dust* aerosol model simulations by comparing to the PM_{10} measurements during regular periods (rare dust events involved); we evaluate dust emission fields, surface dust concentration simulation and forecast skills which are obtained by either assimilating the raw PM_{10} data, or bias-corrected measurements either using the CTM or machine learning model.

The paper is organized as follows. The biased observation representing error and its influence on the assimilation system are also explained in Chpater 4.2. The two bias correction methods, the *non-dust* aerosol regional chemical transport model and a machine learning model, are discussed and the bias simulation is evaluated in Chapter 4.3. Chapter 4.4 reports the assimilation results using the two bias correction methods, and evaluates the forecast skills using independent measurements. Chapter 4.5 discusses the necessities of observation bias correction in assimilation works, highlights our key contributions.

4.2. EMISSION INVERSION SYSTEM

The assimilation system, which will be used to combine bias-corrected PM_{10} observations with simulations, is based on a reduced-tangent-linearization four dimensional variational (4DVar) data assimilation developed in Chpater 3. The errors in dust emission field were assumed to be only caused by the uncertainty in the friction velocity threshold in the dust windblown parametrization. To fully resolve the observation-minus-simulation errors, LOTOS-EUROS/dust in this chapter is configured with a higher model resolution of 0.25°.

4.2.1. BIASED OBSERVATION REPRESENTING ERROR

In real applications, the observations inevitably have biases which cannot be attributed to the model simulation, as following:

$$\boldsymbol{y}_i = \mathcal{H}_i(\,\mathcal{M}_i(\boldsymbol{f})\,) + \boldsymbol{b}_i + \boldsymbol{\sigma}_i \tag{4.2}$$

where $\boldsymbol{\sigma}_i$ is the vector of Gaussian distributed observation errors which have zero means and a known covariance matrix $\mathbf{R}_i$, and $\boldsymbol{b}_i$ denotes the vector of observation bias. In our application, the vector $\boldsymbol{y}_i$ contains the observed PM_{10} concentrations, while the aerosols released in the local anthropogenic activities and other *non-dust* related processes are referred as $\boldsymbol{b}_i$. Note that the PM_{10} measurements themselves might also contain 'native' biases due to the incorrect sensor reading or systematic errors. However, this part of the bias in the PM_{10} observations is unknown and not considered in this thesis.

In the course of data assimilation, it is impossible to determine whether the departures ($\boldsymbol{d}_i$) of the prior simulations from the observations are due to the biased observations $\boldsymbol{b}_i$ or emission errors $\delta\boldsymbol{f}$. Thus, the assimilation result will diverge from the true state when a bias is present. In complex dynamic models as the atmospheric transport model, the biases (*non-dust* aerosols) could have high spatial and temporal variabilities and is therefore difficult to quantify.

In this work, we proposed two methods to quantify the bias levels for the observation bias correction. The first one is the *non-dust* parts of LOTOS-EUROS chemical transport model (CTM) which simulates the aerosol life cycles including emission, transport and deposition. The second method is to describe the *non-dust* aerosol levels using a data-driven machine machine model. Details of these two methods are illustrated in Chapter 4.3.

In fact, both LOTOS-EUROS CTM and machine learning model are imperfect, and some biases might still exist after the correction. The former one is known to be limited by errors in the emission inventories, meteorological forecasts and all kinds of input sources. The latter is then hampered by the deficiency of the type model (e.g., insufficient to represent the complexity of the phenomenon), inadequate amount of training data. However, by combining the bias-corrected observation with the dust model, the assimilation will adapt to posteriors which are more close to reality.

There were a few studies that addressed both the model deficiency and uncertainty in observation bias simultaneously using either variational data assimilation (Dee and Uppala, 2009) or sequential filters (Dee, 2005, Lorente-Plazas and Hacker, 2017). Those assimilation schemes not only require a formulation of a model for the bias, but also need a quality-assured reference to describe the uncertainty of the bias model. The need to attribute errors to their proper sources is obviously a key part in any assimilation systems, but becomes especially critical when it involves bias correction. This is because a wrong error attribution will force the assimilation to be consistent with a biased source. If the source of a known bias is uncertain, assimilation without considering the uncertainty of bias model is the safest option (Dee, 2005). Therefore, these two *non-dust* models are solely set as references for the bias, and the uncertainties are not explored here.

4.2.2. ASSIMILATION WINDOW

Fig. 4.1 shows a time line for the assimilation experiment around the April 2015 dust event, which is very similar to what was used in Chapter 3. The dust event has a short duration, and therefore only a single assimilation window with a length of 36 hours is used. The dust emissions take place at the start of the window, while the observations become available at the end of the window since they are located downwind from the source region (see Fig. 4.2). A long assimilation window is therefore necessary in order to estimate the correct emission parameters given the observations.

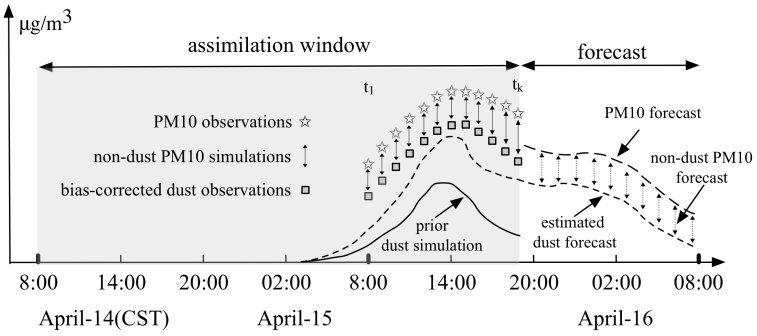

Figure 4.1: Timeline of observation availability, assimilation cycles and forecasts

When we perform the assimilation analysis at April 15, 19:00, only the dust observations from April 15, 08:00 to 19:00 will be assimilated and they are calculated by subtracting the *non-dust* part (CTM based or ML based) from the PM_{10} observations. After the analysis, the simulation model is used to perform a dust forecast for the next 12 hours using the newly-estimated emission parameters. A full-aerosol PM_{10} forecast will then be calculated by adding the dust forecast and *non-dust* aerosol forecast, where the later again originates from either the CTM and machine learning model.

4.3. OBSERVATION BIAS CORRECTION METHODS

Two systems are introduced to correct the *non-dust* bias when using PM_{10} observations in a dust assimilation. The first one is CTM LOTOS-EUROS/*non-dust* model that simulates the physical processes of the *non-dust* aerosols. The latter is the machine learning model that estimates the *non-dust* aerosol based on historical records. The following sections describe the two methods in more detail.

4.3.1. CHEMICAL TRANSPORT MODEL (LOTOS-EUROS/*non-dust*)

The regional CTM LOTOS-EUROS/*non-dust* is configured similar to the LOTOS-EUROS/dust used in the assimilation, but now includes all trace gases and *non-dust* aerosols. The configuration is similar to what is used for daily air quality simulations over China as described in (Timmermans et al., 2017). Anthropogenic emissions are taken from the Multi-resolution Emission Inventory for China (MEIC) inventory[1]. Natural emissions in-

[1] http://www.meicmodel.org

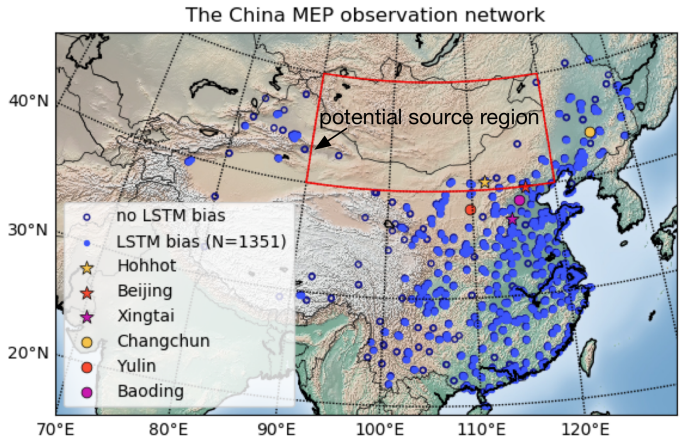

Figure 4.2: The China MEP air quality monitoring network and the potential dust storm source region. LSTM based *non-dust* PM_{10} forecast are performed only in stations of blue dot (N=1351), while ones of black circles are skipped.

cluded are the sea salts that are calculated online, biogenic emissions that are calculated online using the MEGAN model (Guenther et al., 2006), and wild fires which were taken from the operational GRAS product (Kaiser et al., 2012). The LOTOS-EUROS full aerosol operational forecast over this modeling domain are released via the MarcoPolo-Panda projects through (www.marcopolo-panda.eu).

The operational CTM Lotos-Euros over China is in its early phase of development as well as the other six CTMs used in the MarcoPolo-Panda project. The purpose of that project is to diagnose statistical differences between the ensemble model simulations and observations. An important objective is to determine ways by which the models can be improved. These differences are mostly attributed to inaccuracy in the weather forecast and errors in the adopted surface emissions (Brasseur et al., 2019, Petersen et al., 2019). Indeed, there is room for minimizing the forecast-observation differences using nudging methods like data assimilation, which requires considerable efforts and not yet exploited in that thesis.

4.3.2. MACHINE LEARNING FOR *non-dust* PM_{10} SIMULATIONS

Given a set of training data, a machine learning algorithm attempts to find the relation between input and output. When a proper model is used, the machine learning algorithm can lean to reproduce the complex behaviors of a dynamic system. The description is purely based on the data, physical knowledge is not included. Machine learning algorithms are popular tools to forecast the air quality indices using the history records (Chen et al., 2018, Fan et al., 2017, Li et al., 2016, X. et al., 2019). In this study, the machine learning algorithm used is the *long short term memory* (LSTM) neural network, which has demonstrated its ability in predicting time series problems (Li et al., 2017).

The LSTM operator $\mathcal{L}$, which is configured with parameters $\boldsymbol{\theta}$, for predicting *non-*

dust PM_{10} can be described as:

$$\boldsymbol{b}^{t_0+t} = \mathcal{L}_{\boldsymbol{\theta}}(\boldsymbol{x}^{t_0},\ \boldsymbol{x}^{t_0-1},\ ...,\ \boldsymbol{x}^{t_0-m+1}) \tag{4.3}$$

where $\boldsymbol{b}^{t_0+t}$ represents the predictor, which is in this study the *non-dust* PM_{10} concentration forecast t hours in advance. The temporal correlation between the input and output features declines when t increases. In our system, the maximum forecast period t is 12 hours. The input vectors $\boldsymbol{x}^{t_0}, \boldsymbol{x}^{t_0-1}, ..., \boldsymbol{x}^{t_0-m+1}$ are the observed data of the past m hours, which is set as 18 hours empirically. The input vectors consist of:

- hourly observations of $PM_{2.5}$, SO_2, NO_2, O_3, and CO from the ground based air quality network in Fig. 4.2;
- observations of $PM_{2.5}$ at the nearby sites;
- local meteorological data (temperature and dew point at 2 m, wind speed at 10 m) which are taken from the LOTOS-EUROS model input and originate from the European Center for Medium-Ranged Weather Forecast (ECMWF).

The LSTM neural network parameters $\boldsymbol{\theta}$ are determined by minimizing the objective function $\mathcal{J}_{\boldsymbol{\theta}}$ that represents the mean squared error of predictors $\boldsymbol{b}$ with respect to the measured values $\boldsymbol{y}^b$:

$$\mathcal{J}_{\theta} = \frac{1}{m}\sum_{i=1}^{m}(\boldsymbol{b}_i - \boldsymbol{y}_i^b)^2 \tag{4.4}$$

The training dataset covers the period from January 2013 to March 2015. In other words, the LSTM model $\mathcal{L}$ is trained to best fit the samples from this period. The two months April and May 2015 in which the studied dust event occurred is set as the testing period.

Dust storms themselves occur with very low frequency. To our knowledge, the studied dust event is the most severe one since 2002, and there are no such large-scale dust events recorded in our training period. Note that cities that are close to the Gobi and Mongolia deserts might have experienced several small-scale dust events with limited increase of dust concentrations. However, the machine learning tries to find the global best fits for the whole training dataset. The default learning rate, which determines the weights are updated during training, on a simple sample is 10^{-4} in our machine learning algorithm. Therefore, the PM_{10} records $\boldsymbol{y}^b$ are very close to the *non-dust* PM_{10} concentrations, and the rare dust event records are not excluded from the training dataset for convenience and for the expected little impact on the training result. The regression model $\mathcal{L}$ is thus assumed to reflect only the relation between input features and the *non-dust* PM_{10}.

Note that including PM_{10} observations in the series of input vectors will certainly improve the skill of the machine learning forecasts. However, the LSTM model would then lack the ability to discriminate between the dust and *non-dust* fractions in PM_{10} during a dust event. Earlier studies showed that the input variables, including $PM_{2.5}$, are independent on the dust storm as illustrated in Chapter 3.

For the non-dust PM_{10} machine learning forecasts in a given site, observations from its nearby sites are also vital and are used in two ways. First, missing data records are

unavoidable in an air quality monitoring network, while the LSTM model training requires an uninterrupted time series of features. In this study, data interpolations of air quality measurements (PM_{10}, $PM_{2.5}$, SO_2, NO_2, O_3 and CO) are performed using both a linear interpolation and a k-Nearest-Neighbor algorithm (Zhang, 2012) if a site has no more than 30% of missing data. Otherwise, all the measurements in the given sites are abandoned. Generally, more information available from the nearby sites will result in a more accurate interpolation. Second, learning in the presence of data errors is pervasive in machine learning, and the measurements from nearby stations are used to limit their influence. Data errors occur due to incorrect sensor readings, software bugs in the data processing pipeline, or even the inaccurate data interpolation. Statistical analysis tests have been conducted which did not only indicate a strong correlation between the non-dust PM_{10} and air quality measurements in the given sites, but also show that the predictor (non-dust PM_{10}) is correlated to the observation indices (especially the $PM_{2.5}$) at its nearby sites. In order to eliminating errors caused by incorrect inputs at the modeling site, the measurements at the nearby stations are considered as the essential indices. In this study, a data instance will only be selected for training the LSTM model if there is at least one nearby site within an empirical radius 0.8°(approx 80 km), and a maximum of 3 nearby sites will be randomly selected where observation stations are densely distributed. To save the computation costs on machine learning model training, only the $PM_{2.5}$ from the nearby sites are included as one of the inputs in this study.

The machine learning model for non-dust PM_{10} forecast is trained site by site, with the hyper-parameters shown in Table 4.1. With the following hyper-parameters, the machine learning model training takes several minutes for each site. The training in each site is independent, hence, the whole workload is highly parallelizable.

Table 4.1: LSTM hyper-parameters.

LSTM layers	neurons per layer	epochs	batch size	forecast length (hours)
2	30	50	64	0 or 12

Fig. 4.2 presents the original field observation network (N≈1500) established by the China Ministry of Environmental Protection (MEP) up to 2018, as well as the sites (N=1351) where LSTM based *non-dust* forecasts are performed. It is clear that the LSTM forecast cannot be performed in each monitoring site. A part of the sites is skipped due to the lack of nearby sites, the rest are caused by high data missing rate in the training period.

4.3.3. EVALUATION OF *non-dust* PM_{10} BIAS CORRECTIONS

Our two bias models, LOTOS-EUROS/*non-dust* and LSTM, could both be used for air quality forecast operationally when there is no dust storm. Once a dust storm is observed, the dust emission inversion system will be enabled, the two non-dust PM_{10} models will then be used in dust observation bias correction. The forecasts are expected to have a good performance when dust is not present, and to underestimate the PM_{10} levels in case of dust storms.

Both the CTM LOTOS-EUROS and LSTM are tested to forecast *non-dust* PM_{10} over April-May 2015. This period includes the 2 to 3 days dust event that is used as test case for the assimilation. Fig. 4.3(a)~(c) show density plots comparing PM_{10} observations with

either LOTOS-EUROS/*non-dust* forecasts, or with LSTM forecast 0 hour and 12 hours in advance.

The CTM LOTOS-EUROS/*non-dust* in general underestimates the *non-dust* PM_{10}. The forecast results in a relatively large root mean square error (RMSE) 89.4 $\mu g/m^3$. This could be explained from the fact not all types of particulate matters, such as secondary organic aerosols, are included in the model, and some aerosol emissions are very difficult to estimate (e.g., wood burning by households). The two LSTM forecasts show on average a good agreement with the observations. The RMSEs of the forecasts by the two machine learning models in the two years of training period are reduced to 55.9 and 60.7 $\mu g/m^3$, and in the two months of test period (excluding the dust event from April 14 to 16) they also stay at comparable low levels of 58.6 and 60.2 $\mu g/m^3$. As expected, a smaller forecast period t=0 hour gives a better result than the forecast over 12 hours.

The scatters in the dust period (April 14 to 16) are denoted using different markers in Fig. 4.3. The underestimation of PM_{10} during the dust period (April 14 to 16) is visible in the bottom right corners of these plots.

When we perform the assimilation analysis at April 15, 19:00, the short period of t=0 hour forecast will be treated as the *non-dust* levels in the bias correction of the original PM_{10} measurements. Note that here t=0 forecasts denote the forecasts valid at each specific snapshot of the observations, while the 12 hours forecasts are valid 12 hours in advance, e.g., the non-dust PM_{10} forecast (12 h) at April 16 07:00 is valid at April 15 19:00. Subsequently, the bias-corrected data are used to estimate the dust emissions over the past 36-hour window. Obviously, one important aim of the assimilation is to make a better forecast, in this study, the forecast skills will be evaluated in the following 12 hours from April 15, 19:00. Besides, the forecast is assessed by comparing the combined PM_{10} forecasts to PM_{10} observations. The LSTM forecast with t=12 hours in advance will be added to the dust storm forecast to build the combined aerosol forecast.

SPATIAL PATTERNS AT OBSERVATION SITES

To assess our two *non-dust* PM_{10} models, Fig. 4.4 shows the snapshots of the PM_{10} measurements, LOTOS-EUROS/*non-dust* simulations, LSTM forecasts, and the corresponding bias-corrected dust observations at three timestamps: April 15 08:00, 19:00 and 22:00. These first two moments are the start and end of the observation interval in the assimilation window (only observations from the last 12 hours of the assimilation window are assimilated as shown in Fig. 4.1), and observations at 22:00 is treated as independent data for cross-validation. At 08:00, actually only few stations close to the dust source area have already observed the dust storm. Some of the sites in central China observed high PM_{10} concentrations which are believed to be caused by presence of *non-dust* aerosols. Nearly all the stations in north China reported this dust storm at 19:00 and 22:00, as a band covering central and northeast China, see Fig. 4.4 (a.2)~(a.3). Fig. 4.4 (b.1)~(b.3) shows that the LOTOS-EUROS/*non-dust* model forecasts quite stable and constant *non-dust* PM_{10} levels, most of the simulated values are less than 100 $\mu g/m^3$. Subsequently, the corresponding bias-corrected dust measurements (see Fig.4.4 (c.1)~(c.3)) are very similar to the original PM_{10} observations. This could be problematic when trying to measure the dust storm from the PM_{10} observations; for instance at 08:00 in Fig. 4.4 (c.1), according to the bias-corrected observations the dust storm seems to have already reached central

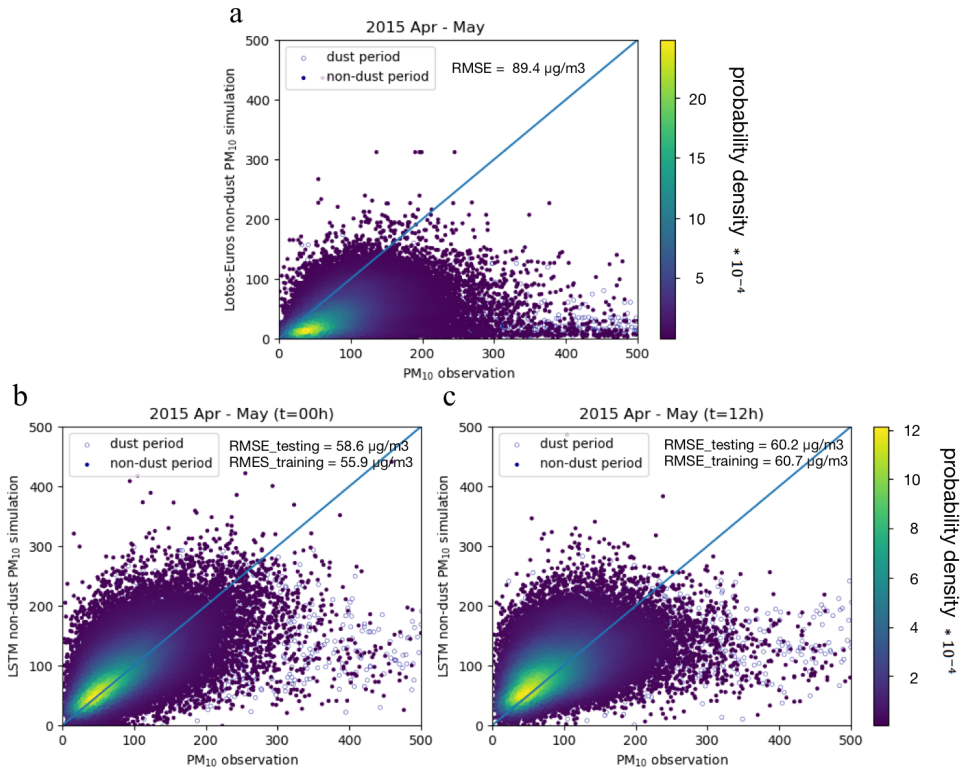

Figure 4.3: *Non-dust* PM_{10} simulation evaluations. (a): LOTOS-EUROS/*non-dust* forecast vs. PM_{10} measurements; (b): LSTM forecast 0 hour in advance vs. PM_{10} measurements; (c): LSTM forecast 12 hour in advance vs. PM_{10} measurements; (NOTE: the solid circles show the 5% random samples over the non-dust period from April to May 2015 while the hollow ones denote the 5% random ones from the dust period (April 14 to 16).

China which was probably not the case. In comparison, the LSTM based bias-corrected dust observations (see Fig. 4.4 (e.1)~(e.3)), which is calculated by subtracting the LSTM *non-dust* part (see Fig. 4.4(d.1)~(d.3)) from the raw PM_{10} measurements, are close to our expectations. Only for sites that are very close to the source regions high dust concentrations are derived at 08:00, while for the other sites hardly any dust is derived. At 19:00, thus 11 hours later, at half of the stations in the north of the domain high dust concentrations are derived. In the southeast of the domain, the derived dust concentrations remain almost zero since the dust plume did not arrive there yet. At 22:00, the plume is moved further south, and the dust load closer to the source region started to decrease.

TIME SERIES

To further evaluate the two bias correction methods, Fig. 4.5 shows the time series at the following selected cities: Hohhot, Changchun, Beijing, Baoding, Xingtai and Yulin. The location of these cities/sites can be found in Fig. 4.2. These cities were selected because they all experienced a severe pollution and illustrated the general performance of the LOTOS-EUROS/*non-dust* and LSTM methods. In addition, each of these cities have at least 4 monitoring sites which assured a high accuracy.

The LOTOS-EUROS grid cells with the selected sites all include other observation sites as well, and to illustrate the spread in the observations the maximum and minimum observed values in the grid cell are added to the time series too. Similarly, the LSTM *non-dust* PM_{10} simulation is given together with the spread within the grid cell.

Before the dust storm arrived at these cites, the LSTM model reproduces the variations in PM_{10} rather well. Some errors are present, for example as can be seen on April 14 from 12:00 to 23:00 in Yulin. After the arrival of the dust storm, the PM_{10} observations strongly increase, while the LSTM *non-dust* fraction remains at a low level since it is independent of the dust storm. The real dust measurement is then calculated by subtracting the *non-dust* part from the raw PM_{10} observations.

The LOTOS-EUROS/*non-dust* simulations underestimate the *non-dust* PM_{10} at all the six locations. Thus, the derived bias-corrected dust observations overestimate the actual dust load, and this will affect the dust assimilation results.

4.4. DATA ASSIMILATION EXPERIMENTS

Three different sets of observations are now available for assimilation in the dust model: the original PM_{10} observations, the PM_{10} observations with LOTOS-EUROS bias correction, and the PM_{10} observations with machine learning bias correction. The results have been compared in terms of the posterior dust emission fields and surface dust concentrations.

A practical use of assimilated concentrations is to use them as a start point for a forecast. This could be used to provide early information about the arrival of the dust plume and the expected dust level. The dust forecast after the end of the assimilation window at April 15 19:00 uses the newly estimated emissions. Apart from the dust concentrations, the forecast will also be evaluated in terms of skill scores for the total PM_{10} concentrations in Chapter 4.4.3.

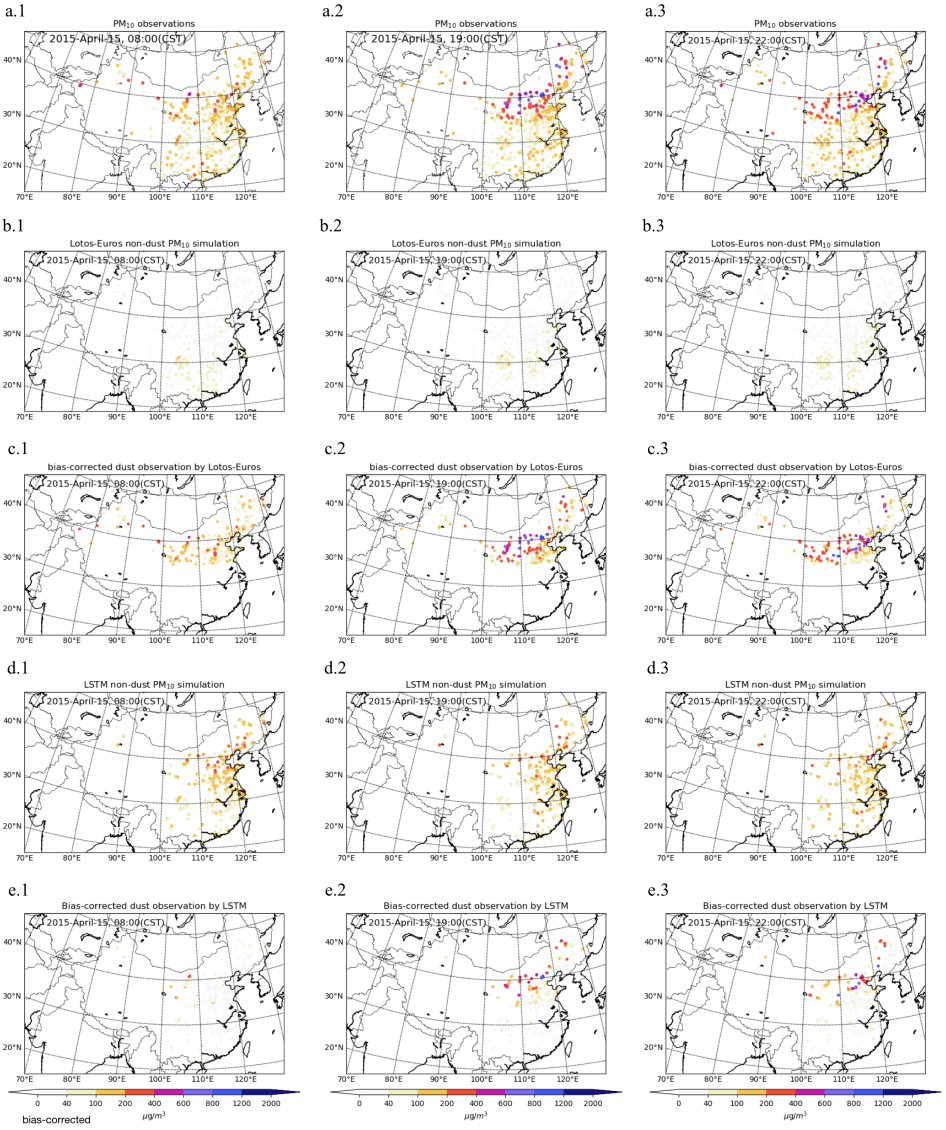

Figure 4.4: Original PM_{10} measurements (a.1~a.3), LOTOS-EUROS/*non-dust* simulated PM_{10} (b.1~b.3) and the corresponding bias-corrected dust observations (c.1~c.3), LSTM predicted *non-dust* PM_{10} (d.1~d.3) and the derived dust observations (e.1~e.3) at three time snapshots: April 15, 08:00 (a.1~e.1), 19:00 (a.2~e.2) and 22:00 (a.3~e.3)

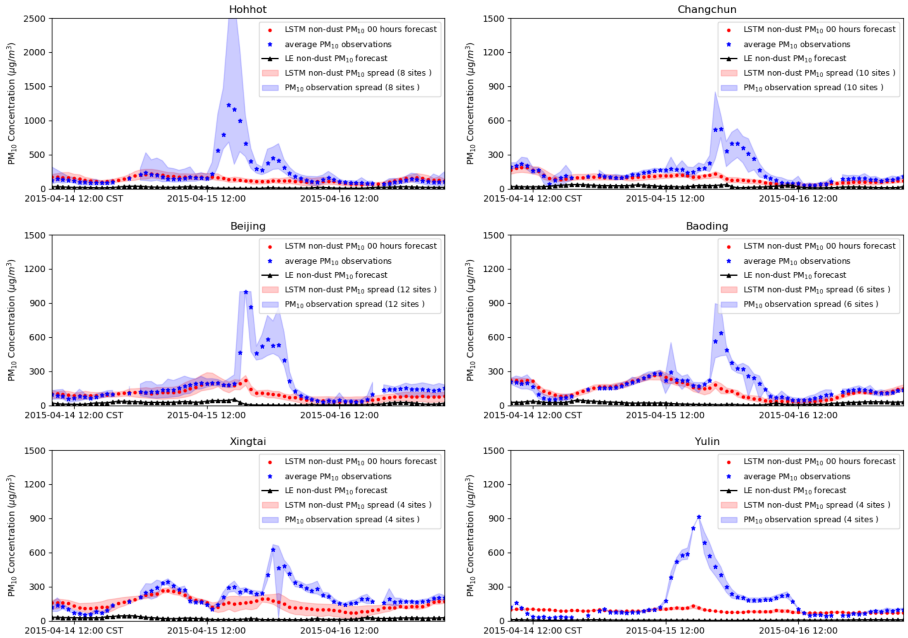

Figure 4.5: Time series of PM_{10} measurements, LOTOS-EUROS/*non-dust* and LSTM predicted PM_{10} levels at six cities: Hohhot, Changchun, Beijing, Baoding, Xingtai and Yulin. LE: LOTOS-EUROS; LSTM: long short-term memory.

4.4.1. OBSERVATION ERROR CONFIGURATION

A key element of the data assimilation system is the observation error covariance matrix **R**. This covariance quantifies the possible difference between simulations and observations. The observations with a smaller error have a higher weight in the assimilation process.

In related works, the dust observation errors were usually empirically quantified. Lin et al. (2008) assumed that the observation error is proportional to the measurement with a constant factor of 10%. Chapter 3 used a similar error setting but also assigned a larger error to low valued measurements since the model might easily results in relative large errors when simulating minor dust loads.

Theoretically, the observation uncertainties are due to the representation errors as well as the measurement errors, while the former one is widely considered as the largest source. Limited by the computation resources, our dust model uses a spatial resolution of 25 km, while the in-situ measurements cover the much less of atmosphere surrounding them (Schutgens et al., 2016). This of course limits our capability of resolving the fine-scale fields that are reflected in observation spaces. Therefore, the spatial representation error is assumed to be the dominant error source and taken into the account in approximating the observation uncertainties. In addition, the error due to the different bias correction terms is indeed another source. It is not yet considered in this study but will be exploited for a more accurate assimilation operation in our future work.

The spatial representation error quantification itself is a complex task. It could be calculated through comparing the model simulations at different scales of resolutions. In this study, the availability of multiple measurement sites in a single model grid cell provides an alternative way to quantify the representation error. When multiple observations are present, the statistical error in the observed values reflects the spatial representation uncertainty. An example is the grid cell covering the city of Beijing, where observations from 12 different field stations are available. Note that it is the grid cell which has the most monitoring stations. The spread of the hourly measurements is shown in Fig. 4.5(c). For each hour, the standard deviation of the measured PM_{10} values is plotted against the mean in Fig. 4.6, where the red markers represent 'regular' polluted conditions, and the blue markers the dust event. The result shows that the spread in the observations closely agrees with the average pollution level during the dust event. Based on this result, a simple linear regression is used to obtain a parametrization for the observation representation error:

$$\sigma = \max(\, a \cdot y + b\,,\ \sigma_{min}\,) \qquad [\mu g/m^3] \tag{4.5}$$

where $a = 0.12$ and $b = 55.7$ are the linear regression parameters based on the dust event data (blue markers). It should be noted that the observation sites in Beijing truncate observations at a maximum of 1000 $\mu g/m^3$, and therefore observations close to this number are not used since the true values might have been much higher. A minimum observation representation uncertainty of $\sigma_{min} = 100\ \mu g/m^3$ is used for the 'dust' observations (PM_{10} with bias correction) to avoid a too strong impact of low valued observations (hardly dust) on the estimation of dust emissions. In case the simulation model estimates dust concentrations at the surface while in reality the plume is elevated, the low valued observations might lead to an unrealistic strong decrease of the dust emis-

sions.

The representation uncertainty has already been validated to fluctuate in space (Schutgens et al., 2016). However, for most other grid cells the number of observations sites is simply one, which makes it difficult to parametrize a representation error in a similar way. Therefore, the representation error parametrized for Beijing is used for all other locations too.

Note that the raw PM_{10} and the bias-corrected dust measurements might have different uncertainties in representing the real dust storm level. This is not yet taken into account in our study, and the three types of the assimilated measurements, raw PM_{10}, bias-corrected dust observation either using the CTM or using the machine learning, are all configured with the same observation error in Eq.4.5. In addition, all the measurements are assumed to be independent, hence, the observation error covariance **R** is diagonal.

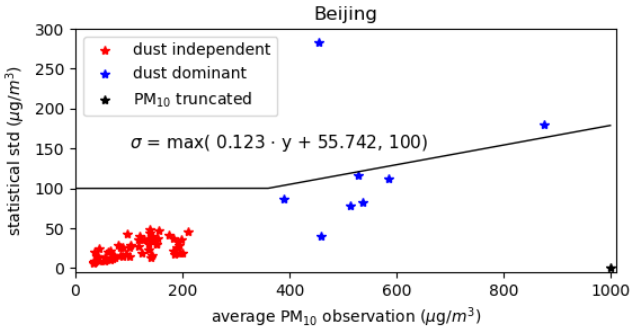

Figure 4.6: Average vs. Standard deviation of the hourly PM_{10} observations range from April 14 08:00 to April 17 07:00 in the grid cell of Beijing. See Fig. 4.5(c) for the time series.

4.4.2. DUST EMISSION ESTIMATION

To evaluate the posterior dust emission field that is obtained by assimilation of the bias corrected 'dust' observations, an emission index $\mathcal{F}_i$ (g/m^2) is defined as in Chapter 3. The index represents the accumulated dust emission in a cell i between April 14 08:00 and April 15 19:00. Fig. 4.7 shows the emission index map of the *a prior* model, and *posteriori* emissions obtained from assimilation of either the original PM_{10} observations, or the LOTOS-EUROS or LSTM based bias-corrected 'dust' measurements.

As shown in Fig.4.7(a), the *a prior* emission was in general rather weak, which resulted in an underestimated surface dust concentration simulation as can be seen for example in Fig. 4.8(a.1)~(a.2). The *posteriori* emissions are almost everywhere higher than the *a prior*. An exception is the black marked region, where the *a prior* emissions are higher. The emissions from this black-dashed region contributed to a too-early arrival of the dust peak in the model cells over Hohhot and Xingtai as shown in Fig. 4.9(a) and (c).

Fig. 4.7 (b) shows the emission index $\mathcal{F}$ that results from directly assimilating the original PM_{10} measurements. As expected the estimated emissions are higher than those

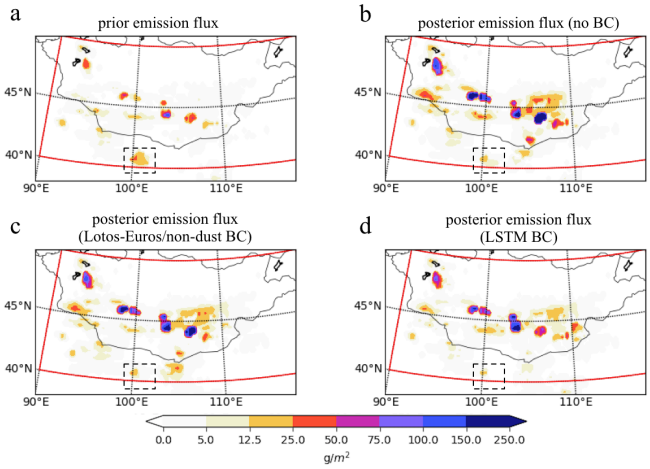

Figure 4.7: Accumulated dust emission map $\mathcal{F}$ between April 14 08:00 and April 15 19:00 of *a priori* model (a), or (b) *a posteriori* estimates using the original PM_{10} observations, (c) LOTOS-EUROS or (d) LSTM based bias-corrected dust measurements. BC: bias correction

obtained by assimilating the bias-corrected observations, since all airborne aerosols observed are attributed to be dust. In comparison, the assimilation with LSTM baseline removed data results in a modest emission level as shown in Fig. 4.7(d). The emissions estimated with LOTOS-EUROS based bias-corrected observations are in between, since the resulting 'dust' observations also overestimate the actual dust loads compared to the LSTM based bias-corrected dust measurements.

4.4.3. DUST SIMULATION AND FORECAST SKILL

Fig. 4.8 (a)~(d) show the dust simulations at the surface layer at the end of the assimilation window (April 15 19:00, left column) and the forecast 3 hours later (22:00, right column) using the newly estimated emission field. Note that the average dust concentration over the affected downwind regions reached at a peak around 22:00. Compared to background simulations in Chapter 3, the *a prior* model simulations have been improved by disabling the topography-based preference factor $\mathcal{S}$ as mentioned in Chapter 2.1.4; however, a large difference from the bias-corrected PM_{10} observations in Fig. 4.4(e) is still present.

The *posteriori* concentrations in Fig. 4.8(b.1)~(b.2) are the result of assimilating the original measurements PM_{10} observations shown in Fig. 4.4(a.1)~(a.2). As expected, these lead to the highest simulated dust concentrations since all the aerosols observed are assumed to represent dust. Especially in the center of the plume, the dust concentration can be as large as 2000 $\mu g/m^3$. Fig. 4.8(c.1)~(c.2) show the results when using the LOTOS-EUROS/*non-dust* bias-corrected PM_{10} observations as 'dust', and although concentrations are lower, they are still likely to overestimate the real dust levels. The *posteriori* results using the LSTM bias-corrected measurements provide the lowest dust concentrations as shown in Fig. 4.8(d). Only in the grid cells that are close to the source

region, the surface dust concentration reach values as large as 2000 $\mu g/m^3$, while in the downwind areas the maximum dust concentrations are usually below 1200 $\mu g/m^3$.

To illustrate the improvements of assimilating bias-corrected measurements, Fig. 4.9 shows the observed and simulated PM_{10} concentrations in the aforementioned grid cells covering Hohhot, Beijing, and Xingtai. These locations are neither the best nor the worst examples, but illustrate typical results and challenges to be solved in future. For a fair comparison with the PM_{10} observations, the non-dust aerosol concentrations obtained from either LOTOS-EUROS/*non-dust* or LSTM were added to the dust simulations from the inversion system.

Site Hohhot is close to the main dust source region. The *a prior* model simulated the arrival of the dust plume 8 hours before it was actually visible in the PM_{10} observations. The assimilation of the observations is able to produce simulations in which the dust plume arrives at the correct time. The assimilation with LSTM bias-corrected data has the best performance, with the peak of the simulated concentrations (dust plus bias) most close to the observed PM_{10}. During the forecast period (t>April 15, 19:00), all three assimilation based forecasts show a decline in concentrations, which slightly overestimate the observations. This can be explained from the fact that the dust storm is a strong flow-dependent phenomenon in which concentrations at a certain location are strongly correlated to earlier concentrations at upwind locations. For Hohhot, only a limited number of observation sites is located upwind, and therefore hardly any data is available to constrain the concentrations at this location. To improve the forecast at Hohhot it will be necessary to have additional observation data, for example from sites actually within the source region, or from satellites observing the aerosol load over the source region.

For the grid cell Beijing, which is located further downwind from the dust source region, the arrival of the dust peak is correctly simulated. However, the amplitude of the concentration peak is underestimated compared to the average PM_{10} observations. As can be seen in Fig. 4.8, the dust plume forms a rather small band over central and northeast China. In each of the three assimilations, the dust concentrations in the band are rather low around Beijing. This suggests that the simulation model simply is not able to increase the dust concentrations here, for example because of uncertainties in the meteorological data, a removal of dust that is too efficient, or because some local sources of dust are absent (equally, non-dust PM_{10} levels are underestimated).

The grid cell Xingtai is located more to the south, and the model is able to simulate high dust concentrations here. The *a prior* model simulates the arrival of a first dust peak already at 13:00, which is however not visible in the PM_{10} data. The assimilation postpones the arrival of the main dust, which according to the measurements takes place around 22:00 and is already in the forecast period. The forecast simulations all overestimate the amplitude of the peak, especially when using the original PM_{10} data as proxy for dust. The assimilation with the LSTM based baseline removal shows the best agreement with the observations.

4.4.4. EVALUATION OF FORECAST SKILL

To evaluate the forecast skill of the assimilation(s), the root mean square error (RMSE) of the reference and three posterior full aerosol simulations (dust forecasts plus *non-dust*

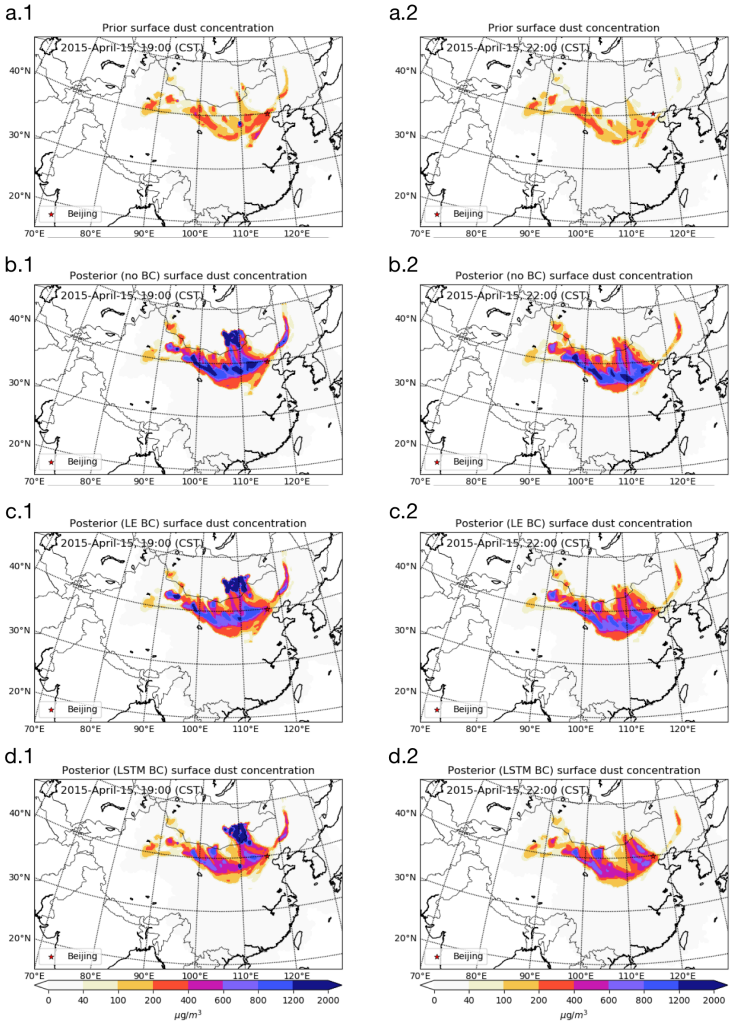

Figure 4.8: Surface dust concentration of *a prior* (a.1~a.2), *posterior* using no bias-corrected (no BC) data (b.1~b.2), *posterior* using LOTOS-EUROS/*non-dust* bias-corrected (LE BC) data (c.1~c.2), *posterior* using no bias-corrected (LSTM BC) data (d.1~d.2) at April 15, 19:00 (a.1~d.1) and 22:00 (a.2~d.2)

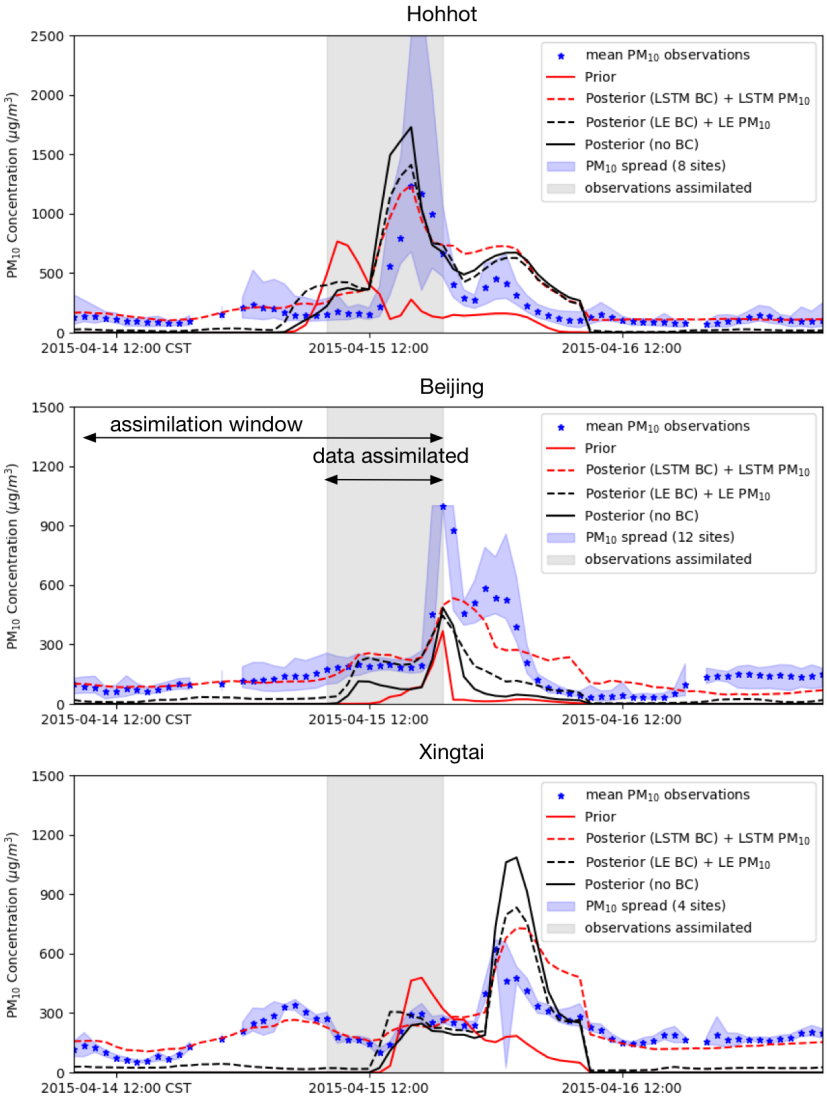

Figure 4.9: Time series of posterior dust concentration and PM_{10} observations in three cities: Hohhot, Beijing, Xingtai (observations in the gray shadow are assimilated)

predictions) with respect to the observed PM_{10} over the whole observation sites has been computed for each hour. A time series of this RMSE is shown in Fig. 4.10; after the assimilation window (marked period), the results are based on the forecast simulations. The *a prior* RMSE values at the end of the assimilation window and during the forecast are about 200-250 $\mu g/m^3$. Direct assimilation of the original PM_{10} measurement actually increases these values to above 300 $\mu g/m^3$ during the forecast, since dust concentrations become strongly overestimated. Assimilation of the LOTOS-EUROS/*non-dust* baseline removed observations nonetheless reduces the RMSE, in particular within the assimilation window. Strongest decrease in RMSE is obtained using the LSTM based baseline removal, with values of 120-200 $\mu g/m^3$ during the forecast.

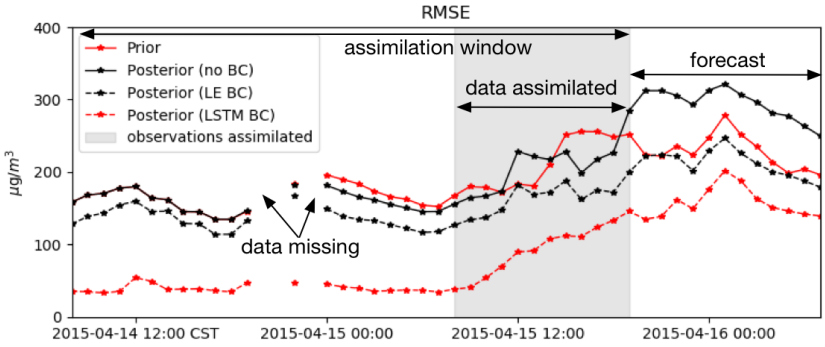

Figure 4.10: Time series of root mean square error compared to the ground PM_{10}. The assimilation window is set from April 14 08:00 to April 15 19:00, and PM_{10} observation in the gray shadow are assimilated.

4.5. CONCLUSIONS

In this Chapter, a dust storm emission inversion experiment has been performed for an event over East Asia in the spring of 2015. PM_{10} observation data from the China Ministry of Environmental Protection observing network were assimilated into a dust simulation model to estimate the dust emissions. The PM_{10} measurements themselves are considered as unbiased. They clearly show the arrival of a dust plume throughout the region due to the high spatiotemporal resolution. However, the data cannot be compared directly to dust simulations since they actually represent a sum of the dust particles and other *non-dust* aerosols. Direct assimilation of these measurements would introduce a bias in the assimilation system, since it cannot distinguish between model and observation errors.

Two methods have been implemented to remove the *non-dust* part the PM_{10} observations during the dust event in order to use them as 'dust' proxy in a dust assimilation system. The first method uses a conventional regional chemical transport model, LOTOS-EUROS/*non-dust*, which simulates the emission, transport, chemistry, and deposition of aerosols mainly related to anthropogenic activities. The second method uses a machine learning model that statistically describes the relations between regular PM_{10} concentrations (outside dust events), and available air quality and meteorological data.

The two methods to estimate the *non-dust* part of the PM_{10} load have been validated. The simulations by the LOTOS-EUROS/*non-dust* model in general underestimate the PM_{10} concentrations. The root mean square error stays at a relative high level of 89.4 $\mu g/m^3$. It is mainly caused by missing emissions and aerosol components such as secondary organic matter. In comparison, the data-driven machine learning model agrees more closely with the real measurements, the RMSE declines to 58.6 $\mu g/m^3$.

A variational data assimilation system has been used to estimate the dust emissions that lead to a severe dust storm in April 2015. The system either assimilated the original PM_{10} observations, or the bias-corrected 'dust' observations based on either LOTOS-EUROS/*non-dust* or LSTM model. The posterior simulations using the original observations resulted in a strong overestimation of the dust concentrations, since all PM_{10} are simply attributed to dust. Using the LOTOS-EUROS/*non-dust* bias-corrected observations, a clear improvement on the dust simulation has been obtained, but overestimation of dust concentrations is still present. The best results are obtained when using a LSTM model to remove the *non-dust* part of the PM_{10} observations, with *posterior* concentrations in good agreement with the measurements.

The dust emissions estimated using the assimilation can be used to drive a dust forecast. When the original PM_{10} observations were used in the assimilation, the forecast skill of the system actually decreased due to the strong overestimation of dust concentrations, the RMSE rose from averagely 230 (prior forecast) to 300 $\mu g/m^3$. Better forecasts are obtained when using the model-based and especially the machine learning based bias-corrected observations. The RMSE of the former one was reduced to 200 $\mu g/m^3$ while the RMSE of the latter one further declined to 150 $\mu g/m^3$.

REFERENCES

Benedetti, A., Di Giuseppe, F., Jones, L., Peuch, V. H., Remy, S., and Zhang, X. (2018). The impact of data assimilation on the prediction of Asian desert dust using an operational 4D-Var system. *Atmospheric Chemistry and Physics Discussions*, pages 1–17.

Berry, T. and Harlim, J. (2017). Correcting Biased Observation Model Error in Data Assimilation. *Monthly Weather Review*, 145(7):2833–2853.

Brasseur, G. P., Xie, Y., Petersen, A. K., Bouarar, I., Flemming, J., Gauss, M., Jiang, F., Kouznetsov, R., Kranenburg, R., Mijling, B., Peuch, V.-H., Pommier, M., Segers, A., Sofiev, M., Timmermans, R., van der A, R., Walters, S., Xu, J., and Zhou, G. (2019). Ensemble forecasts of air quality in eastern china – part 1: Model description and implementation of the marcopolo–panda prediction system, version 1. *Geoscientific Model Development*, 12(1):33–67.

Chen, G., Li, S., Knibbs, L. D., Hamm, N. A. S., Cao, W., Li, T., Guo, J., Ren, H., Abramson, M. J., and Guo, Y. (2018). A machine learning method to estimate PM2.5 concentrations across China with remote sensing, meteorological and land use information. *Science of The Total Environment*, 636:52–60.

Dee, D. P. (2005). Bias and data assimilation. *Quarterly Journal of the Royal Meteorological Society*, 131(613):3323–3343.

Dee, D. P. and Uppala, S. (2009). Variational bias correction of satellite radiance data in the ERA-Interim reanalysis. *Quarterly Journal of the Royal Meteorological Society*, 135(644):1830–1841.

Eyre, J. R. (2016). Observation bias correction schemes in data assimilation systems: a theoretical study of some of their properties. *Quarterly Journal of the Royal Meteorological Society*, 142(699):2284–2291.

Fan, J., Li, Q., Hou, J., Feng, X., Karimian, H., and Lin, S. (2017). A Spatiotemporal Prediction Framework for Air Pollution Based on Deep RNN. *ISPRS Annals of Photogrammetry, Remote Sensing and Spatial Information Sciences*, IV-4/W2:15–22.

Guenther, A., Karl, T., Harley, P., Wiedinmyer, C., Palmer, P. I., and Geron, C. (2006). Estimates of global terrestrial isoprene emissions using megan (model of emissions of gases and aerosols from nature). *Atmospheric Chemistry and Physics*, 6(11):3181–3210.

Huneeus, N., Schulz, M., Balkanski, Y., Griesfeller, J., Prospero, J., Kinne, S., Bauer, S., Boucher, O., Chin, M., Dentener, F., Diehl, T., Easter, R., Fillmore, D., Ghan, S., Ginoux, P., Grini, A., Horowitz, L., Koch, D., Krol, M. C., Landing, W., Liu, X., Mahowald,

N., Miller, R., Morcrette, J. J., Myhre, G., Penner, J., Perlwitz, J., Stier, P., Takemura, T., and Zender, C. S. (2011). Global dust model intercomparison in AeroCom phase I. *Atmospheric Chemistry and Physics*, 11(15):7781–7816.

Jin, J., Lin, H. X., Segers, A., Xie, Y., and Heemink, A. (2019). Machine learning for observation bias correction with application to dust storm data assimilation. *Atmospheric Chemistry and Physics*, 19(15):10009–10026.

Kaiser, J. W., Heil, A., Andreae, M. O., Benedetti, A., Chubarova, N., Jones, L., Morcrette, J.-J., Razinger, M., Schultz, M. G., Suttie, M., and van der Werf, G. R. (2012). Biomass burning emissions estimated with a global fire assimilation system based on observed fire radiative power. *Biogeosciences*, 9(1):527–554.

Li, X., Peng, L., Hu, Y., Shao, J., and Chi, T. (2016). Deep learning architecture for air quality predictions. *Environmental Science and Pollution Research*, 23(22):22408–22417.

Li, X., Peng, L., Yao, X., Cui, S., Hu, Y., You, C., and Chi, T. (2017). Long short-term memory neural network for air pollutant concentration predictions: Method development and evaluation - ScienceDirect. *Environmental Pollution*, 231:997–1004.

Lin, C., Wang, Z., and Zhu, J. (2008). An Ensemble Kalman Filter for severe dust storm data assimilation over China. *Atmospheric Chemistry & Physics*, 8:2975–2983.

Lorente-Plazas, R. and Hacker, J. P. (2017). Observation and Model Bias Estimation in the Presence of Either or Both Sources of Error. *Monthly Weather Review*, 145(7):2683–2696.

Petersen, A. K., Brasseur, G. P., Bouarar, I., Flemming, J., Gauss, M., Jiang, F., Kouznetsov, R., Kranenburg, R., Mijling, B., Peuch, V.-H., Pommier, M., Segers, A., Sofiev, M., Timmermans, R., van der A, R., Walters, S., Xie, Y., Xu, J., and Zhou, G. (2019). Ensemble forecasts of air quality in eastern china – part 2: Evaluation of the marcopolo–panda prediction system, version 1. *Geoscientific Model Development*, 12(3):1241–1266.

Schutgens, N. A. J., Gryspeerdt, E., Weigum, N., Tsyro, S., Goto, D., Schulz, M., and Stier, P. (2016). Will a perfect model agree with perfect observations? the impact of spatial sampling. *Atmospheric Chemistry and Physics*, 16(10):6335–6353.

Shao, P., Tian, H., Sun, Y., Liu, H., Wu, B., Liu, S., Liu, X., Wu, Y., Liang, W., Wang, Y., Gao, J., Xue, Y., Bai, X., Liu, W., Lin, S., and Hu, G. (2018). Characterizing remarkable changes of severe haze events and chemical compositions in multi-size airborne particles (PM1, PM2.5 and PM10) from January 2013 to 2016–2017 winter in Beijing, China. *Atmospheric Environment*, 189:133–144.

Timmermans, R., Kranenburg, R., Manders, A., Hendriks, C., Segers, A., Dammers, E., Zhang, Q., Wang, L., Liu, Z., Zeng, L., Denier van der Gon, H., and Schaap, M. (2017). Source apportionment of PM2.5 across China using LOTOS-EUROS. *Atmospheric Environment*.

Wang, Y. Q., Zhang, X. Y., Gong, S. L., Zhou, C. H., Hu, X. Q., Liu, H. L., Niu, T., and Yang, Y. Q. (2008). Surface observation of sand and dust storm in East Asia and its application in CUACE/Dust. *Atmospheric Chemistry and Physics*, 8(3):545–553.

X., L., Jin, J., and van den Herik, J. (2019). Air Quality Forecast through Integrated Data Assimilation and Machine Learning.

Xu, L., Batterman, S., Chen, F., Li, J., Zhong, X., Feng, Y., Rao, Q., and Chen, F. (2017). Spatiotemporal characteristics of pm2.5 and pm10 at urban and corresponding background sites in 23 cities in china. *Science of The Total Environment*, 599-600:2074 – 2084.

Yumimoto, K., Murakami, H., Tanaka, T. Y., Sekiyama, T. T., Ogi, A., and Maki, T. (2016). Forecasting of Asian dust storm that occurred on May 10–13, 2011, using an ensemble-based data assimilation system. *Particuology*, 28:121–130.

Zhang, S. (2012). Nearest neighbor selection for iteratively kNN imputation. *Journal of Systems and Software*, 85:2541–2552.

5

DUST EMISSION INVERSION USING HIMAWARI-8 AODS

Aerosol optical depths (AODs) from the new Himawari-8 satellite instrument have been assimilated. This advanced geostationary instrument is capable of monitoring the East Asian dust storms which usually have great spatial and temporal variability. The quality of the data has been verified through a comparison with AERONET AODs. Promising results are obtained in AOD assimilation experiments during a dust event in May 2017. The dust emission fields that drive the simulation model are strongly improved by the inverse modeling, and consequently the simulated dust concentrations are in better agreements with the observed AOD as well as ground based observations of PM_{10}. However, some satellite AODs shows significant inconsistence with the simulations and the PM_{10} and AERONET observations, which might arise from retrieval errors over a partially clouded scene. The assimilation procedure therefore includes a screening method to exclude these observations in order to avoid unrealistic results. A dust mask *screening method is designed, which is based on selecting only those observations where the deterministic model produces a substantial amount of dust. Experiment results show that this screen algorithm gives more accurate result compared to the traditional method based on background covariance in the case study. Note that our screen method would exclude valuable information in case the model is not able to simulate the dust plume shape correctly, hence applications in related studies requires inspections of simulations and observations by user.*

This chapter has been published in Jin et al. (2019):
Dust Emission Inversion Using Himawari-8 AODs Over East Asia: An Extreme Dust Event in May 2017.
Journal of Advances in Modeling Earth Systems, 11(2):446-467.

5.1. INTRODUCTION

The ground-based observations of aerosol optical depth (AOD) and particulate matter (PM) are of high importance for improving dust simulations. However, the limitations are also not negligible. For instance, the ground-based stations that observe visibility, PM_{10}, or AOD are often located only in the downwind and densely populated regions, which are far away from the source regions of dust in East Asia (the Mongolia and Gobi Deserts). Those instruments can only measure the dust levels when the plumes have already arrived in the downwind areas, hence they are of little help to the early dust forecasting and warning system. Besides, the model error due to the transport process usually grows with the distance that the plume travels. Even in case the dust emissions would be known accurately, the simulation error could be substantial by the time that the plume reaches an observation site. It will then be difficult to determine whether the observation-minus-simulation differences are due to the transport error or the emission deficiencies. Satellite instruments such as CALIPSO or MODIS are better capable of measuring the dust plume at its initial stage. However, CAPLISO has a narrow spatial coverage of about 5 km, and therefore only a limited observing coverage. The MODIS products provide a much larger spatial coverage, but only information on the total column and therefore no estimate of the plume height or thickness. The polar orbiting instruments also have a limited temporal coverage; for example the MODIS AQUA and TERRA platforms pass by only around 10:30 and 13:30 (local time).

Designed with the wide observing coverage and high temporal resolution, geostationary measuring instruments provide valuable information to track these short term and fast-changing airborne pollution events. Such as Seviri carried on board Meteosat Second Generation, from which the aerosol products have been used in dust storm detection (Ian and Richard, 2012) over North Africa and volcanic ash estimation (Fu et al., 2017) in Europe. The first of the next-generation geostationary Earth orbit meteorological satellites, Himawari-8 was launched in October 2014 by the Japan Meteorological Agency (JMA) (Bessho et al., 2016), and is pointed to East Asia. One of the instruments on the satellite is the Advanced Himawari Imager (AHI), which has significantly higher radiometric, spectral, and spatial resolution than those previously available in the geostationary orbit. The AHI has a multi-band imager with 16 spectral channels, covering a wavelength range from 0.46 to 13.3 μm. With a short observation interval of 10 min for the full disk and 2.5 min for specific target regions, Himawari-8 has the ability to track fast-changing phenomena, and thus provide useful data for assimilation into a dust storm model over East Asia. The Himawari-8 aerosol properties have already been used in the airborne aerosol data assimilation (Yumimoto et al., 2016), also in the dust data assimilation which shows the overwhelming strength compared to the MODIS satellite measurements (Sekiyama et al., 2016).

In this Chapter, we present the dust emission inversion using AOD observations from the Himawari-8 instrument. The geostationary satellite potentially covers both the dust source regions as well as the dust affected regions, with high spatial and temporal resolution. This opens the possibility that a dust storm is observed in an early stage already, and could therefore help to reduce the uncertainty in the emission estimate. The observations are assimilated into a dust simulation model based on the LOTOS-EUROS chemical transport model (CTM) using the reduced-tangent-linearization 4DVar tech-

nique. To ensure that the Himawari observations and model simulations are consistent with each other, special attention is paid to the observation selection. A dust masking technique that only selects observations where the model is able to simulate a dust load has been developed too.

LOTOS-EUROS simulation results for the tested extreme dust storm event over East Asia in May 2017 are presented in Chapter 5.2. In Chapter 5.3, the methodology of the reduced-tangent-linearization 4DVar is reviewed and the assimilation cycles are described. The Himawari-8 AODs used for data assimilation are described, and evaluated using the ground-based AOD observations from the AERONET network in Chapter 5.4. This subchapter also describes the ground-based observation network from the China Ministry of Environmental Protection (MEP) that is used to provide independent PM_{10} data to assess the dust simulations. In Chapter 5.5, both the *dust mask* observation screen method and a traditional measurement selection method are described and illustrated. Assimilation results are then shown, and evaluated by comparisons with the available AOD and PM_{10} observations in Chapter 5.6.

5.2. DUST STORM EVENT IN MAY 2017

In this Chapter, a dust storm event is investigated that occurred in May 2017. This dust event is reported to be the most severe one in the past 20 years. Fig. 5.1 (a), (b) and (c) show the LOTOS-EUROS simulation of AOD (550nm) at 13:00(CST) for May 3 to May 5. The model AOD map on May 3 shows that the severe dust plume stayed in Inner Mongolia, while a very small part was already transported to Central China. In the most severe dust plume, the maximum model AOD value was around 5 to 8. In the next 24 hours, the main plume was gradually blown along the southeast direction. The area affected by the dust storm is extended, while the maximum simulated column-integrated AOD lowers to a range from 2 to 5. On May 4 13:00, the dust plume covers almost all of North China, and a new dust plume started to develop in Inner Mongolia. In the third day, most of north China is free of extreme dust loads, and the main plume has been transported further to the south east, and even arrived at the Korean Peninsula. The dust aerosols deposited significantly while the plume moved to the east, and most of the simulated AOD values are lower than 2 at May 5, 13:00.

The reason why we use a new dust event (in May 2017) for the geostationary data based emission inversion is that Himawari-8 product is not available during the previous event in April 2015 yet.

5.3. EMISSION INVERSION SYSTEM

5.3.1. DATA ASSIMILATION METHODOLOGY

The assimilation system that will be used to combine Himawari-8 AOD observations with the dust simulations is based on a reduced-tangent-linearization (RTL) 4DVar that developed in Chapeter 3. Instead of only considering the errors from the friction velocity threshold (dust event in April 2015 in Chapter 3 and Chapter 4), the errors due to the wind field (friction velocity) are also taking into account when approximating the dust emission uncertainty of the event in May 2017. The uncertainty in the emission vector

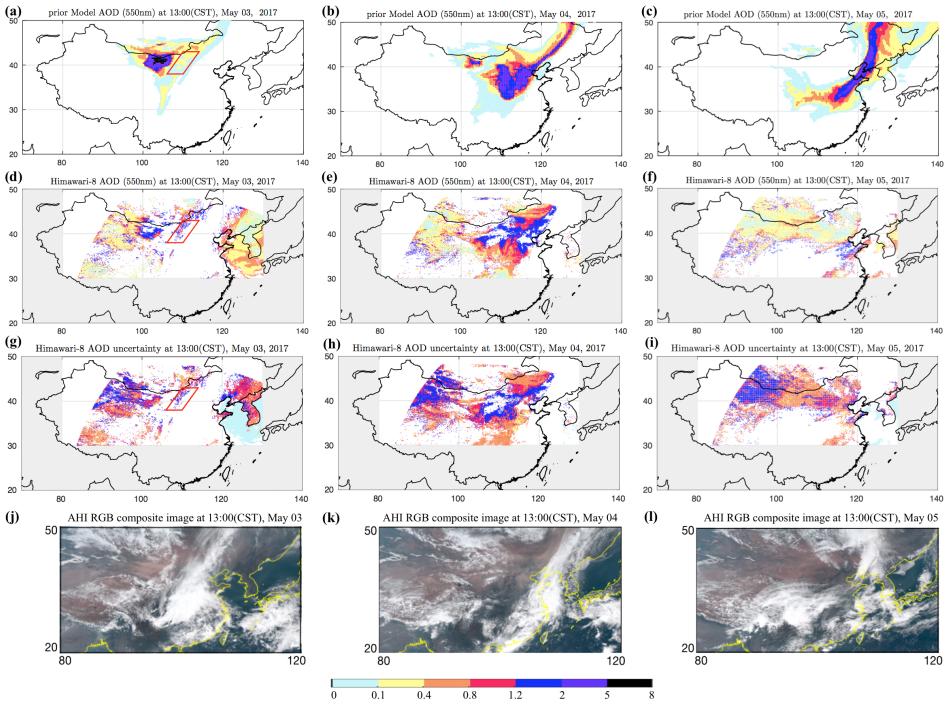

Figure 5.1: Simulations of AOD (550 nm) by LOTOS-EUROS model, as wells as Himawari-8 AOD (550nm), and AOD uncertainty, and AHI RGB composite image at 13:00(CST), May 3 to May 5: (a)(b)(c): Model AOD; (d)(e)(f) Himawari AOD; (g)(h)(i): Himawari AOD uncertainty; (j)(k)(l): AHI RGB image

$\delta \boldsymbol{f}$ is then:

$$\mathbf{B} = \mathbf{F}_{u_*} \mathbf{B}_{u_*} \mathbf{F}_{u_*}^T + \mathbf{F}_{u_{*t}} \mathbf{B}_{u_{*t}} \mathbf{F}_{u_{*t}}^T \tag{5.1}$$

The sum of the two contributions to the covariance of the emission deviation is already described in Chapter 2.2.

In this Chapter, the goal of the 4DVar technique is to find the maximum likelihood estimator of the dust emission field $\boldsymbol{f}$, given the available observations over an assimilation window. The incremental formulation aims to find the optimal emission deviation $\delta \boldsymbol{f}$ as the minimum of the cost function can be formulated as:

$$\mathcal{J}(\delta \boldsymbol{f}) = \frac{1}{2} \delta \boldsymbol{f} \, \mathbf{B}^{-1} \, \delta \boldsymbol{f} + \frac{1}{2} \sum_{i=1}^{k} \left(\mathbf{H}_i \mathbf{M}_i \delta \boldsymbol{f} + \boldsymbol{d}_i \right)^T \mathbf{R}_i^{-1} \left(\mathbf{H}_i \mathbf{M}_i \delta \boldsymbol{f} + \boldsymbol{d}_i \right) \tag{5.2}$$

where k is the number of time steps within the assimilation window for which observations are available. For an observation time i, the innovation vector (length m_i) is defined as the difference between the simulation and observations:

$$\boldsymbol{d}_i = \mathcal{H}_i(\mathcal{M}_i(\boldsymbol{f})) - \boldsymbol{y}_i \tag{5.3}$$

where $\mathcal{M}_i$ is the LOTOS-EUROS transport model, $\mathcal{H}_i$ is the operator that relates the observations to the model state, and $\boldsymbol{y}_i$ is the vector with observations for this time step. The operators $\mathbf{H}_i$ and $\mathbf{M}_i$ denote the linearizations of $\mathcal{H}_i$ and $\mathcal{M}_i$ around the prior state $\boldsymbol{f}_b$, respectively. In each outloop minimization process, the posterior state from the last iteration will be treated as the prior for the next iteration, where the linear operators $\mathbf{H}_i$ and $\mathbf{M}_i$, and the innovation vector $\boldsymbol{d}_i$ will be updated. The observation error term is weighted by the observation error covariance $\mathbf{R}$, for which the individual elements will be described in Chapter 5.4.1. The vector $\delta \boldsymbol{f}$ denotes a perturbation of the emissions with respect to the background state, and $\mathbf{B}$ is the covariance matrix of this perturbation as defined in Eq. 5.1.

One of the main efforts in using this formulation is the use of the a linearized model operator $\mathbf{M}_i$. This *tangent linear model* is often a separate model that needs to be maintained and updated next to the full model $\mathcal{M}_i$. To simplify the method, in this study a reduced-tangent-linearization 4DVar is used. The reduced-tangent-linearization 4DVar is based on a proper orthogonal decomposition (POD) of the background covariance $\mathbf{B}$ which efficiently carries out a model order reduction by identifying the few most energetic modes:

$$\begin{aligned} \mathbf{B} &= \mathbf{U}\mathbf{U}^T \approx \tilde{\mathbf{U}}\tilde{\mathbf{U}}^T \\ \delta \boldsymbol{f} &\approx \tilde{\mathbf{U}} \delta \boldsymbol{w} \end{aligned} \tag{5.4}$$

where $\mathbf{U} \in \mathbf{R}^{P \times P}$ is the background emission covariance transform, while $\tilde{\mathbf{U}} \in \mathbf{R}^{P \times p}$ is the truncation of $\mathbf{U}$ based on POD. The vector $\delta \boldsymbol{w} \in \mathbf{R}^p$ is the transformed vector, P denotes the emission field size of $O(10^4)$ and p is the reduced rank size. In this study, the size of the background covariance $\mathbf{B}$ is $O(10^4 \times 10^4)$. For this case, the computational cost of a *Cholesky* decomposition is still affordable. In case when $\mathbf{B}$ has a much larger dimension, the principle patterns of the emission vector can also be computed using an *Arnoldi* iteration method (Arnoldi, 1951).

With the truncated transform of $\mathbf{B}$, the cost function of the reduced-tangent-linearization 4DVar is formulated as:

$$\mathcal{J}(\delta \boldsymbol{w}) = \frac{1}{2}\delta \boldsymbol{w}^T \delta \boldsymbol{w} + \frac{1}{2}\sum_{i=1}^{k}\left(\mathbf{H}_i \tilde{\mathbf{M}}_i \tilde{\mathbf{U}} \delta \boldsymbol{w} + d_i\right)^T \mathbf{R}_i^{-1}\left(\mathbf{H}_i \tilde{\mathbf{M}}_i \tilde{\mathbf{U}} \delta \boldsymbol{w} + d_i\right) \tag{5.5}$$

where $\tilde{\mathbf{M}}_i$ denotes the reduced tangent linear model with a rank p, which is approximated using the perturbation method. Similar to the traditional incremental 4DVar, posterior control variable vector $\delta \boldsymbol{w}$ from the last outer loop iteration will be used as the prior for the next iteration in the minimization process, where both the linear model operator $\tilde{\mathbf{M}}_i$ and innovation $\boldsymbol{d}_i$ are updated. In this study, the reduced rank size p is set as 40. A larger reduced rank $p > 40$ is also tested, but the improvement is negligible. By projecting the original parameter field into a subspace of a few leading patterns, the reduced-tangent-linearization 4DVar significantly decreases the computation time for deriving the linear model operator. However, as it only explores the optimal parameters in a reduced subspace, inevitably some properties of the original dynamic system will be lost.

5

5.3.2. ASSIMILATION WINDOW

Fig. 5.2 shows the assimilation window settings for the test event. The dust simulation is configured with a period from 15:00, May 02 to 06:00, May 06. The dust outbreak events are fully covered by the assimilation windows, hence the model is assumed to be free of dust at the starting moment. It forwards with default emission field $\boldsymbol{f_b}$ and provides early dust forecast for the whole period if no data assimilation analysis is performed. The first assimilation cycle is set from the start to 15:00 May 03, with a length of 24 hours, while the available observations from 09:00 to 15:00 May 03 are used in the reduced-tangent-linearization 4DVar. Then our model propagates from the start again with the newly estimated emission vector $\boldsymbol{f_a}$, resulting in the posterior simulation in the first cycle as well as the dust forecast after 15:00, May 03. In fact, parts of AOD observations in the following time are also attributed to the dust emission in the first assimilation window, hence an extended window, e.g., 48 hours, will enrich the data to estimate these emissions. However, to provide the in-time dust forecast like in case of an operational system, our assimilation starts once the observations during a full day (09:00 ~15:00) are obtained.

The second cycle is designed with the same length, and the posterior emission field is used to provide the dust forecast after 15:00, May 04. After the end of the second cycle, dust emission is negligible and won't be carried into downstream, thus, a third assimilation cycle is not implemented.

With the settings of the assimilation window, we are able to evaluate whether the assimilation algorithm helps to improve the dust early forecasting in practical applications.

5.4. DATA FOR ASSIMILATION AND VALIDATION

5.4.1. HIMAWARI-8 AEROSOL OPTICAL DEPTH (AOD)

The Japan Aerospace Exploration Agency (JAXA) have developed a Himawari-8 aerosol retrieval algorithm (Fukuda et al., 2013, Ishida and Nakajima, 2009, Yoshida et al., 2018).

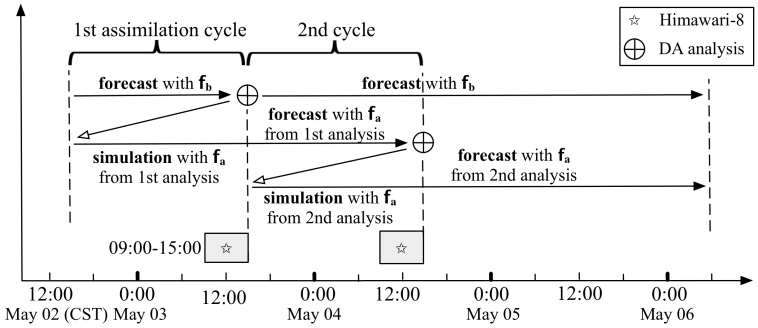

Figure 5.2: Timeline of observation availability, assimilation windows and forecasts

Cloud/clear discrimination is performed. The Aerosol Optical Depth (AOD) at 500nm and the Ångström exponent (AE) are derived from the visible channels (470, 510, and 640μm) over land areas, and from both the visible (640 μm) and near-infrared data (860 μm) over ocean regions. The JAXA retrievals provide Himawari-8 AOD Level 2 at 10 minute intervals with a resolution 0.05°× 0.05°. In this study, the JAXA Himawari-8 Level 2 AOD will be assimilated with the dust simulations using the reduced-tangent-linearization 4DVar to identify and track the rapid-changing dust storm events.

AOD at the wavelength 550nm are more widely used to evaluate the aerosol column-integrated concentration, the original Himawari-8 Level 2 products (500nm) are extrapolated using (Cesnulyte et al., 2014):

$$\mathrm{AOD}_{550} = \mathrm{AOD}_{500} \cdot \left(\frac{550}{500}\right)^{-\alpha} \tag{5.6}$$

where α represent the Ångström exponent which is also from the Himawari-8 aerosol property product. Fig. 5.1(d),(e) and (f) show three snapshots of the AOD (550nm) map. For better interpretation, also the RGB composite images from the Advanced Himawari Imager (AHI) are shown in Fig. 5.1(j), (k) and (l). In general, the three plume maps show a large similarity to the prior LOTOS-EUROS AOD simulation as shown in Fig. 5.1(a),(b) and (c). Note that the Himawari-8 AOD observations do not exceed a value of 2, while the prior model simulated AOD shown in Fig. 5.1(a) exceeds this value significantly.

As shown in Fig. 5.1(d), at May 3 the main part of the dust plume stayed in the boundary region between Mongolia and North China, which is believed to be the source region. The adding value of the Himawari-8 AOD product over ground based observations is clearly visible for that day; while the dust plume was already observed by the satellite in detail at this early stage, the first ground-based sites that observed the plume are located far away from the source region. For instance, the upstream four sites (Wuhai, Bayanzhuoer, Hohhot and Baotou) did not measure severe PM_{10} concentration until 4 to 8 hours later (see Chapter 5.6.3 and Fig. 5.12. The early observations of the dust plume could therefore be of great benefit for a timely forecast of dust storms. Note that only a few AODs are available in the Central China for that day. As shown in the RGB composite in Fig. 5.1(j), this region is covered by clouds which hampers retrievals of total

AOD columns. The AOD fields retrieved by Himawari have rather high values in an area next to the cloud covered region, which is marked by a red frame in Fig. 5.1(d). However, the model simulations did not show high AOD values in this area, and therefore the high values in the observations might also arise from retrieval errors over a partially clouded scene. The difference between observations and simulations in this region will be discussed further in Chapter 5.5 on observation selection.

During the next 24 hours, the severe dust plume were moved southeastwards. Fig. 5.1(e) shows that there was a band with severe dust loads from the Central China to Northeast China around May 04 13:00 CST. As shown in Fig. 5.1(k), the central region of this band is free of cloud, but AOD retrievals there are not available for unknown reasons. A new plume with high dust loads is also present in the Inner Mongolia province. On May 5, the plume was transported further in southeast direction as shown in Fig. 5.1(f), and even affected the Korean Peninsula. AOD retrievals over Northeast China are not available on this day, while the model still simulates a band with high dust loads.

Fig. 5.1(g), (h) and (i) represent the AOD uncertainty from the same JAXA Himawari product. The AOD uncertainties over lands stay at a high level similar to the AODs from SEVIRI on board a geostationary satellite (Carrer et al., 2010), but much larger than the MODIS AODs from polar orbit satellites (Remer et al., 2005). Zhang et al. (2019) indicated they are due to the large uncertainties in the aerosol models and surface reflectance estimation in the retrieval algorithm. In fact, Level 3 with more certain measurements are also available, however, only few AODs survive during the further retrieval hence not used in this work. To make the observation resolution consistent with the model, the Himawari AODs (550nm) as well as the uncertainty are coarsened. The coarsened AODs and uncertainty are taken as the average over the 0.25°× 0.25°model grid cell. The coarsened data can be seen in Fig. 5.7.

The square of coarsened uncertainty are set as the diagonals of the observation covariance matrix **R**. Although the relative uncertainties of the Himawari AODs are higher than the emission uncertainties in Fig. 2.3 with respect to the prior emission in Fig. 5.8, the huge number, $O(10^4 - 10^6)$, due to a fine resolution and a wide coverage still makes the observation error term dominant in the cost function J. In addition, a spatial correlation of the coarse AODs is assumed while building the error matrix **R**,

$$s(i, j) = e^{-a \cdot h(i,j)} \tag{5.7}$$

where $s(i, j)$ and $h(i, j)$ represent the correlation coefficient and distance between model cell i and j respectively, while $a = 0.03$ km^{-1} is an empirical value based on a statistical analysis of the original Himawari AODs. Note that experiments were also conducted using a diagonal observation error covariance, thus neglecting the spatial correlations in the observation errors. Those assimilation runs resulted in similar results (not included in this paper) to the experiments shown here. This is because that our simulation is spatially smooth and does not contain strong local variability, the impact of observation spatial correlation is then very weak.

5.4.2. HIMAWARI-8 AOD VERSUS AERONET

Before assimilating the new Himawari-8 AOD, the product is first evaluated through a comparison to ground based observations from the AErosol RObotic NETwork (AERONET).

At the sites of this network, AOD total columns are measured by ground sun photometers. In the dust-affected region, four AERONET stations are available, marked as A1 to A4 in Fig. 5.5: Baotou, Beijing, Beijing CAMS, and Xianghe. Fig. 5.3 shows the time series of AERONET AOD at these four sites (red marks), either from the Level 1.5 product (cloud-screened and quality controlled), or otherwise Level 2.0 (quality-assured). Himawari-8 Level 2 AODs at 500nm are also shown, as average over the 0.25°× 0.25°model grid cell in which the site is located; for each 10 minute observation time, the blue mark is the grid cell mean and the gray error bar represents the observation error which is the mean of Himawari AOD uncertainties within the grid cell. As can be seen in the time series, the spread in the Himawari observations is large, but in general the mean values are rather stable. Though the Himawari AODs did not match the AERONET measurements all the time, all the AERONET AODs are within the spread of observation error.

On May 4, high AODs values are observed by AERONET as well as Himawari in all four sites. For the Beijing CAMS station, no observations are available at these moments, but it is supposed to give similar measurements with Beijing and XiangHe due to the small distance. The Himawari AOD observations match well with the AERONET observations during the event. On May 5, the Himawari and AERONET stations Baotou and Beijing CAMS all observe low AOD values, which indicated the dust storm already expired at that time.

For further comparison, the scatter diagrams of the AODs at the above 4 sites during the dust storm form May 03 to May 06 are plotted in Fig. 5.4. The comparison results in a high correlation coefficient (R^2 = 0.9762). As can be seen in the maps before, the Himawari AOD values do not exceed a value of 2; with high dust loads, the AERONET observations reach values in a range of 0.0-2.5. Although this limited comparison is not a guarantee for a high quality of Himawari-8 AODs over the whole model domain in the dust event, the agreement is sufficient to have confidence that this new data set represents the dust plume optical properties.

5.4.3. MAP OF THE FIELD STATION OBSERVATIONS

As mentioned in Chapter 1.4.1, a network of over 1,500 field stations all over China has been established to monitor the atmospheric constituents including $PM_{2.5}$, PM_{10}, CO, O_3 and SO_2. Most of these ground stations are located in the densely populated regions in eastern China, and are rather far away from the dust source region in Inner Mongolia, see Fig. 5.5. Compared to the Himawari-8 AODs, these could not provide information on the dust storm from the very start. However, hourly averaged PM_{10} observations from the network could be used as independent data, to verify the improvement of the dust simulation in the areas where the interest in accurate forecast is the highest.

Though all these Himawari-8, AERONET AODs and the ground PM_{10} data are actually a sum of the dust aerosols and particles released in local activities, the 2017 dust storm is an extremely severe one hence dust aerosols are very dominant in the full aerosols. Therefore, all these measurements are assumed to be consistent to the dust simulations. Observational bias corrections (Dee and Uppala, 2009) or non-dust baseline removals, e.g., in Chapter 4, would be required in case of less severe dust storms.

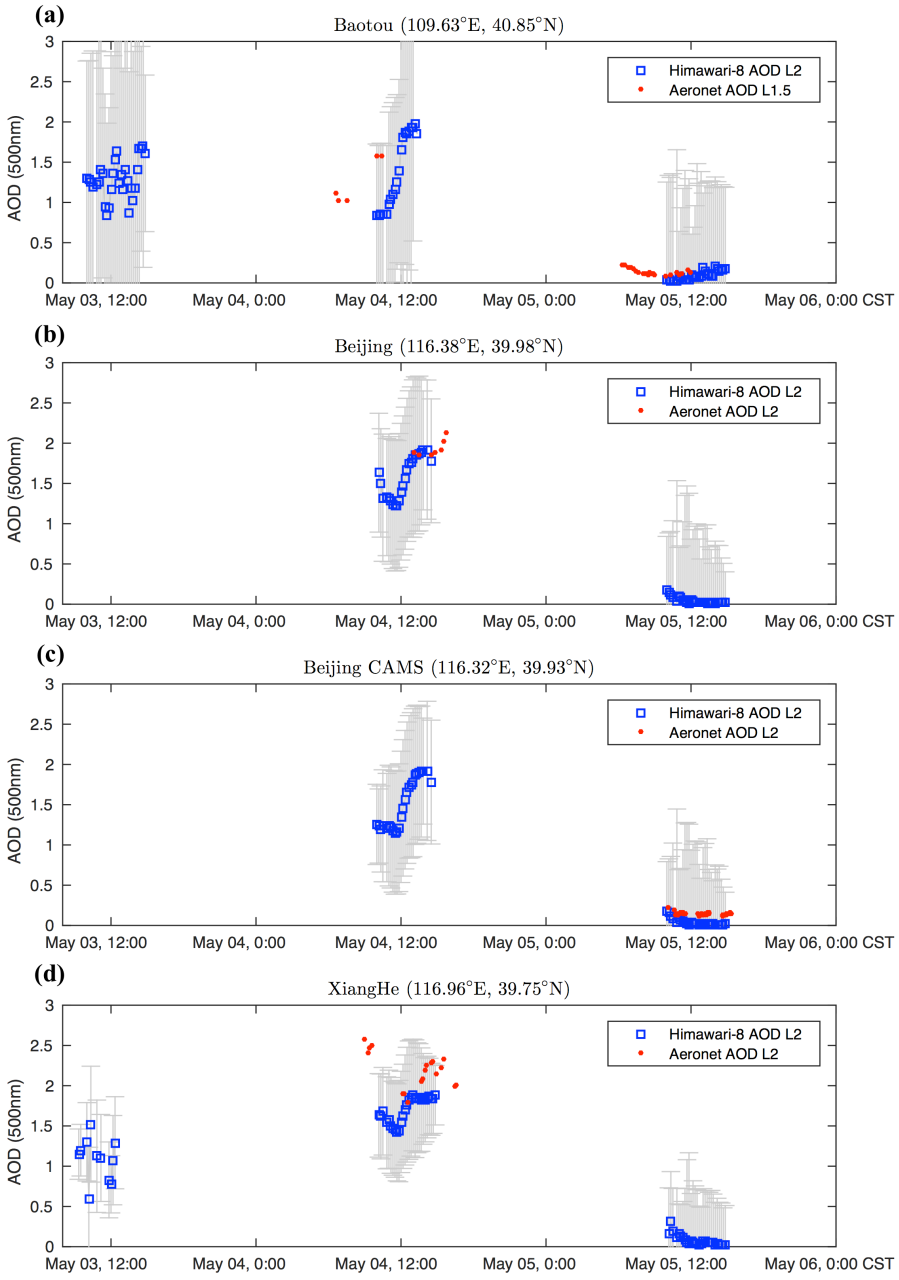

Figure 5.3: Time series of AOD at or around AERONET sites: AERONET AOD observations (level 1.5 or 2), Himawari-8 AOD retrievals with the gray bar representing the observation error (mean of uncertainties within the grid cell) around the AERONET sites.

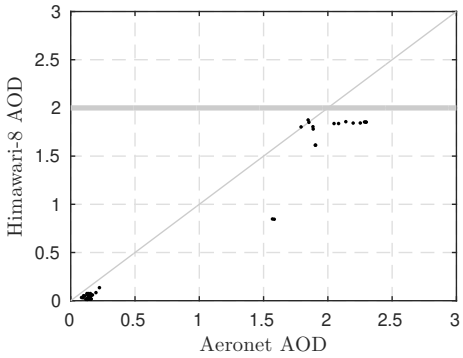

Figure 5.4: Scatter diagrams of Himawari-8 AOD compared to AERONET AODs at Baotou, Beijing, Beijing CAMS, and XiangHe from May 03 to May 05

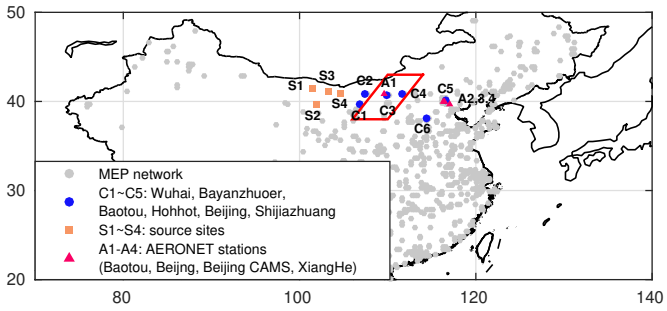

Figure 5.5: The China MEP network of field measurement stations, AERONET stations, and source region sites.

5.5. OBSERVATION SELECTION FOR DATA ASSIMILATION

The data assimilation system is designed to deal with imperfect model simulations and uncertain observations. For our case, it aims to find the optimum dust emission field that ensures the best match between simulations and Himawari-8 AOD observations. Fundamentally, it relies on the assumptions of an unbiased model and measurements with a Gaussian probability distribution. In practice, the discrepancy between the simulations and the observations can be strongly biased however, for example because model errors in deposition and transport are not taken into account. Also, sometimes the AOD retrievals might be strongly biased, for example due to failed retrievals under the presence of clouds. Such inconsistency will inevitably lead to analysis errors or model divergence.

To limit the negative effects of inconsistency between observations and simulations, algorithms for data selection have been developed and implemented in data assimilation systems (Anderson and Järvinen, 1999, Sakov and Sandery, 2017). The general idea of the observation selection is to exclude measurements that cannot be represented well by the background model simulation. The actually assimilated observations are then a

subset of the original data. The reason why certain observations are excluded should be monitored through the assimilation process, and ideally the assimilation system should be adjusted to allow inclusion of these observations in the future.

5.5.1. INCONSISTENCE BETWEEN THE DUST MODEL AND HIMAWARI-8 AOD

Although Fig. 5.1 showed many similarities between the prior LOTOS-EUROS model simulation and the Himawari-8 AOD observations during the dust episode, some significant differences were also found. For instance, at May 3 the Himawari-8 AOD showed high values around the border between Mongolia and Inner Mongolia at 13:00(CST), marked by the red frame in Fig. 5.1(d). However, the model simulated only a small amount of dust there, resulting in modest AOD values. To analyze this discrepancy, the time series of AOD and surface dust concentration in Baotou (located in the highlighted red framework) is shown in Fig. 5.6. The reason to select Baotou is the availability of both Himawari-8 and AERONET AOD observations, as well as a PM_{10} observing site.

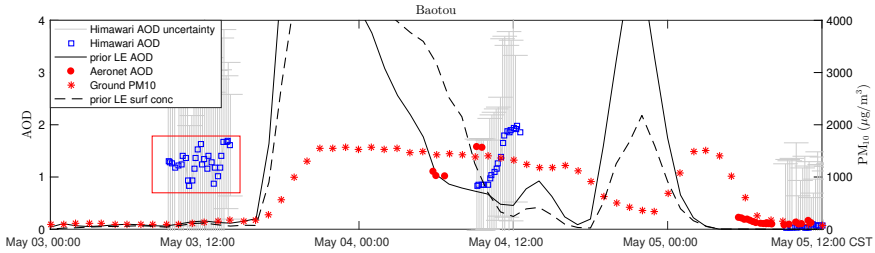

Figure 5.6: Time series of observed (Himawari-8 and AERONET) AOD and simulated AOD (left axis), as well as the observed and simulated surface PM_{10} concentrations in Baotou (right axis)

Fig. 5.6 shows that the surface PM_{10} observations are low until the arrival of the dust plume around 16:00. The model simulations show the same pattern, but the computed surface dust concentrations are much higher than the actually observed PM_{10} concentrations. The Himawari-8 AOD shows there are already quite high AOD values around noon. An explanation could be that the dust cloud is initially elevated from the surface, and therefore not observed by the PM_{10} network. However, there are no AERONET observations to confirm the heavy dust in the higher vertical layer, which might be an indication that the sky was actually partially clouded as suggested by the RGB composite in Fig. 5.1(j). Actually, it is difficult to distinguish between clouds and thick dust especially in those regions where the temporal variations of dust AOD are large, since the Himawari-8 product also uses the temporal variation of observed radiance for the cloud identifications.

The time series in Baotou show that in this location, for the current model configuration, the simulated surface PM_{10} is strongly correlated with the simulated AOD. Assimilation of the high valued Himawari AOD observations at May 3 would therefore lead to an increase of simulated surface PM_{10}, which is not consistent with the surface observations. Since the high AOD values retrieved from Himawari could not be confirmed by AERONET observations, and might have been caused by a partially clouded scene, it

would be better to have these observations excluded from the assimilation. The algorithms of automatic exclusion of these observations, or selection of observations to be used in the assimilation, will be described in Chapter 5.5.2 and Chapter 5.5.3, respectively.

5.5.2. BACKGROUND CHECK

A popular data selection algorithm is the *background check* (BC) (Anderson and Järvinen, 1999, Dee et al., 2011). This selects only those observations for which the difference from the background simulation is within a range relative to the uncertainty of the difference:

$$\left(y - \mathcal{H}(\mathcal{M}(\boldsymbol{f})) \right)^2 \leq \kappa \, (\sigma_b^2 + \sigma_o^2) \tag{5.8}$$

where the left hand side represents the square of difference between an observation and the corresponding simulation value by the background model. Under the assumption of this being unbiased, the expected stochastic distribution has zero mean and the variance shown in parentheses at the right hand side, where σ_b and σ_o are the standard deviations on the diagonals of covariance matrices $\mathbf{B}$ in the observation space and $\mathbf{R}$ respectively. The factor κ is a predefined threshold, a larger κ allows more observations to survive the selection. (Anderson and Järvinen, 1999) associated quality flags with different values of the threshold, where $\kappa = 0$ selects only *correct* data, $\kappa = 1$ selects *probably correct* data, $\kappa = 2$ also selects *probably incorrect* data, and $\kappa = 3$ even selects *incorrect* data.

Fig. 5.7(a) shows the coarse AOD from the Himawari data at May 03 13:00, there are lots of measurements available in the source region, also inside the highlight red frame. Fig. 5.7(b) and (c) present the selected Himawari-8 AOD using $\kappa = 1$ and $\kappa = 2$ at the same time snapshot. On May 3, when using a strong selection $\kappa = 1$, many AOD observations are excluded, for example parts of the observations in the red, but also many observations in the source regions. Thus, the valuable observations that show the development of the dust storm at an early stage are excluded too. With a more relaxed selection using $\kappa = 2$, more AOD observations in the source region remained but still a lot of them are discarded. Definitely, more AODs in the source region will be kept if a more relaxed *background check* $\kappa > 2$ is applied, the selection AODs of which are closer to the original observations. On the other hand, observations in the red frame which should have been excluded now remained under these two selections $\kappa = 1$ and $\kappa = 2$. The main reason why these observations are selected by the *background check* is the rather large observation uncertainty, which can be seen in Baotou in Fig. 5.6. On May 03, the innovations $y - \mathcal{H}(\mathcal{M}(\boldsymbol{f})$ are all within the observations' spread of its uncertainty. More restricted selection is then required in order to exclude those unexpected measurements inside marked frame. It is therefore difficult to tune the observation selection properly using this method.

5.5.3. DUST MASK SELECTION

To have a proper observation selection for the studied application, the *dust mask* (DM) method is introduced here. The dust mask criterion selects only those observations in the grid cells where the deterministic model simulation exceeds a certain threshold:

$$\mathcal{H}(\mathcal{M}(\boldsymbol{f})) \geq s \tag{5.9}$$

The user defined threshold s denotes a certain dust level over which the grid cell is considered to be affected by the dust storm. The identification of the dust masked region is only based on the initial simulation of the dust model and s, and independent of the observation uncertainty. This selection works efficiently in cases where the model is able to reproduce a correct dust plume shape, but is not able to simulate the correct amplitude of dust concentrations. The observations are only selected over this dust masked region where the model simulated an amount of dust over this level. In other regions, high AOD values reported by Himawari are excluded, which are due to cloud/dust misdiscrimination, or local emissions that are not included in this simulation model. This selection also removes the modest Himawari AODs where the model also produces a low dust level. However, as those measurements are already in good agreements with the model simulations, the exclusion of these data has only minor impacts on the assimilation results.

A limitation of the *dust mask* selection is that it could exclude valuable observations in case the model is not able to simulate the dust plume shape correctly. In that case, the model could simulate a modest dust level ($< s$), and hence remove the high AOD values as if they are due to the AOD retrieval error while they actually represent the severe dust. Whether a *dust mask* selection is necessary is therefore case-dependent, and requires inspections of the simulations and AOD observations by the user.

The empirical threshold s is adjustable in practice; if the size of the dust-affected plume is overestimated, a large threshold should be adopted, otherwise, s should be lowered. In our case, we evaluated the impact of the *dust mask* threshold by using either $s = 0.1$ or $s = 0.4$, which corresponds to about 5% and 20% of the maximum Himawari AOD value.

Fig. 5.7(d) and (e) present the Himawari-8 AOD observations selected by the dust mask criterion, for two different thresholds $s = 0.4$ and $s = 0.1$. When using a high DM threshold $s = 0.4$, the dust-affected region is located exactly in the source region, observations outside are all excluded. With a lower threshold $s = 0.1$, a larger dust-affected region is identified, observations near the source region are also selected. Moreover, all observations inside the highlighted red frame are excluded with $s = 0.4$ since the background model shows that the dust level there is very low (< 0.4), and a small portion of these data are kept in case a lower threshold $s = 0.1$ is set.

5.6. ASSIMILATION RESULT AND DISCUSSION

5.6.1. EMISSION ANALYSIS

Using the above described configurations, the Himawari-8 AOD observations have been assimilated for the dust storm event to estimate the dust emission field $\boldsymbol{f}$. Different assimilation runs were performed, either using all observations, or using a subset of AODs selected by the *background check* (BC) or *dust mask* (DM).

Fig. 5.8(a)~(f) show the map of prior, several posterior emission integration index F (the definition can be found in Chapter 2.2.3) over the potential source region during the period of the two assimilation windows. The prior model simulated the highest emission

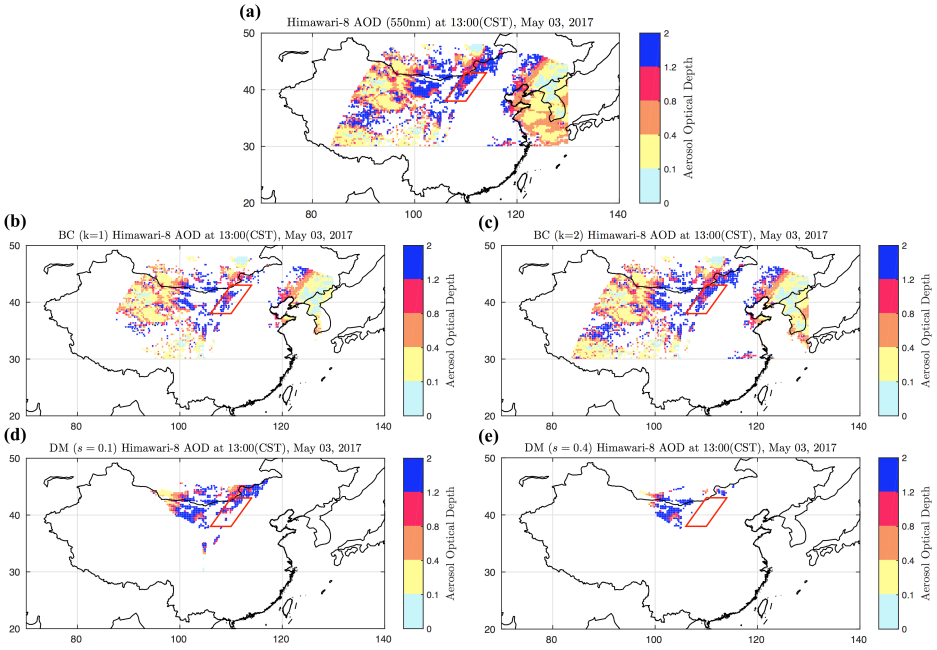

Figure 5.7: The results of Himawari-8 AOD observations selected for assimilation by the *background check* (BC) and dust mask (DM) criterion at 13:00, May 03: (a): no selection; (b) and (c): BC with $\kappa = 1$ and $\kappa = 2$; (d) and (e): DM with $s = 0.1$ and $s = 0.4$

integration, especially in the boundary region between China and Mongolia. In a large number of grid cells, the accumulated dust emissions are in the range from 120 to 200 g/m^2, which resulted in the overestimation of the AODs in dust plume center as can be seen in Fig. 5.1(a). The assimilation of all available Himawari AODs and DM selected AODs generally computed a lower level of dust emission, there are only a few grid cells with the integrated emission exceeding 120 g/m^2.

As mentioned in Chapter 5.5.2, many of the AOD observations in the source region are excluded while using the BC selection, because they exceed the uncertainty spread of simulation-observation difference in Eq.(14). Although the estimated emissions also decreased a bit, the emission flux F still stayed at a much higher level than posterior emissions by assimilating raw AODs and DM screened AODs.

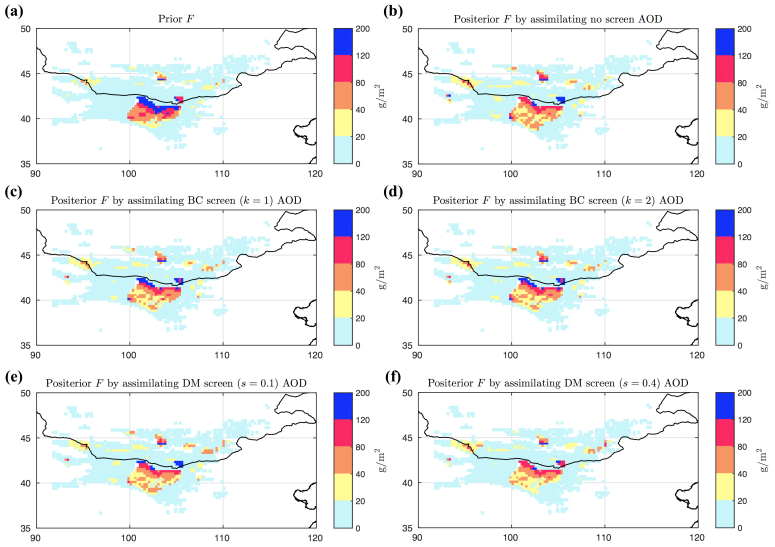

Figure 5.8: The posterior emission integration index F after the first analysis (15:00 May 03) using the no screen Himawari-8 (a); BC $k = 1$ (b), $k = 2$ (c) and DM $s = 1$ (d), $s = 2$ (e) screening methods

5.6.2. AOD ANALYSIS

In each experiment, the LOTOS-EUROS model is used to simulate the dust load using the optimized dust emissions, and both column-integrated AOD as well as surface PM_{10} are evaluated with observations.

Fig. 5.9(a)~(e) show the snapshots of AODs over the domain for each of the 3 days of the events, either using all observations or parts of AODs from a selection. The prior model AODs at these three corresponding moments are plotted in Fig. 5.1(a),(b) and (c), while the original Himawari-8 AODs are shown in Fig. 5.1(d),(e) and (f). The simulated AOD values show in general the same patterns as the observations for all experiments, but differences are present at regional scale. Compared to the background simulation, in which the model AODs are significantly overestimated at the center of the dust plume, all the posterior AODs decreased after assimilation, but different assimilation runs also

resulted in different increments.

The effect of the different observation selection criteria is best seen on May 3 for the area marked by the red frame. If no selection is applied and all observations are used in the assimilation, emissions are elevated to a level which is able to produce high simulated AOD values in the red marked region. When a *background check* selection is applied (Fig. 5.9(b)~(c)), the simulated AODs are lower in the marked area as parts of the high-value AODs are excluded. However, since this *background check* also excluded observations over the source region, the assimilation is less effective to change the dust emissions here and the simulated AOD remains rather high (values above 5). This effect is less strong when a more relaxed selection ($\kappa = 2$) is performed, which also leads to higher AOD values in the marked area. When the *dust mask* criteria is used (Fig. 5.9(d)~(e)), the simulated AODs in the marked area remain low and are better than the results obtained using the *background check*. In addition, the simulated high AOD values in the source region are also tuned to a low level which are in better agreement with the observations. In similar cases, the predefined *dust mask* threshold s is recommended to be set from 5% to 20% of the maximum AOD value, a too high threshold will exclude most observations while a too low value makes the observation selection less effective.

To illustrate the differences in the posterior AOD performance for the different selection criteria, Fig. 5.10 shows the time series of AOD at four locations in the source region (S1~S4 in Fig. 5.5) during the evolution of the dust storm on May 3. The strong dust emissions occurred on this day in this region, and the Himawari-8 observations are also available. In S1 and S2, the prior model already produced an AOD simulation that is close to the Himawari-8 AOD; however, the model strongly overestimated the AODs in S3 and S4. This suggests that the existing emission parametrization is in principle able to simulate dust loads, but at local scale the error might still be large. Assimilation using all available observations (no selection) strongly improves the simulation, and the best results are obtained using the *dust mask* selection criteria. Selection based on *background check* leads to simulations with still much too high AOD, since many of the AOD observations in the source region are actually not selected for assimilation.

The impact of the different observation selection on the AOD simulation can also be observed on May 4 in Fig. 5.9(a.2)~(e.2). If no selections are performed, the simulated AOD values are still a bit overestimated in the plume center, also the size of dust-affected region (AOD > 0.1) are extended compared to the background simulation. When the *background check* is implemented, the dust-affected region is limited because parts of the inconsistent data are excluded. However, the simulated AOD is still significantly overestimated in the plume center due to the exclusion of the AOD observations in the source region in the first cycle. In the cases when *dust mask* selection is applied, the size of the dust plume is not much extended especially when a restricted selection $s = 0.4$ is used, and the AOD simulation overestimation is mitigated.

On May 05, differences in the of simulated AODs using the two observation selections still existed, but were not so strong.

5.6.3. COMPARISON WITH SURFACE PM_{10}

In order to further evaluate the posterior simulations, the simulations of PM_{10} are now compared with observations from the surface network described in Chapter 5.4.3. Since

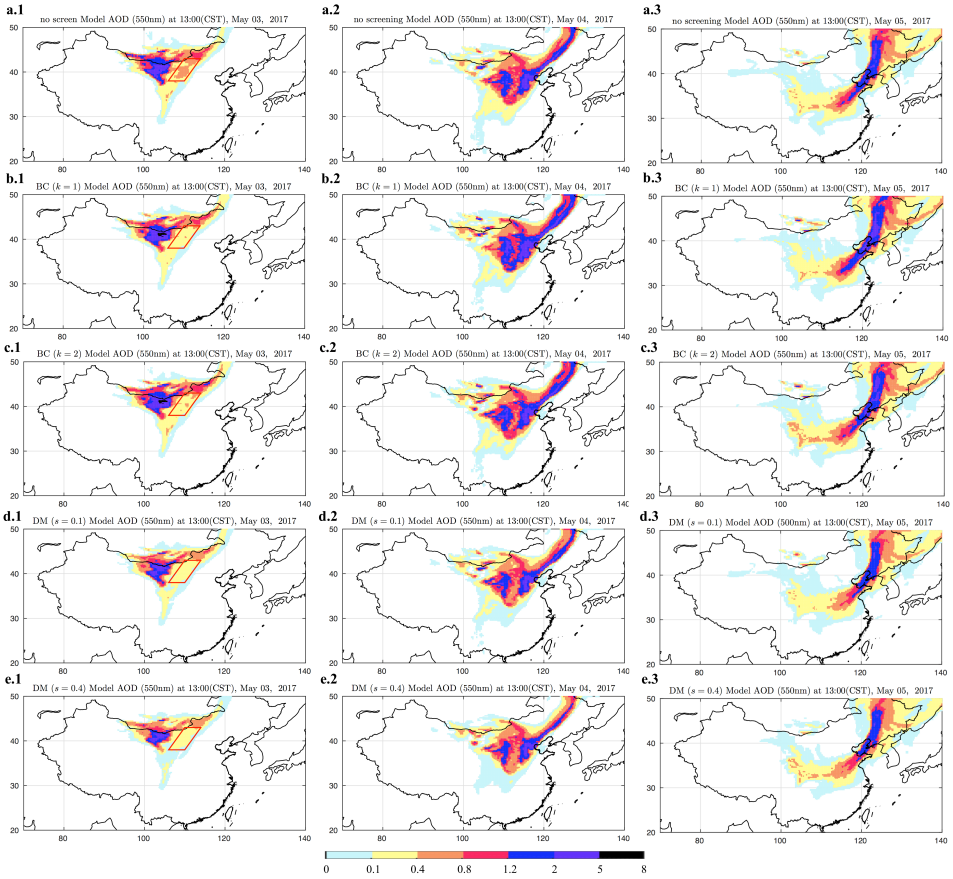

Figure 5.9: Posterior AOD map using no screen Himawari-8 (a.1~a.3), BC $k = 1$ (b.1~b.3), $k = 2$ (c.1~c.3) and DM $s = 1$(d.1~d.3), $s = 2$ (e.1~e.3) screening methods at three time snapshots: 13:00(CST), May 03 (a.1, b.1, c.1, d.1, e.1), May 04 (a.2, b.2, c.2, d.2, e.2), May 05 (a.3, b.3, c.3, d.3, e.3). Note: the prior model AOD and the Himawari-8 AOD are shown in Fig. 5.1

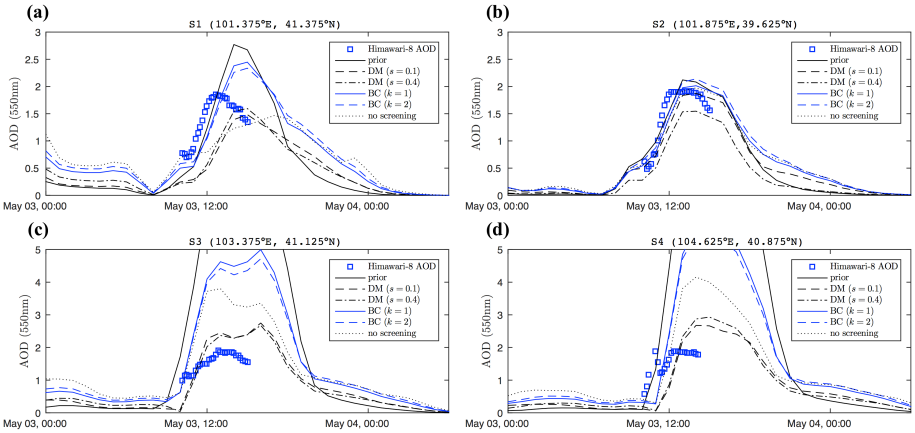

Figure 5.10: Time series of AOD in 4 sites in the source region site on May 03, (Himawari observations averaged over the 0.25 × 0.25 model grid)

5

these observations were not assimilated, this assessment will show the added value of assimilation the Himawari AOD for surface PM_{10} concentrations.

It should be noted that the PM_{10} observations represent not only the dust aerosols, but also particulate matters from local anthropogenic activities. In most cities, the PM_{10} values are in a range of 10-200 $\mu g/m^3$ during the non-dust period. During a dust event, however, the maximum PM_{10} concentrations easily reach several thousands $\mu g/m^3$. Therefore, in this Chapter the PM_{10} observations are compared directly with the simulated total dust concentrations, neglecting that a small part of the observations is actually non-dust, and without using any non-dust aerosol correction. Besides, we only used the PM_{10} from the 200 sites in the North China which reported this severe dust phenomena instead of assimilating all measurements, since some sites in the South China were free of the dust during the episode.

Fig. 5.11(a)~(e) show the three time snapshots of surface PM_{10}, either from the observation network, or from the background simulation, or from the posterior simulations using different AOD selection. These three snapshots show the whole process of the dust transport. On May 3 13:00(CST), the first high surface PM_{10} concentrations are observed around the Mongolia and Gobi Deserts. The plume then moves to the Central and Northeast China and leads to significantly increased concentrations in the morning of May 4 7:00, and severe dust plume is further carried southeastwards and the surface dust concentrations stayed at a very high level in the following 6 hours. In the time followed, the surface dust concentrations start to decrease gradually, and are much weaker compared to the ones at May 04, 07:00 and 13:00, and are not shown here.

Fig. 5.11(a.1) shows that most of the surface sites are free of extreme dust loads on May 3 13:00 (CST), and the PM_{10}s are below 200 $\mu g/m^3$ (first row). Fig. 5.11(c.1) shows the map with the posterior dust concentrations obtained by assimilating all Himawari-

8 AOD (third row). Unlike the observed PM_{10} map, it shows that there are also non-negligible dust concentrations of about 200 to 500 $\mu g/m^3$, especially inside the red frame. Similarly, the assimilation of the *background check* selected observations (fourth row) also shows high level dust concentrations in the marked area since the *background check* selection did not exclude the high AOD values there. In the contrary, both the prior concentrations (second row) and the assimilations using *dust mask* observation selection (fifth row) do not show high PM loads in this region. This shows that assimilation of certain observations introduces unrealistic dust concentrations at the surface.

Fig. 5.11(a.2)~(a.3) show the surface PM_{10} concentrations at the other two snapshots on May 4 7:00 and 13:00. Severe dust concentrations are reported by stations all over North China, with a few values up to 2000 $\mu g/m^3$, and most ones stay in a range of 500 to 2000 $\mu g/m^3$. The second row shows the corresponding background simulations. Similar to the AOD, the background simulation also overestimated the PM_{10}, and at many locations the simulated concentrations exceed 2000 $\mu g/m^3$. The assimilation of Himawari AOD (third to fifth row) lower the concentrations, where the best result is seen when *dust mask* selection is used. When the *dust mask* selection is performed, the estimated surface concentrations are now in a range of 500 to 2000 $\mu g/m^3$, which is in agreement with the observations.

To further analyze the performance in simulations of surface concentrations, the time series of surface dust concentration in 6 sites, as well as the ground PM_{10} measurements are shown in Fig. 5.12. The locations of these 6 sites can be found in Fig. 5.5.

The PM_{10} observations indicate that the dust storm arrived in Wuhai and Bayanzhuoer on May 3 around 14:00, and in Hohhot and Baotou around 19:00. The time series of the prior simulation follow this pattern, although the simulated values are 2 to 3 times higher than the observed.

After assimilation of Himawari-8 AODs, the posterior concentrations are strongly improved in Wuhai, Hohhot and Baotou, as shown in Fig. 5.12(a),(c) and (d). Best results are obtained when the *dust mask* selection is applied. The assimilation does not improve concentrations in Bayanzhuoer as shown in Fig. 5.12(b); the observations there reach values as high as 4000 $\mu g/m^3$, while the maximum simulated concentrations after assimilation are around 1500 $\mu g/m^3$.

Assimilation of all available data or using the BC selection criteria could introduce a small inconsistency in the surface concentrations in the early morning of May 3, as indicated by the red boxes in Fig. 5.12(a)~(d). In some assimilations an extra peak in the dust concentrations is incurred, with a maximum around 200 to 500 $\mu g/m^3$. This peak was caused by the assimilation of AOD observations that cannot be represented correctly by the model, it still exists in the assimilation when *background check* is performed, but can be eliminated when the *dust mask* selection is applied.

In the two downstream sites Beijing and Shijiazhuang, the dust plume only arrives in the morning of May 4. The model is able to simulate the arrival and departure of the plume correctly. The amplitude of the concentrations are too high for the background simulation, although this is not completely sure for the Beijing site since observations seem to be limited to 1000 $\mu g/m^3$. After assimilation the model simulations are in better agreement with the observations in especially Shijiazhuang, with best results obtained

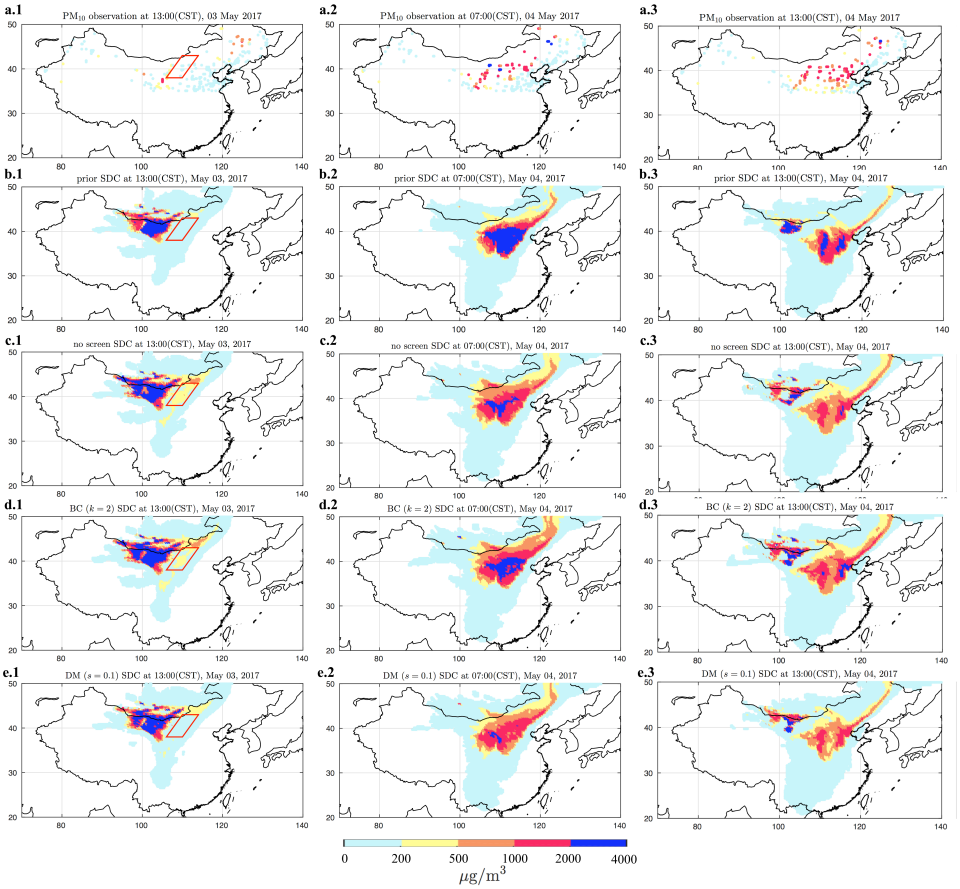

Figure 5.11: Field PM_{10}, prior and posterior surface dust concentration (SDC) map at 13:00, May 03 (a.1~e.1); 07:00, May 04 (a.1~e.1) and 13:00, May 04 (a.1~e.1)

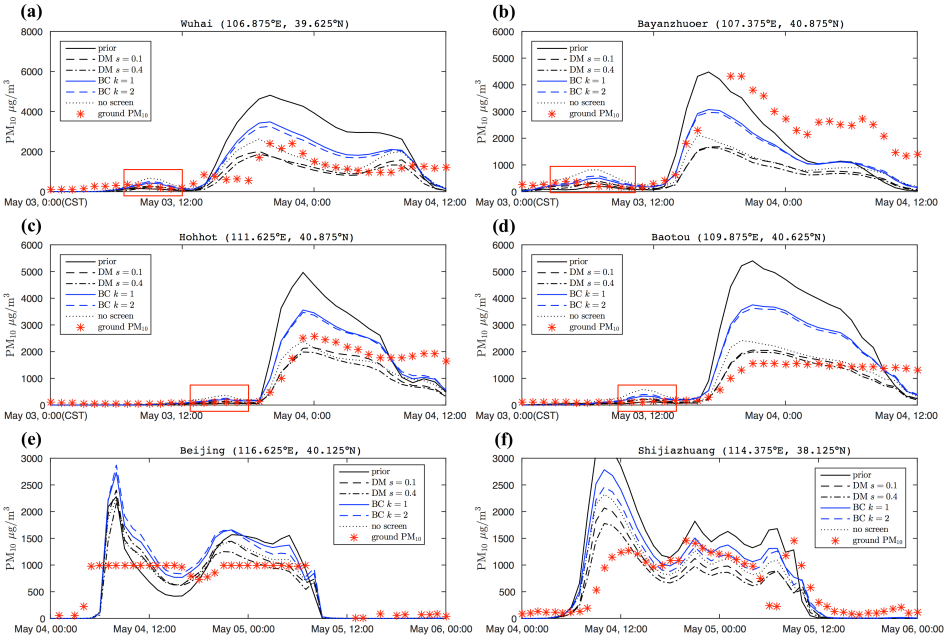

Figure 5.12: Time series of PM_{10} and surface dust concentration in C1 to C6: (C1: Wuhai; C2: Bayanzhuoer; C3: Wuhai; C4: Baotou; C5: Beijing; C6: Shijiazhuang)

using the *dust mask* selection.

5.6.4. FORECAST SKILL

A practical application of the AOD assimilation is to serve as the start of a forecast. This could be used to timely provide information to the public on the arrival of the dust plume and the expected dust concentrations.

To evaluate the forecast skill, the hourly root mean square error (RMSE) between observed and simulated surface PM_{10} has been computed over the 200 northern stations most affected by the dust. As shown in Fig. 5.13, the first and second data assimilation analysis are performed on May 03 15:00 and May 04 15:00, respectively. Each hourly forecasts before the first analysis are provided by the background model, forecasts from May 03, 15:00 to May 04, 15:00 are based on the estimated emission from the first analysis while forecasts in the following hours are based on the optimized emission from the second analysis. Therefore, all the surface PM_{10} simulations here could be used as the forecasts in the dust early warning system. Fig. 5.13 shows a time series of the RMSE values. Before the first assimilation analysis is conducted, all the forecasts are based on the background emission and show the same performance. Though our prior model already provides a good temporal match of real dust event, the discrepancy is still large due to difficulty in accurately modeling the actual dust levels. A consistent improvement of the dust forecast skill is shown when the data assimilation is implemented. The maximum RMSE around May 4 0:00 is reduced from 1000 to 600 $\mu g/m^3$ when the forecast is based on assimilated dust emissions, the forecast skill is further improved with RMSE values reduced to 500 $\mu g/m^3$ if the dust-mask selection is applied. When the *background check* is used for observation selection, RMSE values are actually higher than in the case with all observations included.

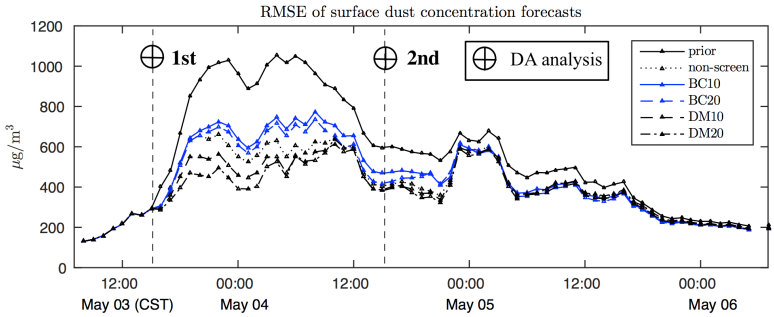

Figure 5.13: Time series of the RMSE of the model surface dust concentration forecasts with respect to the field measurements of PM_{10}

5.7. CONCLUSIONS

In this Chapter, total column AOD observations from the new geostationary satellite Himawari-8, have been used in our dust emission inversion system. Its aerosol product has a wide spatial coverage and high spatial and temporal resolution, which provides

valuable information to monitor dust storms over Asia.

An extreme dust storm event over North China during May 3-5 2017 was selected as test case for the assimilation. For this event, the Himawari-8 AOD observations were found to be consistent with the available AOD observations from the AERONET network. Simulations of dust have been made using the LOTOS-EUROS regional air quality model, and time series of simulated AOD showed in general good agreements with the observations with respect to arrival and decrease of the dust storm, but the amplitude is over estimated.

In one region the satellite retrievals of AOD showed rather high values that are not represented by the simulation model. These high AOD values could not be confirmed by AERONET observations, and might be attributed to presence of the partially clouded scenes. Using these Himawari observations in an assimilation would then lead to analyzed dust emissions that further result in incorrect simulations. Therefore, observation selection criteria have been developed by selecting only those observations that can be represented by the model. A *dust mask* selection that uses only those observations, where the model also simulates an amount of dust, was shown to provide the best results.

The assimilation system uses a reduced-tangent-linearization 4DVar technique to estimate dust emissions over daily time windows during the dust event. Both uncertainties in the meteorological wind field and the friction velocity threshold field are taken into account when the emission uncertainty is approximated. Assimilation of Himawari AOD is shown to provide emission estimates that, when used as input for the model, strongly improves the simulated AOD as well as the simulated surface concentrations compared to the PM_{10} observations. Using proper selection of AOD observations in the assimilation, the forecast skill during the dust storm was strongly improved.

REFERENCES

Anderson, E. and Järvinen, H. (1999). Variational quality control. *Quarterly Journal of the Royal Meteorological Society*, 125(554):697–722.

Arnoldi, W. E. (1951). The principle of minimized iterations in the solution of the matrix eigenvalue problem. *Quarterly of Applied Mathematics*, 9(1):17–29.

Bessho, K., Date, K., Hayashi, M., Ikeda, A., Imai, T., Inoue, H., Kumagai, Y., Miyakawa, T., Murata, H., Ohno, T., Okuyama, A., Oyama, R., Sasaki, Y., Shimazu, Y., Shimoji, K., Sumida, Y., Suzuki, M., Taniguchi, H., Tsuchiyama, H., Uesawa, D., Yokota, H., and Yoshida, R. (2016). An Introduction to Himawari-8/9— Japan’s New-Generation Geostationary Meteorological Satellites. *Journal of the Meteorological Society of Japan. Ser. II*, 94(2):151–183.

Carrer, D., Roujean, J.-L., Hautecoeur, O., and Elias, T. (2010). Daily estimates of aerosol optical thickness over land surface based on a directional and temporal analysis of SEVIRI MSG visible observations. *Journal of Geophysical Research: Atmospheres*, 115(D10).

Cesnulyte, V., Lindfors, A. V., Pitkänen, M. R. A., Lehtinen, K. E. J., Morcrette, J. J., and Arola, A. (2014). Comparing ECMWF AOD with AERONET observations at visible and UV wavelengths. *Atmospheric Chemistry and Physics*, 14(2):593–608.

Dee, D. P. and Uppala, S. (2009). Variational bias correction of satellite radiance data in the ERA-Interim reanalysis. *Quarterly Journal of the Royal Meteorological Society*, 135(644):1830–1841.

Dee, D. P., Uppala, S. M., Simmons, A. J., Berrisford, P., Poli, P., Kobayashi, S., Andrae, U., Balmaseda, M. A., Balsamo, G., Bauer, P., Bechtold, P., Beljaars, A. C. M., van de Berg, L., Bidlot, J., Bormann, N., Delsol, C., Dragani, R., Fuentes, M., Geer, A. J., Haimberger, L., Healy, S. B., Hersbach, H., Hólm, E. V., Isaksen, L., Kaallberg, P., Köhler, M., Matricardi, M., McNally, A. P., Monge-Sanz, B. M., Morcrette, J. J., Park, B. K., Peubey, C., de Rosnay, P., Tavolato, C., Thépaut, J. N., and Vitart, F. (2011). The ERA-Interim reanalysis: configuration and performance of the data assimilation system. *Quarterly Journal of the Royal Meteorological Society*, 137:553–597.

Fu, G., Prata, F., Lin, H. X., Heemink, A., Segers, A., and Lu, S. (2017). Data assimilation for volcanic ash plumes using a satellite observational operator: a case study on the 2010 Eyjafjallajökull volcanic eruption. *Atmospheric Chemistry and Physics*, 17(2):1187–1205.

Fukuda, S., Nakajima, T., Takenaka, H., Higurashi, A., Kikuchi, N., Nakajima, T. Y., and Ishida, H. (2013). New approaches to removing cloud shadows and evaluating the 380 nm surface reflectance for improved aerosol optical thickness retrievals from the GOSAT/TANSO-Cloud and Aerosol Imager. *J. Geophys. Res. Atmos.*, 118(24):2013JD020090+.

Ian, A. and Richard, W. (2012). An automated dust detection using SEVIRI: A multiyear climatology of summertime dustiness in the central and western Sahara. *Journal of Geophysical Research: Atmospheres*, 117(D8).

Ishida, H. and Nakajima, T. Y. (2009). Development of an unbiased cloud detection algorithm for a spaceborne multispectral imager. *J. Geophys. Res.*, 114(D7):D07206+.

Jin, J., Segers, A., Heemink, A., Yoshida, M., Han, W., and Lin, H.-X. (2019). Dust Emission Inversion Using Himawari-8 AODs Over East Asia: An Extreme Dust Event in May 2017. *Journal of Advances in Modeling Earth Systems*, 11(2):446–467.

Remer, L. A., Kaufman, Y. J., Tanré, D., Mattoo, S., Chu, D. A., Martins, J. V., Li, R., Ichoku, C., Levy, R. C., Kleidman, R. G., Eck, T. F., Vermote, E., and Holben, B. N. (2005). The MODIS Aerosol Algorithm, Products, and Validation. *Journal of the Atmospheric Sciences*, 62(4):947–973.

Sakov, P. and Sandery, P. (2017). An adaptive quality control procedure for data assimilation. *Tellus A: Dynamic Meteorology and Oceanography*, 69(1).

Sekiyama, T. T., Yumimoto, K., Tanaka, T. Y., Nagao, T., Kikuchi, M., and Murakami, H. (2016). Data Assimilation of Himawari-8 Aerosol Observations: Asian Dust Forecast in June 2015. *SOLA*, 12(0):86–90.

Yoshida, M., Kikuchi, M., Nagao, T. M., Murakami, H., Nomaki, T., and Higurashi, A. (2018). Common Retrieval of Aerosol Properties for Imaging Satellite Sensors. *Journal of the Meteorological Society of Japan. Ser. II*, advpub.

Yumimoto, K., Nagao, T. M., Kikuchi, M., Sekiyama, T. T., Murakami, H., Tanaka, T. Y., Ogi, A., Irie, H., Khatri, P., Okumura, H., Arai, K., Morino, I., Uchino, O., and Maki, T. (2016). Aerosol data assimilation using data from Himawari-8, a next-generation geostationary meteorological satellite. *Geophys. Res. Lett.*, 43(11):2016GL069298+.

Zhang, Z., Wu, W., Fan, M., Tao, M., Wei, J., Jin, J., Tan, Y., and Wang, Q. (2019). Validation of Himawari-8 aerosol optical depth retrievals over China. *Atmospheric Environment*, 199(1352-2310):32–44.

6

BACKTRACING DUST EMISSION ERRORS USING THE ADJOINT METHOD

Emission inversion using data assimilation relies on the correct assumptions on the background error covariance. A perfect covariance accounts for the uncertainty based on prior knowledge, and is able to explain the difference between model simulations and observations. However, a partially unrepresentative background uncertainty is unavoidable. Since in complex emission parameterization the uncertainties are induced from a lot of different inputs, they can hardly all be taken into account. In this Chapter, we report how an adjoint model can be used to detect errors in the background emission assumptions in practical dust storm emission inversions. An adjoint based sensitivity method is used as a supplement of the data assimilation system to trace back the error sources in case that large observation-minus-simulation residues remain after the assimilation.

In Chapter 5, the assimilation system successfully resolved observation-minus-simulation errors using satellite AOD observations in the most dust-affected regions. However, a large underestimation of dust in northeast China remained despite the fact the assimilated measurements indicated severe dust plumes there. We use an adjoint model of our dust simulation system to detect the most likely source region for these unresolved dust loads. The backward modeling points out the Horqin desert, which used to be considered as less important in East Asia dust storm forecast, but is in this case the most likely emission source. The reference emission and uncertainty are then reconstructed over the Horqin desert by assuming higher surface erodibility. After the emission reconstruction, the emission inversion is performed again and the posterior dust simulations are now in better agreement with the reality.

This chapter is submitted for publication to *Atmospheric Chemistry and Physics*:
Backtracing back dust emission errors using the adjoint method.

6.1. INTRODUCTION

MOST dust emission inversion systems (Di Tomaso et al., 2017, Khade et al., 2013, Yumimoto et al., 2016, Yumimoto and Takemura, 2015) use variational methods to estimate the optimal emissions. Since a large programming effort is required to formulate and implement the tangent linear (TL) model and its adjoint model (AM) in the traditional 4DVar, the systems often employ model-reduced or ensemble-based variational assimilation. With model reduction, a simplified tangent-linear model is used to propagate the background error covariance. Ensemble methods generate an ensemble of perturbed emissions and propagate this ensemble to approximate the evolution of background error covariance. Both of these adjoint-free methods are able to reduce uncertainty in emissions by determining the dominant and sensitive patterns. The computation costs necessarily limit the size of the reduced tangent-linear model or the size of the ensemble to a number that is much smaller than the size of the emission parameter space. Consequently, the optimal emission that can be calculated are constrained to a subset of the original space, which is predefined through using the model/parameter reduction.

A crucial element of all inversion methods is the proper specification of the spread of likely estimates, which are for emission inversions the uncertainties in these emissions. Ideally, the emission uncertainties should be both physically reasonable and capable of providing sufficient variations to explain the observation-minus-simulation differences. Unfortunately, the many possible errors that could be present in the dust parameterizations could not be described all together, and simplifications are needed. As of yet, most studies used fairly coarse emission uncertainty, limited to optimization of a few scaling factors for emission inventories spanning a larger domain. In the dust emission inversion research by Yumimoto et al. (2008), the emission background covariance is assumed to be uncorrelated in space and the uncertainty is simply defined as 500% of the prior emission flux rate. Khade et al. (2013) introduced an uncertain erodibility fraction parameter field to introduce variability in dust emissions over the Sahara desert, and reduced the uncertainty by using an Ensemble Adjustment Kalman filter (EAKF). Di Tomaso et al. (2017) attributed the emission error to the uncertainty in the Friction Velocity Threshold (FVT), which was reduced by estimating an optimal correction factor using a Local Ensemble Transform Kalman Filter (LETKF). Limited by the ensemble size, the multiplicative value was considered spatially and temporally constant. In the study described in Chapter 3, a spatially varying multiplicative factor was applied to compensate the errors in the FVT in the dust emission parametrization. The uncertainties were described by including uncertainty in the FVT and in the surface wind field in Chapter 5.

An essential step before starting an inversion is to check weather the specified uncertainties are actually able to explain the differences between observations and simulations. The sensitivity of the model with respect to the uncertainties should learn if the parameters considered are really the dominant problematic parameters. Under the circumstances that the aforementioned model-reduced or ensemble-based variational data assimilation algorithms are adopted, the knowledge of the sensitivity is particularly valuable, since it can efficiently help the model/parameter reduction by removing those insensitive problematic parameters. Based on this knowledge, the background covariance could be improved which will immediately improve the emission inversions.

An efficient way of examining sensitivities is the use of an adjoint model. This is especially useful to examine the sensitivity of a limited number of output values for changes in a large amount of input values. The first implementations of an adjoint of an atmospheric transport model was in the early 1980's with applications in numerical weather forecasting (DIMET and TALAGRAND, 1986, Talagrand and Courtier, 1987). Implementations in chemical transport models (CTM's) can be found in (An et al., 2016, Elbern et al., 1997, Hakami et al., 2005, Henze et al., 2007a, Hourdin and Talagrand, 2006). The standard forward version of a CTM requires input from initial conditions and model parameters, and provides concentrations in receptor points as output. the state evolution could therefore be regarded as source-oriented. Adjoint models, however, could be regarded as receptor-oriented, as they use a distortion in a receptor point as input, and compute from this the distortions of the input parameters that explain this. In case of many uncertain parameters, an adjoint model is very efficient in calculating model sensitivities than other methods such as the traditional finite-difference method, which requires many forward model runs with perturbed inputs (Zhai et al., 2018).

In this Chapter, we first review the emission inversion described in Chapter 5, where the Himawari-8 satellite AOD observations was assimilated for a dust storm event in May 2017. Although significant improvements on dust simulation and forecast skills driven by the posterior emissions were reported, some large regional simulation errors remained. In particular, during three severe dust outbreaks (SD) some high dust concentrations observed at ground level were not at all or not completely resolved by the a posteriori simulations, although the assimilated AOD observations also indicated that a severe dust plume was present. An adjoint version of the transport model is then introduced. It will not be used to optimize emissions (although that would make sense in a 4DVar context), but instead it is used to trace back the potential emission source that could explain the observed high concentrations. For the three selected dust outbreaks the sensitivity towards the emissions is computed for observation sites that were not resolved correctly by the assimilation. Each of the results pointed at the Horqin desert as the most likely source region. Up to now, this desert was considered to be of of less importance in dust simulation models since the dominant sources are usually in the Gobi desert. To evaluate whether dust emissions from the Horqin desert could indeed explain the observed high concentrations, a new inversion is applied with a modified emission model with a higher surface erodibility over this region. The new reference model is further improved by assimilating ground based PM_{10} observations, which significantly reduce the remaining differences.

While various studies on aerosol and/or dust emission inverse modeling assume that the location of sources is known, this study is different in focusing on sources that are not known yet. Within this context, the highlights are twofold. First, this study shows how an adjoint model could be used to identify potential sources in case large observation-minus-simulation error residues are found that cannot be explained by the existing model and assumed uncertainties, and thus cannot be corrected using a data assimilation system. With the potential source region identified by the adjoint sensitivities, the background emission uncertainty is updated. Second, the Horqin desert is validated to be an important source of dust. Based on our results it is advised that this region should be taken into account as potential source in east Asian dust forecasts.

This Chapter is organized as follows: Chapter 6.2 reviews the emission uncertainty construction in our previous dust storm emission inversion over a dust storm in May 2017 studied in Chapter 5. Chapter 6.3 shows the high error residues in the assimilation analysis in the previous study, specifically, three severe dust (SD) outbreaks are not well reproduced in northeast China even though the assimilated measurements indicated severe dust plume. Chapter 6.4 presents the theory of adjoint model and how to detect the potential emission source for the three SDs. In Chapter 6.5, the dust model is reconstructed by assuming higher soil erodibility for emissions over the tracked potential source regions. The emission uncertainty is also updated automatically. Besides, regional emission inversion is performed again. Chapter 6.6 further discusses the added value using adjoint sensitivities for detecting sources to resolve simulation errors.

6.2. DUST EMISSION INVERSION

The dust storm event over east Asia that took place in May 2017 has been used as case study for dust emission inversion in Chapter 5. In that study, an assimilation system around the same transport model (LOTOS-EUROS) was used to assimilate AOD observations from the Advanced Himawari Imager (AHI) instrument on board of the geostationary Himawari-8 satellite (Yoshida et al., 2018). The AHI instrument provides observations with a fine temporal (10 mins) and spatial (5 kms) resolution and a wide domain covering the East Asia. The assimilation system adjusted the dust emissions in the source regions to obtain the best comparison between simulated and observed AOD. Through comparison with independent PM_{10} data, the dust concentration forecast was validated to be strongly improved at most downwind sites by the assimilation.

The uncertainty of the emission in Chapter 5 was mainly assigned as a sum of two sources, the uncertainty in the friction velocity threshold and in the erosive wind fields. The uncertainty in the friction velocity threshold u_{*t} was described by a spatially varying multiplicative factor β, defined as random variables with a mean of 1.0 and a standard deviation σ of 10%. The uncertainty in the friction wind velocity u_* was described by the spread in a meteorological ensemble with 26 members. Note that the dust emission model computes hourly emissions per grid cell, which may vary strongly from hour to hour. In the inversion system, the temporal variation of the emission model is maintained and could be further increased by the uncertainty during the assimilation window(s) of 24 hours.

Fig. 6.1a shows the accumulated dust emission flux from May 02 15:00 to May 04 15:00 China standard time (CST). These dust emissions are responsible for the event that is studied. Outside of this period, the dust emissions are rather weak. The figure shows that the main source regions are in the Gobi and Mongolia deserts. Fig. 6.1b shows the corresponding standard deviation of the accumulated emission that follows from assumed uncertainty.

Snapshots of Himawari-8 AODs are shown in Fig. 6.5. This type of data was assimilated with LOTOS-EUROS simulations in two 24 h windows. The posterior accumulated emission are also shown in Fig. 6.1c. Both the prior and posterior simulation indicate that the dust was emitted from the Gobi, Mongolia and Alex deserts. Previous research (Zhang et al., 2018) and simulation from an operational dust forecast model, BSC-DREAM8b, have identified the same emission source for this event. The red box in

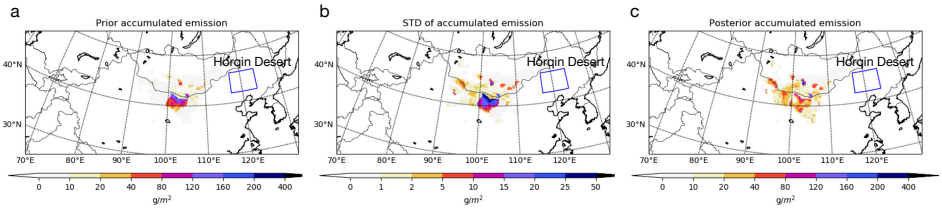

Figure 6.1: Accumulated prior dust emissions from 2017 May 02 15:00 (CST) to May 04 15:00 (left), as well as the assumed standard deviation, and the estimate after assimilation.

Fig. 6.2 indicates the location of the Horqin desert. That shows that the area is not a completely sandy desert but has some vegetation, although sparse. No (or hardly) any dust emissions are assumed to be released from here in the emission model, and therefore also the associated uncertainty is zero. Thus, the Horqin Desert is in the model considered as completely free of dust emissions, and emissions could also not be introduced by the inversion system. However, as we shall see later on, dust emissions from this region could very well explain observed differences between observations and simulations, and therefore the inversion system should be adjusted to allow emissions from there too.

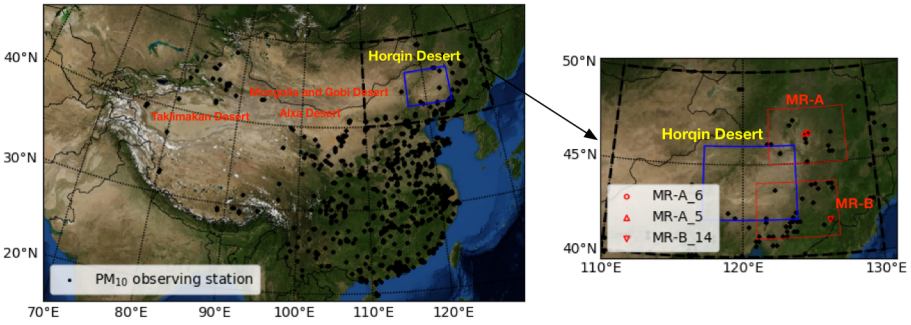

Figure 6.2: The Blue Marble of East Asia; the locations of Mongolia and Gobi desert, Alxa desert, Taklimakan desert, and Horqin desert; the China MEP air quality monitoring network. Red marked region A (MR-A) and Red marked region 2 (MR2) are where the dust is observed but not reproduced using chemical transport models

Dust concentration forecasts based on the *a posteriori* emissions have been validated by comparison with ground based PM_{10} measurements. Snapshots of the *a posteriori* surface dust concentrations as well as PM_{10} measurements are shown in Fig. 6.3 ~ Fig. 6.4.

6.3. REGIONAL DIFFERENCE BETWEEN OBSERVATIONS AND SIMULATIONS

As of yet, over 1,500 field stations all over China has been established by the China Ministry of Environmental Protection (MEP) to monitor atmospheric constituents including $PM_{2.5}$, PM_{10}, CO, O_3, SO_2 and NO_2. The observation network is shown in Fig. 6.2. Hourly averaged PM_{10} observations from the network are used as independent data to evaluate the *a posteriori* dust simulations after assimilation of Himawari-8 AOD. Although these PM_{10} measurements are actually a sum of the dust aerosols and particles released in local activities, the values are dominated by dust during the severe events that are studied here. Therefore, all these measurements are assumed to be representative for comparison with the dust simulations. In case of less severe dust storms, observational bias corrections (Dee and Uppala, 2009) or baseline removal in Chapter 4 would be required to remove the *non-dust* part from the observations to allow comparison with a 'dust-only' model.

Although for most locations the *a posteriori* dust simulations showed good agreement with the PM_{10} observations, some large mismatches remained, especially in the north east part of China. Specifically, extremely high values of surface dust concentration over three severe dust events were reported by the ground-based monitoring system in this region, but neither could be reproduced to a full extent by the simulations. This is illustrated in Fig. 6.3 for the first severe dust plume from 2017 May 03 08:00(CST) to 20:00, which we will refer to as "SD1", and in Fig. 6.4 for the second dust outbreak from May 04 02:00 to 14:00, which is referred as "SD2". Similar figures for the third events ("SD3") is available as supplementary.

The top row in Fig. 6.3 shows PM_{10} observations at three different moments covering the SD1. Obviously a dust plume that crosses the red marked region A (MR-A), with max PM_{10} observations rising rapidly from 200 $\mu g/m^3$ at 08:00 to more than 2,000 $\mu g/m^3$ at 20:00. The second and third row show the *a priori* and *a posteriori* LOTOS-EUROS simulations on the surface dust concentration for the same hours. Unfortunately, the simulations in the MR-A region were completely free of dust in both simulations. Note that the simulated prior and posterior AODs, which are not shown here, generally have a similar profile to the surface dust concentration shown in Fig. 6.3(b) and (c).

Himawari-8 AOD also indicated the existence of a severe dust plume over MR-A, a snapshot of AOD map at May 3 12:30 can be seen in Fig. 6.5(a). Most of AODs over MR-A exceeds 1.2. Our first 24 h cycle of emission inversion was performed by assimilating these high-value AODs. The simulations driven by the posterior emission fields, shown in Fig. 6.3(c.1) ~(c.3), still present that the MR-A is clear of dust during this whole period. The difference between the posterior simulation and observations indicates that the current emission and its spread cannot explain the first dust plume in MR-A. In other words, the dust plume moved over MR-A was not due to emissions from Gobi and Mongolia deserts we predefined in the background emission, but some deserts else.

The three snapshots of PM_{10} observations in Fig. 6.4(a) indicate the second severe dust plume (SD2) over the same region MR-A. In this case, both *a prior* and *a posterior* LOTOS-EUROS model simulate a dust plume over MR-A (see Fig. 6.4(b) and Fig. 6.4(c)), which was backtracked on the emissions from Gobi, Mongolia and Alex deserts. The

maximum of the modeling surface dust concentration over MR-A on May 4 is around 500 $\mu g/m^3$, however, the maximum PM_{10} measurement value exceeds 2,000 $\mu g/m^3$. It is true that these observation-minus-simulation might be caused by the emission underestimation over the Mongolia and Gobi deserts. Yet those emissions also contributed the dust plume observed in Central China. In this case, those dust flux rates are actually constrained at a modest level by other measurements in emission inversion analysis. Besides, the dust plume did not fully cover the observed dust-affected regions. Thus, the dust level is considered to be partially due to the predefined emissions, but also caused by emission somewhere.

Himawari-8 measurements are not successfully retrieved due to the cloud scene over MR-A, thus AOD snapshots are not presented.

The underestimation of dust concentrations over MR-A on the SD1 and SD2 was also found in other simulation systems, for example as published by the SDS-WAS service[1]; as example, results over SD1 and SD2 from the BSC-DREAM8b model are shown in the last row of Fig. 6.3 and Fig. 6.4, respectively. These suggests that some sources of dust might be missing in the emission models that are used to drive the simulation system.

Similar conclusion was drawn for the third dust outbreak ("SD3"), for which simulation and PM_{10} measurements are available in supplementary. For SD3, it was found that severe dust plume was recorded over the marked region (MR-B) in the northeast China. However, neither the *a prior*, *a posterior* simulations nor the BSC-DREAM8b simulation reproduce any dust over MR-B, though the assimilated Himawari-8 AODs, see in Fig. 6.5(b), did indicated the existence of a dust plume over this region.

To further illustrate the three severe dust outbreaks in the Northeast China on May 03 and 04, respectively, the time series of PM_{10} observations in all monitoring stations inside the marked regions MR-A shown in Fig. 6.6(a). The overall PM_{10} levels within these two regions is shown in terms of the hourly mean plus/minus standard deviation over observations. The mean PM_{10} levels are around 100 ~200 $\mu g/m^3$ when there is no dust (earlier than May 02 12:00). The peak of SD1 arrives in marked region MR-A around May 03 08:00, and has left the region at May 04 00:00; the mean PM_{10} concentrations have reached a value up to 1,000 $\mu g/m^3$. The most severe dust plume occurs during SD2 at May 04, with mean PM_{10} measurements inside MR-A up to 1500 $\mu g/m^3$.

6.4. DETERMINE EMISSION SOURCES USING AN ADJOINT MODEL

The adjoint approach provides an efficient tool for calculating the sensitivity of a simulation model with respect to its input parameters. In this study, the adjoint is used to identify potential source regions for dust that could explain the mismatch between simulations and observations the north east of China.

6.4.1. ADJOINT THEORY

The following notation will be used for the discrete time step of our simulation model:

$$\boldsymbol{x}^k = \mathcal{M}^k(\boldsymbol{x}^{k-1}, \boldsymbol{f}^{k-1}) \tag{6.1}$$

[1] https://ess.bsc.es/bsc-dust-daily-forecast

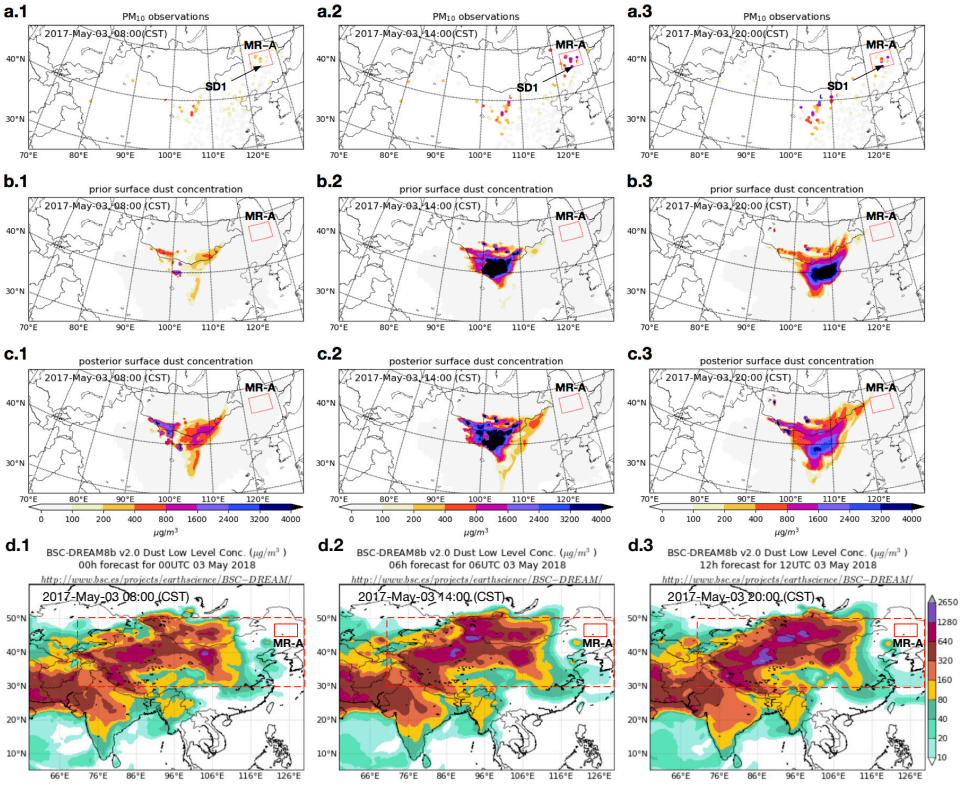

Figure 6.3: PM_{10} observations (a.1~a.3) vs. surface dust concentration simulation of the 1st severe dust (SD1) from LOTOS-EUROS prior (b.1~b.3), posterior (c.1~c.3) and BSC-DREAM8b (d.1~d.3) over the marked region A (MR-A) at May 03 08:00 (CST): a.1~d.1; 14:00 (CST): a.2~d.2; 20:00 (CST): a.3~d.3.

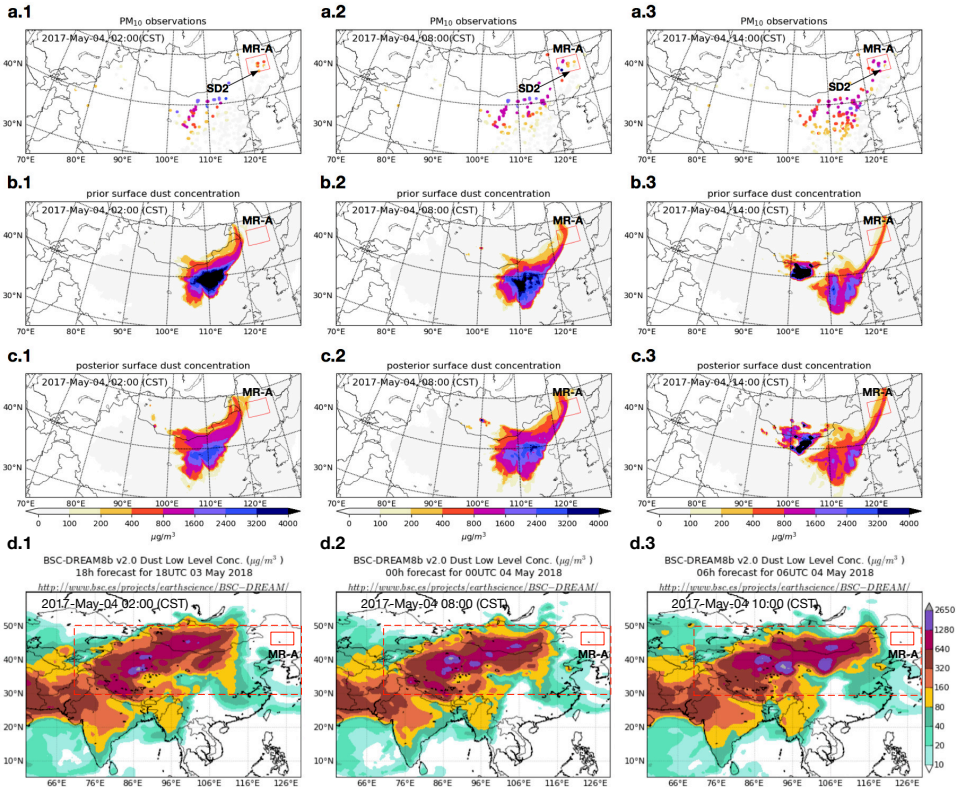

Figure 6.4: PM_{10} observations (a.1~a.3) vs. surface dust concentration simulation of the 2nd severe dust (SD2) from LOTOS-EUROS prior (b.1~b.3), posterior (c.1~c.3) and BSC-DREAM8b (d.1~d.3) over the marked region A (MR-A) at May 04 02:00 (CST): a.1~d.1; 08:00 (CST): a.2~d.2; 14:00 (CST): a.3~d.3.

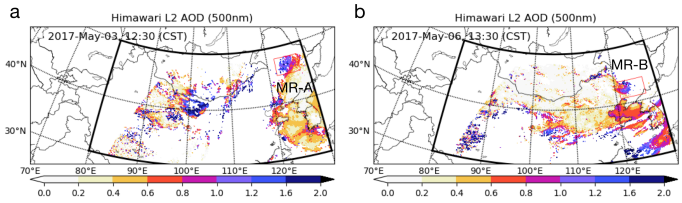

Figure 6.5: Two snapshots of Himawari-8 Level 2 AODs (500 nm) at May 03 12:30 and May 06 13:30. Note that only observations in the black framework are presented, insides which AODs failed in retrieval at the white pixels.

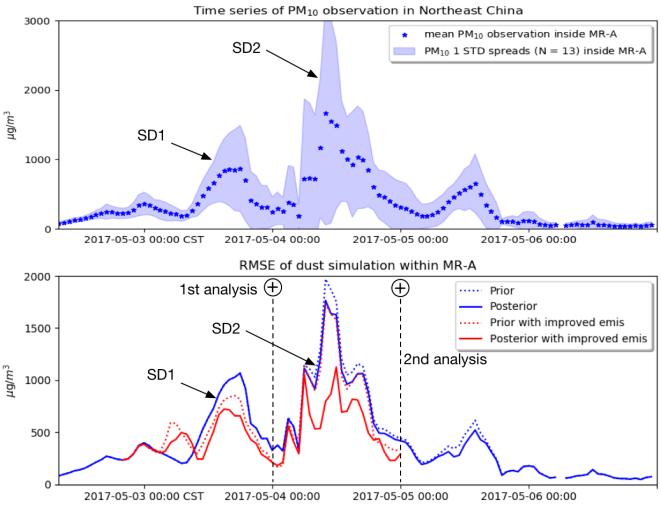

Figure 6.6: a: Average and standard deviation (STD) spread of the hourly PM_{10} variations inside the MR-A (13 sites) and MR2 (29 sites); b: root mean square error of prior and posterior simulation, reconstructed prior and posterior with MR-A and MR2. Maps of these stations can be seen in Fig. 6.2.

in this equation, $\boldsymbol{x}^k$ denotes the state vector at time k that consists of 3D fields of dust aerosol concentrations for each of the 5 dust size bins in the model, the input vector $\boldsymbol{f}^{k-1}$ consists of emission fields for the 5 size bins, and $\mathcal{M}^k$ denotes the model operator that simulates $\boldsymbol{x}^k$ given the state and input at time $k-1$. For a dust transport simulation, the model is linear towards both $\boldsymbol{x}$ and $\boldsymbol{f}$, and could therefore be written using matrix operators:

$$\boldsymbol{x}^k = \mathbf{M}^{k-1}\,\boldsymbol{x}^{k-1} + \mathbf{E}^{k-1}\,\boldsymbol{f}^{k-1} \tag{6.2}$$

the operator $\mathbf{M}^k$ represents the transport part of the model, while $\mathbf{E}^k$ represents the emission part. Repeated application of Eq. (6.2) provides the evolution of the state from time $k-K$ to time k:

$$\begin{aligned}
\boldsymbol{x}^k &= \mathbf{M}^{k-1}\left(\mathbf{M}^{k-2}\,\boldsymbol{x}^{k-2} + \mathbf{E}^{k-2}\,\boldsymbol{f}^{k-2}\right) + \mathbf{E}^{k-1}\,\boldsymbol{f}^{k-1} && (6.3)\\
&= \mathbf{M}^{k-1}\cdot\mathbf{M}^{k-2}\,\boldsymbol{x}^{k-2} + \mathbf{M}^{k-1}\cdot\mathbf{E}^{k-2}\,\boldsymbol{f}^{k-2} + \mathbf{E}^{k-1}\,\boldsymbol{f}^{k-1} && (6.4)\\
&= \mathbf{M}^{k-1}\cdot\mathbf{M}^{k-2}\cdot\ldots\cdot\mathbf{M}^{k-(K-1)}\cdot\mathbf{M}^{k-K}\,\boldsymbol{x}^{k-K} + && (6.5)\\
&\quad \mathbf{M}^{k-1}\cdot\mathbf{M}^{k-2}\cdot\ldots\cdot\mathbf{M}^{k-(K-1)}\cdot\mathbf{E}^{k-K}\,\boldsymbol{f}^{k-K} + && (6.6)\\
&\quad \ldots + \mathbf{M}^{k-1}\cdot\mathbf{E}^{k-2}\,\boldsymbol{f}^{k-2} + \mathbf{E}^{k-1}\,\boldsymbol{f}^{k-1} && (6.7)
\end{aligned}$$

We define a model *response function* as a scalar function of the state:

$$\mathcal{J}(\boldsymbol{x}^k) \in \mathcal{R} \tag{6.8}$$

the response could for example be defined as the simulation at a single location (an observation site), or an average over multiple grid cells. The gradient of this response function at time k with respect to the input vector $\boldsymbol{f}^{k-K}$ follows from application of the chain

rule, and using that Eq. (6.6) is the only term in the expansion of $\boldsymbol{x}^k$ that depends on $\boldsymbol{f}^{k-K}$:

$$\nabla_{\boldsymbol{f}^{k-K}} \mathcal{J}(\boldsymbol{x}^k) = \nabla_{\boldsymbol{f}^{k-K}} \left(\boldsymbol{x}^k\right)^T \cdot \nabla_{\boldsymbol{x}^k} \mathcal{J}(\boldsymbol{x}^k) \tag{6.9}$$

$$= (\mathbf{E}^{k-K})^T \cdot (\mathbf{M}^{k-K})^T \cdot \ldots \cdot (\mathbf{M}^{k-2})^T \cdot (\mathbf{M}^{k-1})^T \cdot \nabla_{\boldsymbol{x}^k} \mathcal{J}(\boldsymbol{x}^k) \tag{6.10}$$

the transpose $(\mathbf{M}^k)^T$ of the linear model operator $(\mathbf{M}^k)$ is referred as the *adjoint model*. To compute the above gradient $\nabla\mathcal{J}$, the adjoint model is applied in a reverse time sequence $k-1, k-2, \ldots, k-K$. The first adjoint operation in this sequence is applied on the *adjoint forcing*:

$$\nabla_{\boldsymbol{x}^k} \mathcal{J}(\boldsymbol{x}^k) \tag{6.11}$$

An adjoint model is powerful tool to compute the model response with respect to various input parameters. A useful application is found in 4DVar data assimilation, where it is used to derive the gradient of a cost function for the difference between observations and simulations. In the context of air quality, this approach has been used to constrain initial conditions, emissions, and other uncertain model parameters such as uptake (Elbern et al., 2000, Henze et al., 2009). For this study, an adjoint implementation of the LOTOS-EUROS model will be used to identify potential emission source regions. The adjoint model is created from the same source code, but using an internal flag it applies adjoint (transpose) versions of the transport and emission operators. Using a negative time step it is able to run backwards in time, as is required to computed gradients as Eq. 6.10. The assimilation system that is used in this study remains the reduced-tangent-linearization 4DVar that was developed in Chapter 3, which does not use the adjoint implementation. Although it would be possible to use the adjoint for the assimilation too, it was chosen to keep the assimilation system the same in order to compare results before and after the introduction of new emission sources.

6.4.2. TEST THE IMPLEMENTATION OF THE ADJOINT MODEL

Before using the adjoint model to identify potential emission sources, the implementation is first illustrated and tested by looking at a single site.

A suitable test to validate whether the adjoint model computes the correct sensitivity of the model towards changes in the input is to compare its evaluation with a finite-difference method (Guerrette and Henze, 2015, Henze et al., 2007b). That is, the sensitivity of a model response $\mathcal{J}(\boldsymbol{x}^k)$ to the previous emission field $\boldsymbol{f}^{k-K}$ is computed either using the adjoint or by perturbing the emission field. For this test, we define the response function to be the dust concentration in the grid cell with the most severe dust plume (SD1) is measured within the marked region MR-A, referred to as "MR-A_6". The response function becomes:

$$\mathcal{J}(\boldsymbol{x}^k) = \mathbf{H}\boldsymbol{x}^k \tag{6.12}$$

where the matrix operator $\mathbf{H}$ is actually a row vector with zeros except for the elements that represent the 5 dust size bins in the selected grid cell:

$$\mathbf{H} = [0, \ldots, 0, 1, 1, 1, 1, 1, 0, \ldots, 0] \tag{6.13}$$

The adjoint forcing becomes:

$$\nabla_{\boldsymbol{x}^k} \mathcal{J}(\boldsymbol{x}^k) = \mathbf{H}^T \tag{6.14}$$

Time t_k is set to 19:00 on May 3 2017 when the dust concentration in MR-A_6 peaked.

Following Eq. (6.10), the sensitivities of this dust concentration towards dust emissions at time t_{k-K} is:

$$\nabla_{\boldsymbol{f}^{k-K}} \mathcal{J}(\boldsymbol{x}^k) = (\mathbf{E}^{k-K})^T \cdot (\mathbf{M}^{k-K})^T \cdot \ldots \cdot (\mathbf{M}^{k-2})^T \cdot (\mathbf{M}^{k-1})^T \cdot \mathbf{H}^T \tag{6.15}$$

A snapshot of the adjoint emission sensitivities at May 03, 13:00 CST, is shown in Fig. 6.7(a) for one of the 5 dust size bins in the model. According to these values, the dust simulation in MR-A_6 valid for 6 hours later is most sensitive to emissions that are roughly in the rectangular box. Note that in this example the response function $\mathcal{J}$ has units of concentrations, which gives $\nabla_f \mathcal{J}$ the units of concentrations (μg/m^3) over emissions (μg/m^2/s), equivalent to s/m.

The same sensitivity could also be calculated using a finite-difference method. For this, 16 locations are chosen within the box, at locations where the adjoint sensitivities are non-zero; the locations are marked with circles. Then 16 model runs are performed over [13:00,19:00], where each run is similar to a standard simulation, but using emissions that are only non-zero at [13:00,14:00] at just one of the 16 marked locations. The magnitude of these emissions is simply set to 1 μg/m^2/s for each bin. The result of each simulation is the simulated concentration in μg/m^3 in the MR-A_6 location at 19:00. The ratio between simulated concentration and emission has units s/m and is a measure for the sensitivity of the simulation in MR-A_6 at 19:00 towards an emission at one of the marked locations at 13:00.

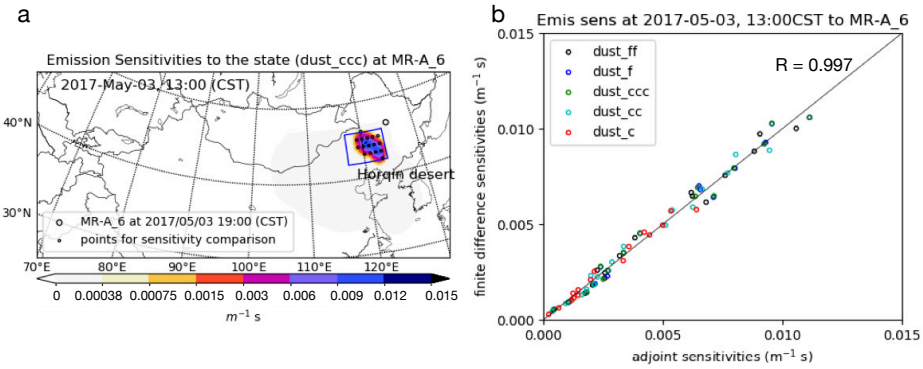

Figure 6.7: Illustration of sensitivities of dust concentrations at 19:00 in location MR-A_6 towards emissions from selected points at 13:00; (a): map of emission sensitivities computed by adjoint model; (b): comparison between sensitivities computed by adjoint method and finite differences.

The scatter plot in Fig. 6.7(b) shows the 16 computed sensitivities (for each of the 5 size bins) versus the sensitivities computed with the adjoint model. The results show that the adjoint-computed sensitivities are in good agreement with the finite difference sensitivities, which results in a relative high *Pearson* correlation coefficient $R = 0.997$.

The comparison suggests that the adjoint model has been implemented correctly. The differences that remain might be due to rounding errors at points where the sensitivity is low, and model processes other than transport and emission which are not included in the adjoint. Both the finite difference and adjoint method seem able to derive emission sensitivities. An advantage of the adjoint method however is that it computes sensitivities with one single simulation, while the fine difference method requires many more (16 in this example).

6.4.3. IDENTIFICATION OF EMISSION SOURCES

During the aforementioned investigated severe dust outbreaks (SD1 and SD2), the emission inversion was not able to provide *a posteriori* simulations that correctly represented the high dust concentrations observed in sites in the north east of China. To identify whether this could be due to missing dust sources, the adjoint model is used to identify potential source regions.

Similar as for the illustrative example in section 6.4.2, the sensitivity of a response function towards changes in emissions is computed using the adjoint model, for each of the 3 dust outbreaks. The adjoint forcing $\mathbf{H}^T$ in Eq. (6.15) are chosen as the observed state variables in MR-A_6 on May 03 19:00 for SD1, in MR-A_5 on May 04 10:00 for SD2, in MR-B_14 on May 06 18:00 for SD3, respectively. The location of MR-A_6, MR-A_5 and MR-B_14 can be found in Fig. 6.2(b). These three sites (and also the surrounding stations) reported the highest PM_{10} levels during the three dust outbreaks. For each case, the adjoint forcing $\mathbf{H}^T$ are filled with values of 10 $\mu g/m^3$ for each bin in the cell with the observation site. Time series of emission sensitivity fields are shown in Fig. 6.8 for the severe dust outbreaks SD1 and SD2, while the sensitivities series over SD3 are reported in the supplementary material.

Figures 6.8(a.1)~(a.6) show the potential source regions for the high PM_{10} values observed in MR-A_6 on May 03 11:00. The blue marked box encloses the Horqin desert, which is a potential source region for dust emitted 10 hours before the observation time. If the dust was emitted earlier, it seems to originate from regions further south. However, these are densely populated regions covered with vegetation, and therefore not a likely source of dust. The sensitivity maps show that for this time period the MR-A_6 location is not sensitive for dust emitted from the Gobi and Mongolia deserts, which are in the current emission model the main source regions. This explains also why the assimilation system, that was based on adjusting emissions from these deserts, was not able to resolve the high dust levels within marked region MR-A during SD1.

As shown in Fig. 6.8(b.1)~(b.6), a potential source region for dust observed in marked region MR-A during SD2 is again the Horqin desert, in case the emission took place 12 hours before observation. For emissions longer ago, the Gobi and Mongolia deserts could be source regions too. According to the reference and posterior dust simulation in Fig. 6.4, the dust plume that originated from the Gobi desert was in fact carried to MR-A on May 04, with 20 to 30 hours of cumulative transport. However, the simulated dust concentrations in this plume are much lower than the observed PM_{10} concentrations. The best explanation is that the dust plume was first released from the Gobi desert, and a part of it was carried to north east China by the prevailing winds. When it crossed over the Horqin desert, huge amounts of new dust particles were lifted too, and the mixed

plume reached marked region MR-A on May 4. A study by Minamoto et al. (2018) also concluded that the dust particles in SD2 were not only from the Gobi desert, but also the Horqin desert, which was up to now not recognized as a potential source of East Asian dust.

Similar conclusions were drawn for the severe dust event ("SD3"), for which figures of backward emission sensitivities are available as supplementary material. For SD3, it was noticed that dust emissions from the Horqin desert between May 06 09:00 to 15:00 could explain the high dust loads observed. Earlier emissions are traced northwards from regions in Siberia that are considered as non-erodible.

The simulation of the emission source sensitivities over the three independent dust events all indicated that the Horqin desert is likely to be the the main source region for SD1 and SD3, and also at least partly a source region for SD2. Therefore, the Horqin desert deserves more attentions while modeling dust storms over East Asian, especially when dust is observed in north east China.

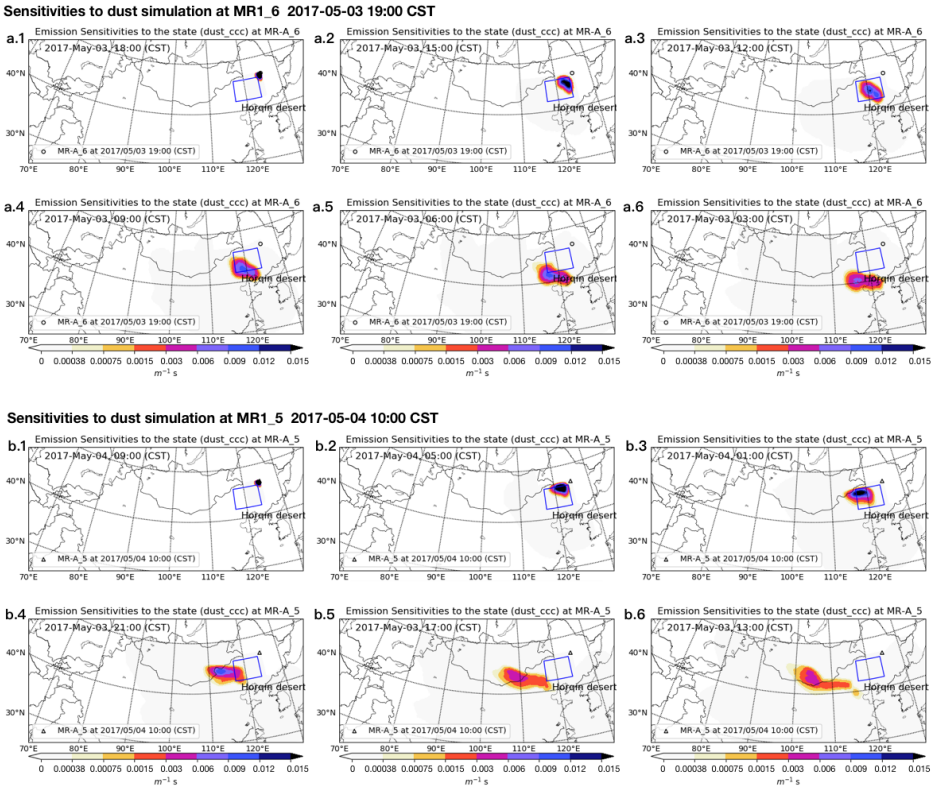

Figure 6.8: Backward time series of emission sensitivity of the dust simulation at MR-A_6 2017 May 03, 19:00 CST, and at MR-A_5 2017 May 04 10:00.

6.5. EMISSION INVERSION WITH IMPROVED EMISSION UNCERTAINTY

Inaccurate inputs such as vegetation cover, surface roughness, topography, or inaccurate emission parametrization, are all possible reasons why the current simulation model is not always able to simulate the actual dust emissions. From the study with the adjoint model it was shown that a lack of emissions from the Horqin deserts is likely to be one of these reasons. To allow dust emissions from this region too, the following changes were applied to the model the emissions and their uncertainties:

- In the landuse data base, most parts of the Horqin desert are described as '*sparse vegetated*'. For this region, the properties of sparse vegetated surfaces are set similar as '*bare areas*', which leads to a higher erodibility parameter $\mathcal{C}_i$ in Eq. 2.1.
- The topography based emission correction is disabled, leading to $\mathcal{S}_i = 1$ in Eq. 2.8.
- A tuning factor 0.7 is used to obtain a lower new friction velocity threshold in Eq. 2.2.
- The uncertainties in the new emission field is described similar as in Chapter 3~4. by correction factors applied to the new friction velocity threshold. The correction factors are spatially varying and have a mean 1 and a standard deviation 10%.

These changes are highly empirical, and chosen just to have better dust simulations for May 2017. However, these might not be sufficient to correctly describe the emissions from the Horqin dessert during other events. Application in other simulations therefore requires careful inspection by the user.

The assimilation of Himawari-8 AODs described in Chapter 5 has been repeated using the new emission and uncertainty model. The experiment is set from the May 03 to May 05 with two 24-h assimilation cycles, which covers the two test dust outbreaks, SD1 and SD2, respectively. As seen in Fig. 6.6(b), the two assimilation analysis are performed at May 04 00:00 and May 05 00:00, respectively. Each of them calculates the most likely emission fields in the past 24 hours that fits both the prior information and available measurements. Himawari-8 AODs are assimilated in the first cycle, of which the measurements error configuration are same to sets in Chapter 5. However, almost no AODs are retrieved in the second window over the MR-A region, hence the ground PM_{10} observation are assimilated instead, of which the representation errors are set similar to the ones in Chapter 4.

The model domain is still configured on the whole East Asia from 15°N to 50°N and 70°E to 140°E shown in Fig. 6.2. The computation complexity on our reduce-tangent-linearization 4DVar is generally proportional to the size of uncertain emission fields. To save the computation costs, the aforementioned new emission and uncertainty are only applied to dust emission over the Horqin deserts. While over the rest domain, the deterministic emission scheme in Chapter 5 is used.

The accumulated dust emissions before and after assimilation are present in Fig. 6.9. After assimilation (panel (b)), a much stronger total emission is estimated than what is computed by the updated *a priori* model (panel (a)). In comparison, the 'old'

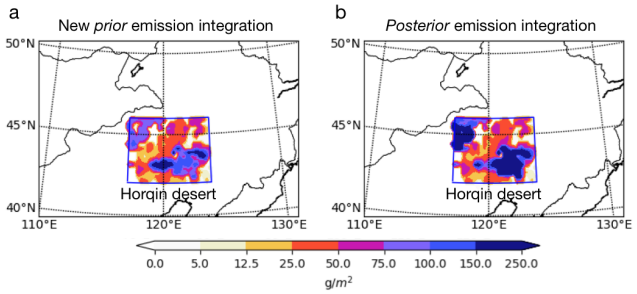

Figure 6.9: Accumulated dust emissions over Horqin Desert from May 03, 20:00 CST to May 05 07:00 (SD2): (a) prior emissions; (b) posterior emissions. The 'old' *priori* and *posterior* accumulated emission map can be seen in Fig.6.1

parametrization scheme indicates that there is no dust emission at all as shown in Fig. 6.1. Snapshots of the dust simulations on SD1 and SD2 driven by either these emissions are shown in Fig. 6.10 and Fig. 6.11 for three different times (columns), respectively; in each figure, the top row shows simulations using the reference emissions, and the bottom row using the assimilation result.

These maps could be compared to the observations and simulations using the original emission model as shown in Fig. 6.3 and Fig. 6.4. Driven by a more easily erodible emission scheme, the *a priori* simulation (see in Fig. 6.10(a)) generated a dust band which originated from the Horqin desert and then carried towards northeast crossing the MR-A. The dust simulation in Fig. 6.10(b) are obtained by assimilating the Himawari-8 AODs in May 03. This *posterior* is validated to be in better agreement with the real states through the independent data (PM_{10} measurements) validation.

In SD2, parts of the dust concentrations in the MR-A are initialized with a dust plume in the left boundary, which is lifted from the Gobi and Mongolia desert. This initial plume is the result of a LOTOS-EUROS simulation driven by the prior emission scheme. meanwhile, extra particles are also mobilized from Horqin deserts and transported northwards. The new emission model increases the dust load, however, the simulation without assimilation still under estimates the PM_{10} concentrations shown in Fig. 6.4(a.1)~(a.3). Using the posterior emission field, the dust simulations are enhanced further, and are in much better agreement with the observations.

To quantify the improvements through the assimilation, the root mean square error (RMSE) between the observed PM_{10} concentrations and the *a priori* and posterior dust simulations has been computed for each hour during these two dust outbreaks, SD1 and SD2. These RMSE numbers are added to Fig. 6.6(b), which already showed similar time series for simulations using the original emission model studies. Using the 'new' emission model, the *a priori* RMSE values are slightly improved compared to the older simulations. Although extra emissions from the Horqin dessert are now included, the default amount is still not strong enough to simulate the observed dust peak, especially on the SD2. The largest improvement is made when assimilation is used to further enhance the emissions; the maximum RMSE values in the SD1 are reduced from 1,100 to 600 $\mu g/m^3$; in the SD2 they are reduced from 2,000 to 1,000 $\mu g/m^3$. In the original assimilation con-

figuration this could not be achieved since the emission uncertainty model did not allow any additional emissions from the Horqin desert at all.

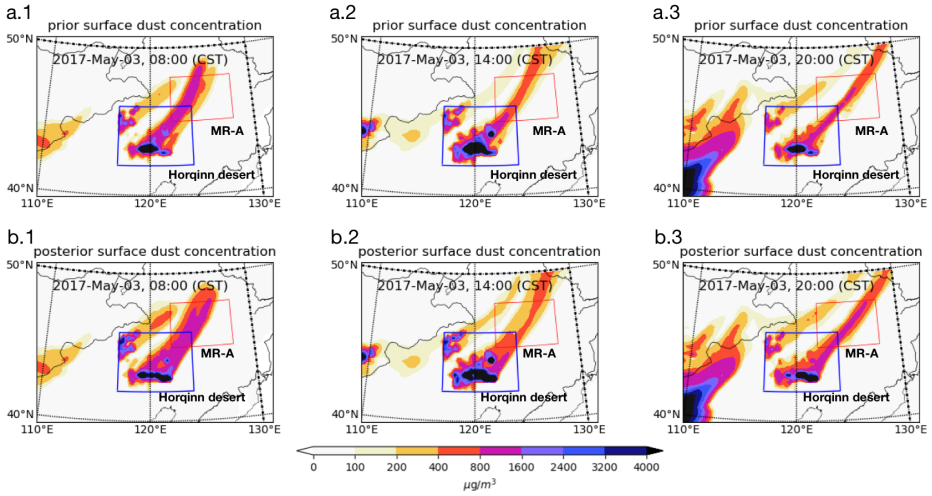

Figure 6.10: Simulation of SD1 using the new emission fields: (a) *a priori* and (b) *posterior* (by assimilating the Himawari-8 AODs) at May 03 08:00 (a.1)~(b.1); 14:00 (a.2~b.2); 20:00 (a.3 ~b.3).

6.6. CONCLUSIONS

In this Chapter, we illustrated the importance of background error covariance in emission inversion, and introduced an adjoint based method to identify the error sources for improving emission reconstruction. The methodology is applied to several dust outbreaks over East Asia in May 2017.

First, the dust storm emission inversion was reviewed. Although remarkale improvements on dust simulations and forecasts have been achieved through assimilating the Himawari-8 satellite AODs, very large errors still remained unresolved in local regions. Specifically, three severe dust outbreaks in the northeast China were investigated, which are neither reproduced by the *a priori* nor by the *posterior* simulation despite the assimilated measurements did indicate the existence of severe dust plumes.

To trace the potential emission sources back regarding the several dust outbreaks, a adjoint model was introduced, which is relatively efficient in calculating the sensitivities of model responses with respect to a large number of input parameters. Before the implementation on emission backtracking in practice, the adjoint model is first evaluated. The results show that the adjoint sensitivities are in a good agreement with the values obtained using a finite difference method.

The adjoint was then used to trace the sensitive emission sources to the three independent dust outbreaks, respectively. All the experiments indicated that the Horqin desert is the most likely dust sources, which used to be considered of less importance in East Asia dust storm forecasts.

The emission scheme and the corresponding uncertainties over the Horqin desert

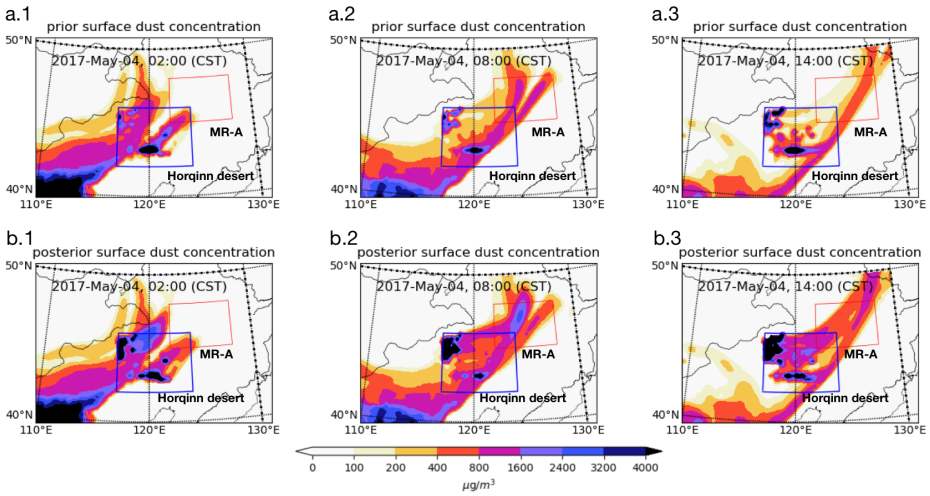

Figure 6.11: Simulation of SD2 using the new emission fields: (a) prior and (b) posterior (by assimilating the ground-based PM_{10} observations) at May 04 02:00 (a.1)~(b.1); 08:00 (a.2~b.2); 14:00 (a.3 ~b.3).

6

are then reconstructed by assigning higher erodibility. The 'new' *a priori* RMSE values are slightly improved compared to the 'old' simulations through including extra emissions over Horqin desert. Significant improvements are made when a new assimilation is carried out to further enhance the emissions. The maximum RMSE values are reduced from 2,000 to 1.100 $\mu g/m^3$.

Our study clearly shows the importance of an corrected background error covariance in resolving observation-minus-simulation errors in emission inversions. The proposed adjoint method could also be performed to identify the sensitive emission sources and guide the construction of emission uncertainties in other atmospheric inverse modeling applications, e.g., black carbon, haze or gases.

6.7. SUPPLEMENTARY

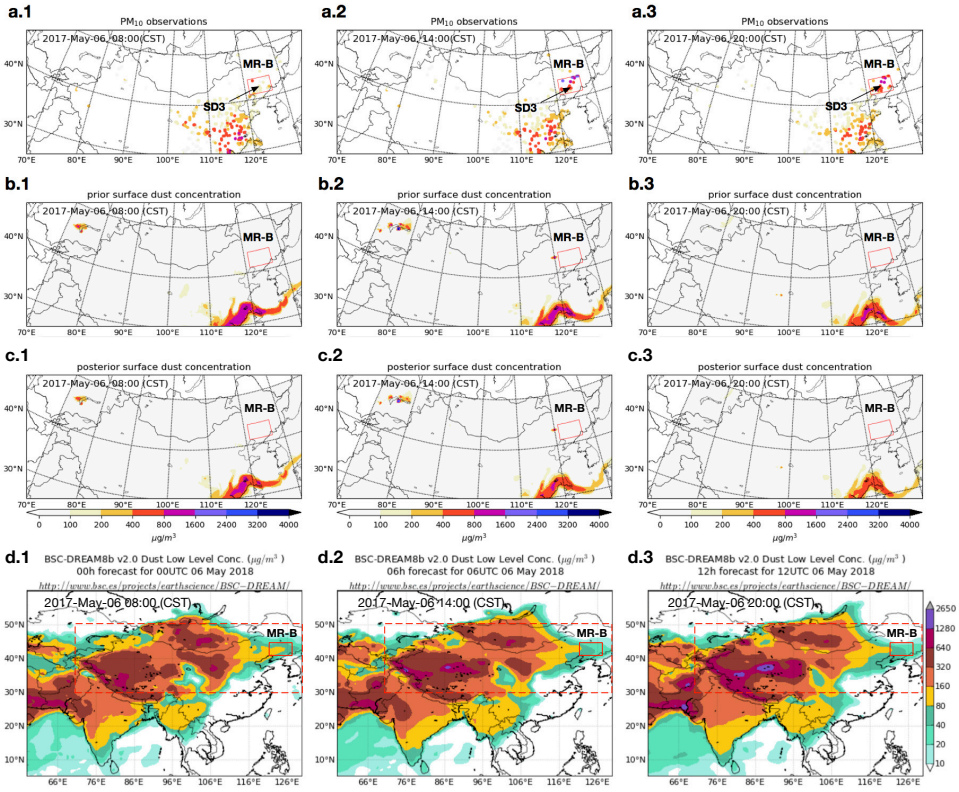

Figure 6.12: PM_{10} observations (a.1~a.3) vs. surface dust concentration simulation of the 3rd severe dust (SD3) from LOTOS-EUROS prior (b.1~b.3), posterior (c.1~c.3) and BSC-DREAM8b (d.1~d.3) over the marked region 2 (MR2) at May 06 08:00 (CST): a.1~d.1; 14:00 (CST): a.2~d.2; 20:00 (CST): a.3~d.3.

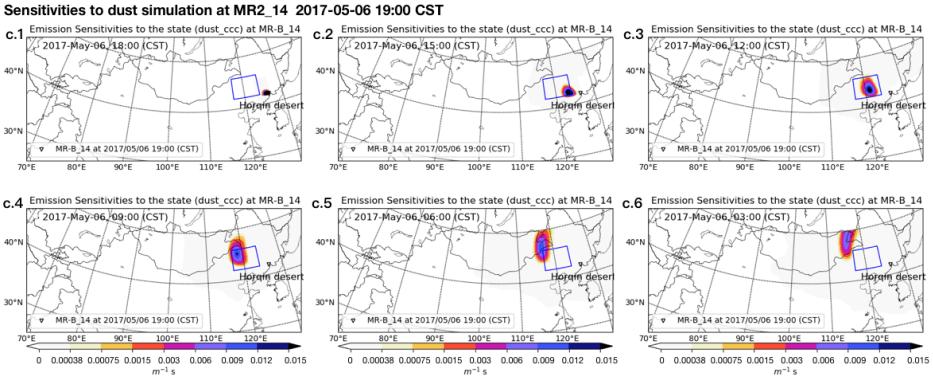

Figure 6.13: Backward time series of emission sensitivity of the dust simulation at MR-B_14 2017 May 06, 19:00 CST.

REFERENCES

An, X. Q., Zhai, S. X., Jin, M., Gong, S., and Wang, Y. (2016). Development of an adjoint model of GRAPES–CUACE and its application in tracking influential haze source areas in north China. *Geoscientific Model Development*, 9(6):2153–2165.

Dee, D. P. and Uppala, S. (2009). Variational bias correction of satellite radiance data in the ERA-Interim reanalysis. *Quarterly Journal of the Royal Meteorological Society*, 135(644):1830–1841.

Di Tomaso, E., Nick, Jorba, O., and Garcia-Pando, C. P. (2017). Assimilation of MODIS Dark Target and Deep Blue observations in the dust aerosol component of NMMB-MONARCH version 1.0. *Geoscientific Model Development*, 10:1107–1129.

DIMET, F.-X. L. and TALAGRAND, O. (1986). Variational algorithms for analysis and assimilation of meteorological observations: theoretical aspects. *Tellus A*, 38A(2):97–110.

Elbern, H., Schmidt, H., and Ebel, A. (1997). Variational data assimilation for tropospheric chemistry modeling. *Journal of Geophysical Research: Atmospheres*, 102(D13):15967–15985.

Elbern, H., Schmidt, H., Talagrand, O., and Ebel, A. (2000). 4D-variational data assimilation with an adjoint air quality model for emission analysis. *Environmental Modelling & Software*, 15(6):539–548.

Guerrette, J. J. and Henze, D. K. (2015). Development and application of the wrfplus-chem online chemistry adjoint and wrfda-chem assimilation system. *Geoscientific Model Development*, 8(6):1857–1876.

Hakami, A., Henze, D. K., Seinfeld, J. H., Chai, T., Tang, Y., Carmichael, G. R., and Sandu, A. (2005). Adjoint inverse modeling of black carbon during the Asian Pacific Regional Aerosol Characterization Experiment. *J. Geophys. Res.*, 110(D14):D14301+.

Henze, D. K., Hakami, A., and Seinfeld, J. H. (2007a). Development of the adjoint of GEOS-Chem. *Atmospheric Chemistry and Physics*, 7(9):2413–2433.

Henze, D. K., Hakami, A., and Seinfeld, J. H. (2007b). Development of the adjoint of geos-chem. *Atmospheric Chemistry and Physics*, 7(9):2413–2433.

Henze, D. K., Seinfeld, J. H., and Shindell, D. T. (2009). Inverse modeling and mapping US air quality influences of inorganic PM2.5 precursor emissions using the adjoint of GEOS-Chem. *Atmospheric Chemistry and Physics*, 9(16):5877–5903.

Hourdin, F. and Talagrand, O. (2006). Eulerian backtracking of atmospheric tracers. I: Adjoint derivation and parametrization of subgrid-scale transport. *Quarterly Journal of the Royal Meteorological Society*, 132(615):567–583.

Khade, V. M., Hansen, J. A., Reid, J. S., and Westphal, D. L. (2013). Ensemble filter based estimation of spatially distributed parameters in a mesoscale dust model: experiments with simulated and real data. *Atmospheric Chemistry and Physics*, 13(6):3481–3500.

Minamoto, Y., Nakamura, K., Wang, M., Kawai, K., Ohara, K., Noda, J., Davaanyam, E., Sugimoto, N., and Kai, K. (2018). Large-Scale Dust Event in East Asia in May 2017: Dust Emission and Transport from Multiple Source Regions. *SOLA*, 14:33–38.

Talagrand, O. and Courtier, P. (1987). Variational Assimilation of Meteorological Observations With the Adjoint Vorticity Equation. I: Theory. *Quarterly Journal of the Royal Meteorological Society*, 113(478):1311–1328.

Yoshida, M., Kikuchi, M., Nagao, T. M., Murakami, H., Nomaki, T., and Higurashi, A. (2018). Common Retrieval of Aerosol Properties for Imaging Satellite Sensors. *Journal of the Meteorological Society of Japan. Ser. II*, advpub.

Yumimoto, K., Murakami, H., Tanaka, T. Y., Sekiyama, T. T., Ogi, A., and Maki, T. (2016). Forecasting of Asian dust storm that occurred on May 10–13, 2011, using an ensemble-based data assimilation system. *Particuology*, 28:121–130.

Yumimoto, K. and Takemura, T. (2015). Long-term inverse modeling of Asian dust: Interannual variations of its emission, transport, deposition, and radiative forcing. *J. Geophys. Res. Atmos.*, 120(4):2014JD022390+.

Yumimoto, K., Uno, I., Sugimoto, N., Shimizu, A., Liu, Z., and Winker, D. M. (2008). Adjoint inversion modeling of Asian dust emission using lidar observations. *Atmospheric Chemistry and Physics*, 8(11):2869–2884.

Zhai, S., An, X., Zhao, T., Sun, Z., Wang, W., Hou, Q., Guo, Z., and Wang, C. (2018). Detection of critical pm$_2.5$ emission sources and their contributions to a heavy haze episode in beijing, china, using an adjoint model. *Atmospheric Chemistry and Physics*, 18(9):6241–6258.

Zhang, X. X., Sharratt, B., Liu, L. Y., Wang, Z. F., Pan, X. L., Lei, J. Q., Wu, S. X., Huang, S. Y., Guo, Y. H., Li, J., Tang, X., Yang, T., Tian, Y., Chen, X. S., Hao, J. Q., Zheng, H. T., Yang, Y. Y., and Lyu, Y. L. (2018). East Asian dust storm in May 2017: observations, modelling, and its influence on the Asia-Pacific region. *Atmospheric Chemistry and Physics*, 18(11):8353–8371.

7

CONCLUSIONS

7.1. DISCUSSION OF THE RESEARCH QUESTIONS

Severe dust storms present great threats to the environment, property and human health over the areas in the downwind of arid regions. Though dynamical dust models have been developed to predict the dust concentrations, the accuracy of these models is usually limited. Along with the progress in the dust modeling, the advances in sensor technologies have made large-scale aerosol measurements feasible. The rich measurements provide opportunities to optimize these dust storm forecast systems through data assimilation. Remarkable progress has also been made in the dust storm data assimilation, however, the dust assimilation study still has large spaces for further improvements.

In this thesis, we further optimized the fast-varying dust storms by exploring four research questions (**Rq**) that were proposed in Chapter 1. The conclusions of this thesis corresponding to these research questions are listed below.

Rq.1 How to quantify the uncertainty in state-of-the-art dust emission parametrization? In data assimilation context that means: how to configure the background error covariance?

In **Chapter 2**, the representation errors of the existing emission parametrization in large-scale models are analyzed. They are identified to be mainly caused by the uncertainties in wind fields related to calculated friction velocities, and soil and surface properties quantified using friction velocity threshold. The relative importance of these two key factors contributing to the emission uncertainty are evaluated. It shows that the variability in emissions due to uncertainty in friction velocity is relatively small compared to the variability due to uncertainty in friction velocity threshold. The total standard deviation is therefore mainly caused by the uncertain soil/surface parameters in our test case. This background uncertainty configuration together with the assimilation algorithm are capable of resolving most observation-minus-simulation errors, as well as to improve the dust forecast skills.

In **Chapter 6**, (occasionally), the empirical background uncertainty might be partially unrepresentative, since the uncertainties induced from a lot of different inputs cannot be simultaneously taken into account. To resolve remaining errors in local regions after assimilation analysis, an adjoint model based sensitivity method was introduced. The adjoint method is capable of tracing the potential emission sources. The adjoint model is very efficient in calculating the sensitivities of model responses with respect to a large number of input parameters. It is validated to be in a good agreement with the values obtained using a finite difference method. Our adjoint model indicated Horqin desert is the main dust sources for dust events in northeast China, which used to be considered of less importance in East Asia dust storm forecasts. The new emission inversion with reconstructed background uncertainty guided by the adjoint model results in further improvements on the dust simulation/forecast.

Our study clearly demonstrates the importance of a corrected emission error covariance in resolving observation-minus-simulation errors. The proposed adjoint method can also be applied to identify the most important emission sources for observations in other applications, e.g., black carbon, haze or gases.

Rq.2 How to develop a data assimilation algorithm for the dust emission inversion with a high computational efficiency?

In **Chapter 3**, an integrated dust storm emission inversion system, which includes a regional dust transport model LOTOS-EUROS/dust and a reduced-tangent-linearization 4DVar, has been developed. The system aims to correct the mismatch in the emission parameterization and hence improve the dust forecast skill. An attractive advantage of the assimilation algorithm is that the adjoint model is not required, and replaced with the rank reduced tangent linear (TL) model. The TL is approximated by the perturbation method, the cost of which is proportional to the parameter dimension. Two model reduction techniques are designed to achieve a high computational efficiency. The first one includes the three spatially varying multiplicative factor (SVMF) filters which reduces the parameter dimension size from $O(10^4)$ to $O(10^3)$, the second one applies the Proper Orthogonal Decomposition (POD) to further project the subspace into a set of key patterns $O(10^2)$.

Rq.3 When assimilating PM_{10} observations with dust simulations, to what extent is the non-dust bias in these observations misleading the analysis, and how to use the full aerosol measurements as a proxy for dust in the emission inversion?

Chapter 4: The presence of inconsistent measurements with nontrivial biases or inseparable baselines is unavoidable in practice. Assimilation analysis might diverge from reality, since the data assimilation itself cannot distinguish whether the observation-minus-simulation errors are due to the biased observations or model deficiencies. The impacts of observation biases on assimilation analysis are explored through a real application, which is the dust emission inversion conditioned on PM_{10} observations.

Two methods have been implemented to remove the *non-dust* part the PM_{10} observations during the dust event in order to use them as 'dust' proxy in a dust assimilation system. The first method uses the full chemistry version of the LOTOS-EUROS, which

simulates the emission, transport, chemistry, and deposition of aerosols mainly related to anthropogenic activities. The second method uses a machine learning model that statistically describes the relations between regular PM_{10} concentrations (outside dust events), and available air quality and meteorological data.

Dust emission inversion tests are conducted that either assimilated the original PM_{10} observations, or bias-corrected 'dust' observations based on either LOTOS-EUROS/*non-dust* or LSTM model. The posterior simulations using the original observations resulted in a strong overestimation of the dust concentrations, since all PM_{10} are simply attributed to dust. Using the LOTOS-EUROS/full-chemistry bias-corrected observations, a clear improvement on the dust simulation has been obtained, but overestimation of dust concentrations is still present. The best results are obtained when using a LSTM model to remove the *non-dust* part of the PM_{10} observations, with *posterior* concentrations in good agreement with the measurements.

The dust emissions estimated using the assimilation can be used to drive a dust forecast. When the original PM_{10} observations were used in the assimilation, the forecast skill of the system actually decreased due to the strong overestimation of dust concentrations; the RMSE for example increased from averagely 230 (prior forecast) to 300 $\mu g/m^3$. Better forecasts are obtained when using the model-based and especially the machine learning based bias-corrected observations. The RMSE of the former one was reduced to 200 $\mu g/m^3$ while the RMSE of the latter one further declined to 150 $\mu g/m^3$.

Rq.4 What is the added value of assimilating aerosol properties from a geostationary satellite, and how to exclude inconsistent AOD observations which might arise from retrieval errors over a partially clouded scene?

In **Chapter 5**, total column AOD observations from the geostationary satellite Himawari-8 have been used in our dust emission inversion system. The AOD product of this instrument has a wide spatial coverage and a high spatial and temporal resolution, which provides valuable information to monitor dust storms over Asia.

An extreme dust storm event over North China during May 3-5 2017 was selected as test case for the assimilation. The Himawari-8 AOD observations were found to be consistent with the available AOD observations from the AERONET network. Simulations of dust have been made using the LOTOS-EUROS regional air quality model, and time series of simulated AOD showed in general good agreements with the observations with respect to arrival and departure of the dust storm, but the amplitude is over estimated.

However, in one region the satellite retrievals of AOD showed rather high values that are not represented by the simulation model. These high AOD values could not be confirmed by AERONET observations, and might be attributed to presence of partially clouded scenes. Using these Himawari observations in an assimilation would lead to inaccurate analyzed dust emissions, and that would lead to incorrect forecast simulations. Therefore, observation selection criteria have been developed by selecting only those observations that can be represented by the model. A *dust mask* selection that uses only those observations, where the model also simulates an amount of dust, was shown to provide the best results.

The assimilation system estimated the dust emissions over daily time windows during the dust event. Assimilation of Himawari AOD is shown to provide emission esti-

mates that, when used as input for the model, strongly improves the simulated AOD as well as the simulated surface concentrations compared to the PM_{10} observations. Using proper selection of AOD observations in the assimilation, the forecast skill during the dust storm was strongly improved.

7.2. OUTLOOK

The research questions of this thesis and insights gained from the results open doors to new future research questions (**FRq**).

FRq.1 In large-scale model systems, the representation of dust emission parametrization remains relatively crude, which is mainly caused by uncertainties in tremendous amount of input sources such as wind fields, soil properties (moisture, soil texture, clay fraction), surface roughness, landcover (vegetation), topography, as well as insufficient knowledge about the aerosol lifting process itself. In this study, only the errors in the friction velocity threshold and wind field are considered. The uncertainties caused by the mismatch or imperfections in the other factors might also play a role in real variabilities of the dust simulations, especially with respect to the fine-scale.

In addition, the dominant error source in emission uncertainty is identified to be the friction velocity threshold parameterization. It is compensated by a spatially varying multiplicative factor (SVMF) in this thesis work. The SVMF is currently assumed to be temporally constant in each assimilation cycle (24 or 36 hours), but able to vary among different windows. The temporal parameter variation patterns within the assimilation window deserve to be further explored, especially under the circumstance of a large amount of data.

FRq.2 In order to use the PM_{10} measurements as a proxy for dust in our emission inversion, two methods for estimating the *non-dust* part of the PM_{10} load have been implemented, based on either a CTM or a machine learning method. The CTM simulates life cycles of those *non-dust* aerosols. The machine learning model describes the relations between the regular PM_{10} and other air quality measurements, which is trained using time series of historical samples.

Both the CTM and machine learning based bias correction methods have room for further improvements. It might be useful to improve the CTM simulations by assimilating PM_{10} observations during the hours where no dust storms are present, and use these improved simulations to remove the *non-dust* part of the observations during the coming dust event. These additional assimilations would then involve repeated forward ensemble bias-model runs which could be computationally expensive. The machine learning model in our full chemistry PM_{10} simulation can also be further optimized, such as using a deeper neural network, including extra input features like *non-dust* PM_{10} simulation from CTMs and other related records.

FRq.3 Theoretically, the observational uncertainties are due to the representation errors as well as the measurement errors, e.g., incorrect sensor readings, bugs in the data

processing pipeline, and inaccurate bias correction. At present, only the former one is take into account in this thesis. The existence of representation errors in our system is mainly because the dust model uses a spatial resolution of 25 km to limit computation time, while the in-situ measurements are representative for a smaller area. The spatial representation error could be quantified through comparing the model simulations at different scales of resolutions.

The error due to the different bias correction terms is another source of uncertainties. Regarding the machine learning based bias correction method, the error itself is actually available and can be easily extracted from the training results.

ACKNOWLEDGEMENTS

Looking back, I realize undertaking this PhD has been one of the most life-changing decisions I have ever made. The process not only broadened my horizons in science, but let my teenager's dream, to be a doctor, come true. It would not be possible to do without the helps that I received from many people.

First of all, I would like to express my sincere appreciation to my promoter Prof. Lin. I feel so lucky to work directly with him, not only for the consistence guidance and immense knowledge that helped my whole PhD research. I was also indebted to him for the supports and trusts when I made the enormous change of my PhD subject to atmospheric data assimilation in the 7th month of my PhD, as well as for those strong recommendations in my job hunting. Many thanks to my promoter Prof. Heemink for his patience, motivation, and insight feedbacks that helped me throughout my research and write this thesis. He was always encouraging me to meetings and conferences to give presentation and meet people.

Besides my promoters, my deepest gratitude goes to my supervisor Dr. Arjo Segers. Apart from being an exceptional scientist and an outstanding programmer, he has his own brand of humor and most time I can get it. Thanks so much for introducing me to the world of atmospheric modeling, for solving many technical issues regarding my dust model, and for the countless inspired discussions. He is the reason that I could complete this thesis on time. I also appreciate Arjo and Susan gratefully for trusting me and let me use their house for two months.

Furthermore, I would like to thank my colleagues in the TUDelft. I would like to thank Kees Lemmens for solving my linux issues, Evelyn Sharabi and Dorothee Engering for helping me out of several matters and Dutch documents translating, Guangliang for those stimulating discussions both at the start of my research and in life, Martin for answering those data-assimilation queries. It is a great pleasure to share with my working space with these amazing people including Yoeri, Sha, Kaihua, Corine, Xiaoyan, Tugce, Ada and Xiangrong.

I am grateful to my friends for making my stay in Delft so enjoyable, Haochuan for the gear and history related discussions, Xiaohui for her remarkable cooking and share, Cong and Senlei for direct humors, also to my gym partners Kuaiyu and Yancong, and my basketball teammates.

My research journey continued in TNO, the Department of Climate, Air and Sustainability. This would not have been possible without the support and guidance from Arjo

Segers and Bas Henzing.

I would like to express my special appreciation to mentor Wanbin, and my friends Ben and Hong for listening to my complaints and motivating me in my PhD.

Last, I would like to thank my family: my parents, my uncle and my sister for their financial supports, spiritual encouragements, unconditional love throughout writing this thesis and my life.

Jianbing
Utrecht, Oct 2019

CURRICULUM VITÆ

Jianbing JIN

Jianbing Jin was born in ShaoXing, China in February 1990. He obtained his BSc. and MSc. degree in Harbin Institute of Technology (in Harbin, China) in July 2013 and July 2015, respectively.

Supported by China Scholarship Council, Jianbing started his Ph.D. programme in Delft Institute of Applied Mathematics (DIAM), Delft University of Technology (TUD), the Netherlands in September 2015. The Ph.D. research was under the supervision of Prof. Hai Xiang Lin, Dr. Arjo Segers and Prof. Arnold Heemink. His research focuses are theory and applications of data assimilation, atmospheric modeling, machine learning in modeling dynamic systems and high performance computing.

During his Ph.D., Jianbing participated a number of conferences, such as EGU 2017, ICCART 2019 and AAC 2019, and two summer schools in atmospheric modeling and data assimilation. He worked as a teaching assistant for HPC courses and designed lab assignments, also supervised two master thesis programmes on machine learning for atmospheric modeling.

From September 2019, Jianbing is an assistant researcher at the Departments of Climate, Air and Sustainability, TNO, the Netherlands.

LIST OF PUBLICATIONS

IN THIS THESIS

1. **Jianbing Jin**, Hai Xiang Lin, Arnold Heemink, Arjo Segers.: *Spatially varying parameter estimation for dust emission using reduced-tangent-linearization 4DVar*, Atmospheric Environment, **187**, 358-373 (2018).

2. **Jianbing Jin**, Hai Xiang Lin, Arjo Segers, Yu Xie, Arnold Heemink.: *Machine learning for observation bias correction with application to dust storm data assimilation*, Atmospheric Chemistry and Physics, **19**, 10009-10026, (2019).

3. **Jianbing Jin**, Arjo Segers, Arnold Heemink, Mayumi Yoshida, Wei Han, Hai Xiang Lin.: *Dust emission inversion using Himawari-8 AODs over East Asia: an extreme dust event in May 2017*, Journal of Advances in Modeling Earth Systems, **11**, 446-467 (2019).

4. **Jianbing Jin**, Arjo Segers, Arnold Heemink, Hong Liao, Richard Kranenburg, Hai Xiang Lin.: *Backtracing dust emission errors using the adjoint method*, Atmospheric Chemistry and Physics (submitted).

SIDE WORK

1. **Jianbing Jin**, Arjo Segers, Hai Xiang Lin, Arnold Heemink, Xiaohui Wang: *Position feature correction in dust storm forecast: grid distortion data assimilation*, Geophysical Review Letters (to be submitted).

2. Hai Xiang Lin, **Jianbing Jin**, Jaap van den Herik: *Air quality forecast through integrated data assimilation and machine learning*, 11th Conference on Agents and Artificial Intelligence, Prague, 2019.